Master's Thesis GEO 511

Statistical analyses of spatial and temporal variability of ground surface temperatures in Alpine terrain

June 30, 2016

Submitted by:
Tobias Riebler
Matriculation No.: 10-709-020

Supervised by:
Dr. Jeannette Nötzli, SLF/PERMOS
Dr. Stefanie Gubler, MeteoSwiss
Dr. Benno Staub, unifr/PERMOS

Faculty Representative:
Prof. Dr. Andreas Vieli

Physical Geography 3G
Glaciology, Geomorphodynamics & Geochronology

Department of Geography University of Zurich
Winterthurerstrasse 190, CH-8057 Zurich

Abstract

Against the background of ongoing climate change, permafrost degradation is observed worldwide. As the interlinking element between the atmospheric conditions and the subsurface thermal regime, ground surface temperature (GST) is the main driving factor influencing the distribution and condition of permafrost. Thus, knowledge about the spatial and temporal variability of GST is crucial regarding the evaluation of the present and future state of permafrost.
This thesis analyzes the unique data set of GST time series collected by PERMOS, extended with data from various other permafrost research programs in the Swiss, French and Italian Alps. Thereby, the spatial and temporal variability of GST is studied by means of different statistical methods. To assess the spatial variability of GST in Alpine terrain, 1439 values of mean annual ground surface temperature from 260 measurement locations at 24 sites are analyzed by use of a multiple linear regression model. The temporal variability of GST is studied by means of a simple linear regression model with time as the explanatory variable. Through that, trends are computed for 36 GST and air temperature time series with lengths of 15 hydrological years. Furthermore, correlations are computed for 81 GST time series with lengths of 4 subsequent hydrological years.
Results reveal the dependence of mean annual ground surface temperatures on air temperature, topography, type of surface material, snow cover and meteorological conditions. In bedrock, mean annual ground surface temperature is 1.8°C higher than in coarse blocks, 1.2°C higher than in debris and 1.0°C higher than in soil. Differences between opposite aspects strongly increase with increasing slope angle and mean annual ground surface temperature decreases with a lapse rate of -4.5°C km^{-1} within Alpine terrain. The temporal variability of GST is pronounced. Regarding a time period of 15 hydrological years (2000 – 2014), the mean inter-annual variability of mean annual ground surface temperature (± 0.47°C) is very much like the mean inter-annual variability of mean annual air temperature (± 0.43°C). In the same time interval, annual trends for both GST and air temperature are not significant. Thereby, the effect of variable snow conditions on mean annual ground surface temperature exceeds the effect of mean annual air temperature on mean annual ground surface temperature in short term observations. With a correlation coefficient of -0.35, the variability between GST time series increases with increasing distance.
The analyzed data set proved to be feasible for statistical analyses regarding the spatial and temporal variability of GST. However, the distribution of slope, type of surface material, aspect and elevation is not balanced. Moreover, the distribution of measurement locations within Alpine terrain is done in piecemeal fashion. Therefore, the informative value regarding the under represented categories is limited. In terms of future analyses, extensions and set-up changes of the existing monitoring set-up should be used to fill these gaps where possible.

Contents

List of Figures

List of Tables

1 Introduction

1.1 Motivation

During the last century, global mean annual air temperature has risen by about 0.7°C (Trenberth et al., 2007). Because permafrost is a subsurface phenomenon defined by the thermal condition of the ground, it reacts sensitively to changes in climatic conditions. As a result of this linkage, permafrost warming is being observed in Europe, Alaska, Canadian high Arctic, Russia and Svalbard (Blunden & Arndt, 2015; Farbrot et al., 2013; C. Harris et al., 2003; Hipp et al., 2012; Isaksen et al., 2007; Romanovsky et al., 2010).

The understanding of the spatial and temporal variability of ground surface temperature (GST) is important in many respects. As the interlinking element between the atmospheric conditions and the subsurface thermal regime, GST is the main driving factor influencing the distribution and condition of permafrost. Thus, knowledge about the spatial and temporal variability of GST is crucial regarding the evaluation of the present and future state of permafrost. Mean annual air temperature trends for 45 MeteoSwiss stations between 1961 – 2005 proved to be strongly positive and statistically significant on the 5% level for all stations (Appenzeller et al., 2007). No obvious dependence of the trends with altitude or geographical position is observed. At the same time, studies regarding different ground temperature (GT) time series measured in boreholes in permafrost areas in Switzerland also have shown significant warming trends (Zenklusen Mutter et al., 2010; PERMOS, 2013). Nevertheless, the variability of GST is still not fully understood. This is because the processes connecting the atmosphere with the ground thermal regime are highly variable on the small scale due to highly fluctuating environmental conditions in mountainous terrain.

Moreover, the analysis of GST is relevant regarding the representativeness of GT measured in boreholes. Because the installation of boreholes is cost-intensive and involved logistics are challenging in most cases, the amount of boreholes is limited within a particular region. As a consequence, GT measurements represent point information with a low spatial density. Simultaneously, GT time series from boreholes are the main indicators for the past and present state of permafrost, often describing the thermal state of the ground over large areas. In this context, GST measurements are relevant in order to study the representativeness of GT regarding the thermal regime of its nearby environment.

The understanding of GST variability is additionally important in the context of permafrost modeling. Permafrost is a subsurface phenomenon, whose occurrence is invisible apart from a few exceptions. Typically, temperature measurements in permafrost areas are sparsely

available and represent point information. Furthermore, site access is limited in most cases. This is why modeling approaches are necessary to estimate the spatial distribution of permafrost (Gruber & Hoelzle, 2001; C. Harris et al., 2009). In this context, GST is often used to validate the performance of statistically and physically based models. However, due to the high spatial and temporal variability of GST, permafrost mapping approaches including point data must be interpreted carefully (Gruber, 2012). Hence, it is of great importance to know about the possible band width of GST variations in space and time in order to correctly interpret results.

In the context of Alpine permafrost terrain, variability of GST has so far been analyzed on a local to regional scale. Gubler et al. (2011) measured differences in mean annual ground surface temperatures (MAGST) of up to 6°C within an elevation band of 300 m. Pogliotti et al. (2015) observed that the spatial variability (2.5 ± 0.1°C) within a restricted area of about 0.01 km^2 can far exceed the inter-annual variability (1.6 ± 0.1°C) of the corresponding loggers. In steep bedrock, mean daily temperature gradients can be up to 10°C over only 6 m distance (Haberkorn et al., 2015). Additionally, Hasler et al. (2011) found that MAGST can range between 1 – 8°C in bedrock with slope angles > 45°. These differences are mainly the consequence of ground properties, heterogeneity of snow cover thickness in space and time, variation in slope and aspect. The assessment of the spatial variability of GST on a continental scale like the Alpine terrain is still missing. Furthermore, few analyses exist on the long-term variability of GST in space and time and little is documented about the long-term effects of changes in mean annual air temperature on the thermal regime in mountain permafrost (Haeberli et al., 2010).

1.2 Research questions

This thesis analyzes the extensive and unique data set of GST time series collected by the universities and research institutes in the frame of the Swiss Permafrost Monitoring Network PERMOS, extended with data from various other permafrost research programs in the Swiss, French and Italian Alps. Thereby, the spatial and temporal variability of GST is studied by means of statistical methods. In total, time series from 275 GST measurement locations with lengths of up to 15 hydrological years are analyzed. The main goal is to contribute insights relating to the spatial and temporal variability of GST in Alpine terrain from an observation-based perspective. Moreover, the measurement set-up and the available data set are evaluated regarding their spatial distribution. Accordingly, this thesis addresses the following research questions:

- How is the spatial variability of GST influenced by topographic parameters, type of ground surface material, snow cover and different regions in Alpine terrain?
- What is the temporal variability of GST within the Swiss Alps?
- How could the measurement set-up of GST monitoring in Alpine terrain be improved in terms of future analyses?

2 Scientific background

2.1 Definition of permafrost

Permafrost (perennially frozen ground) is defined as lithosphere material that remains at or below 0°C for at least two consecutive years (French, 2007). Because of its thermal definition, permafrost is found at high-latitude lowlands as well as mid-latitude high mountain regions, both leading to a cold thermal regime in the ground. In Switzerland about 5% of the total area is underlaid by mountain permafrost (Boeckli et al., 2012), whereby *mountain permafrost* is simply permafrost in mountain areas, typically characterized by great relief variations (Gruber & Haeberli, 2009). Since the majority of this area has temperatures just below 0°C (Haeberli & Guodong, 1993), the sensitivity of mountain permafrost to changes in climate is high. However, temperatures in permafrost areas can be as low as -25°C at high altitudes (Figure 7.1).

2.2 Influencing factors

Because permafrost is thermally defined, the distribution of permafrost is controlled by factors influencing the energy exchange processes between the atmosphere, the surface and the underground (Etzelmüller et al., 2001; Hoelzle, 1996). According to Gruber (2005) the distribution of mountain permafrost can be conceptualized with the domains *climate*, *topography* and *ground conditions* (Figure 2.1), which influence the occurrence of permafrost on different scales. Climate is the leading factor on the continental scale (e.g. the Alps), defining air temperature, solar and net radiation and precipitation patterns as a function of latitude, altitude and continentality (Barry, 2008).

On the regional scale (e.g. Piz Corvatsch), these conditions are overlaid by topography as the governing factor. Thereby, air temperature is controlled by elevation. Furthermore, solar irradiation is determined by slope angle and topographic aspect, defining the insolation angle as well as the shading through the terrain geometry (C. Harris et al., 2009; Šafanda, 1999). Moreover, the topographic parameters slope angle and curvature play an important role regarding the redistribution of snow by wind and avalanches (Haeberli et al., 2010; Luetschg et al., 2004). In complex high-mountain topography, three-dimensional effects additionally influence the distribution of permafrost through lateral heat fluxes (Noetzli et al., 2007; Noetzli & Gruber, 2009). Overall, the existence of mountain permafrost is strongly dependent on topography in high-relief regions such as the Swiss Alps (Etzelmüller & Frauenfelder, 2009).

The topographically overlaid climate conditions are modified by ground properties and snow variability at the local scale (e.g. late spring snow patch). The effect of snow on the ground thermal regime is subject to many different parameters of the snow cover itself such as timing, duration, thickness, density and structure, governing the energy exchange through its low thermal conductivity and high albedo (Zhang, 2005). The snow cover generally constrains the energy exchange at the ground surface and decouples the ground thermal regime from the atmospheric conditions, leading to higher mean annual ground temperatures due to protection from heat loss in winter (Goodrich, 1982). Because the thermal resistance is a function of snow thickness, the degree of decoupling is dependent on snow depth (Bernhard et al., 1998). Field observations as well as numerical simulations prove that in coarse blocky material, snow depth of more than 0.6 m is necessary for effectively insulating the ground (Hanson & Hoelzle, 2004; Luetschg et al., 2008).

On gentle slopes, a thin snow cover along with low atmospheric temperatures has a cooling effect on the ground thermal regime due to high surface albedo of fresh snow and little insulation from cold air (Schneider et al., 2012; Zhang, 2005). If present, thin snow covers in steep bedrock lowers the surface temperature as well. By that, the solar irradiation is reflected by the thin snow cover in summer, resulting in a cooling of the thermal regime at the ground surface (Hasler et al., 2011; Magnin et al., 2015). However, this cooling effect diminishes with extreme steepness because of reduced snow cover (Gruber & Haeberli, 2007). On gentle slopes, the effect of thick snow covers depend on the date of first winter snow insulation: An early snow onset date results in an insulated ground and thus prevents the ground thermal regime from cooling. Accordingly, a late snow onset date has a cooling effect on the ground thermal regime. This highlights the timing of the first significant snowfall in early winter as a critical factor regarding the thermal development of the ground. For this reason, GST is strongly affected by the duration of the non-insulating snow period in early winter (Luetschg et al., 2008). In spring, thick snow covers (e.g. accumulated avalanche snow) have a cooling effect on the underlying ground, because they act like a barrier for the warm atmospheric temperatures, consume melt energy and reflect the incoming solar radiation (Luetschg et al., 2004).

On the local scale, the ground thermal regime is additionally influenced by the ground surface material. Thereby, coarse blocky material has a cooling effect on the subsurface temperatures, which is shown in many studies. Despite the lack of definite proof, several hypotheses exist to explain the thermal anomaly in block-rich material compared with finer-grained material and bedrock. The first hypotheses refers to *interconnecting voids*, enabling advective heat transfer through air movement, which leads to cooler ground temperatures compared to adjacent soils consisting of fine grained material (S. A. Harris & Pedersen, 1998; Schneider et al., 2012). The heat exchange in open work block fields is thus dominated by atmospheric processes (Herz et al., 2003), which favors an efficient and lasting exchange of cold air during early winter and result in a negative thermal anomaly (Bernhard et al., 1998). This effect is increased by protruding blocks, dampening the insulating effect of the snow cover in winter (Gruber & Hoelzle, 2008). The second concept is the *balch effect*. Since cold air is denser

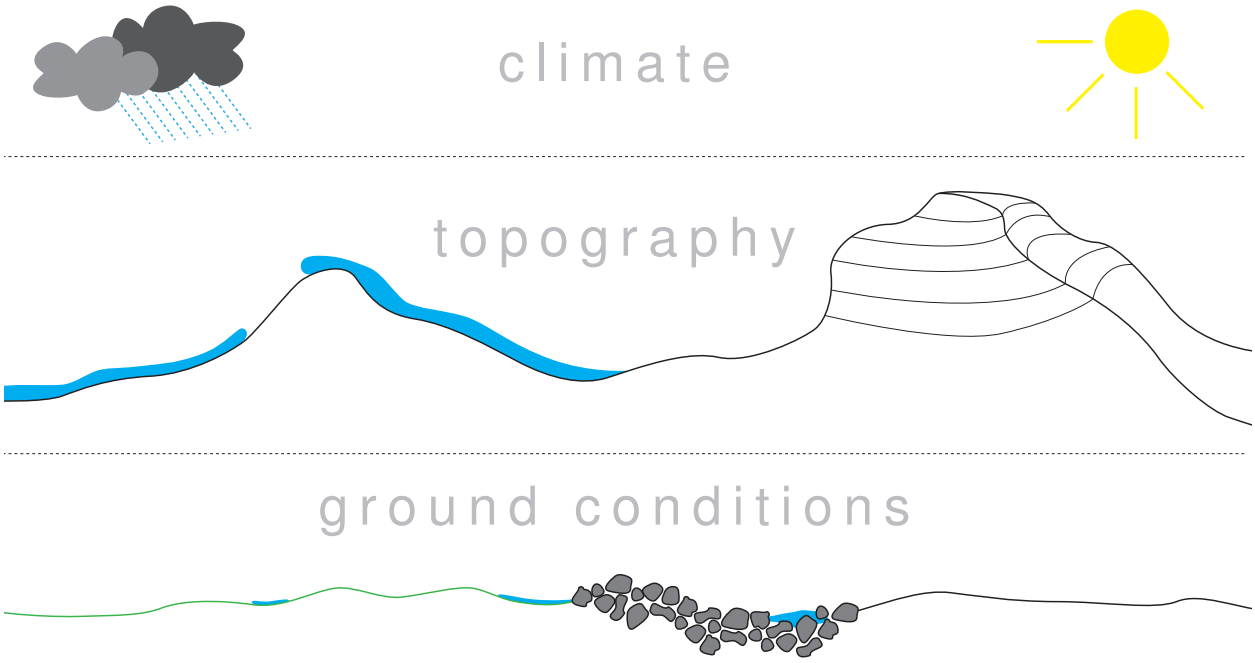

Figure 2.1: Domains influencing permafrost on different scales.

than warm air, cold air will tend to displace warmer air in the interstice volume between the blocky material cooling down the nearby environment (S. A. Harris & Pedersen, 1998). As a consequence, the air in the top part of the ground is characterized by a stable stratification. Thus, the advective heat exchange through air movement is inhibited, which is an important cooling process in summer. The third explanation refers to air circulation in talus slopes and is called the *chimney effect*. According to Delaloye and Lambiel (2005), differences in air density result in a upwards movement of warm air in winter, which causes the aspiration of cold air in the lower part of the slope through a thick but porous snow pack, leading to cold reservoir within the scree. This mechanism takes a reverse course during summer, preventing the ground thermal regime from rising significantly above 0°C (Delaloye et al., 2003; Morard et al., 2010).

Beside snow cover and coarse ground surface material, also vegetation canopy and surface organic layers have a critical effect on the ground thermal regime, although their significance in mountainous terrain play a minor role compared to high-latitude lowlands. In general, vegetation and organic material shield the ground thermal regime from solar heat, leading to lower GST than air temperature (AT) in summer (French, 2007). This cooling effect is enhanced in winter, when thermal conductivity is higher due to frozen soils, enabling the intrusion of low temperatures into the ground. These processes lead to lower temperatures at the permafrost table relating to GST. Because the processes on the local scale collude with the factors from the other domains, GST vary significantly over short distances, leading to a highly heterogeneous ground thermal regime in mountainous terrain.

2.3 Surface thermal regime

In terms of the main energy exchanging processes, the influencing factors of the different domains are proxies for the *surface energy balance*. The surface energy balance is the basis of the coupling between the atmospheric conditions and the thermal regime of the ground and is responsible for the ground surface temperature regime. The processes involved in the surface energy balance comprise the net exchange of radiation between the atmosphere and the earth surface, the transfer of sensible and latent heat by turbulent motion of the air and the conduction of heat into the ground (Williams & Smith, 1989). The surface radiation balance R_{net} [Wm^{-2}] is

$$R_{net} = S_{in} \times (1 - \alpha) + L_{in} - L_{out} \tag{2.1}$$

where R_{net} is the net radiation absorbed at the earth's surface, S_{in} is the shortwave incoming radiation, L_{in} the longwave incoming radiation and L_{out} the emitted longwave radiation (Ohmura & Raschke, 2005; van den Broeke et al., 2004). The albedo α determines the amount of reflected shortwave incoming radiation and is a site-specific property which can vary widely. S_{in} is mainly a climatic factor, because it is strongly influenced by latitude, time of year and weather conditions. S_{in} is also determined by local topography, especially in mountainous terrain, where changes in slope angle and topographic aspect are frequent. L_{in} depends largely on cloud conditions and atmospheric humidity. L_{out} is determined by ground surface temperatures and emissivity. Thus, L_{in} and L_{out} are considered as climatic factors as well. Including the other processes, the surface energy balance can be written as

$$R_{net} + Q_h + Q_{le} + Q_g + Q_m = 0 \tag{2.2}$$

where Q_h is the turbulent heat flux of the sensible heat, Q_{le} the turbulent heat flux of the latent heat, Q_g the heat conduction into the ground and Q_m the melt energy. Because energy cannot simply disappear, the individual fluxes of the surface energy balance in equation 2.2 must balance at all times (Williams & Smith, 1989). The turbulent heat fluxes Q_h and Q_{le} depend on surface roughness, wind speed, atmospheric stability and temperature differences between air and surface, whereas Q_{le} is additionally determined by the availability of water and radiation (Williams & Smith, 1989). Providing that snow or ice is available at the ground surface, Q_m is present as long as enough energy is available for melting ($\mathrm{T} > 0°\mathrm{C}$ without melting). The amount of snowmelt is given by the positive sum of the energy balance fluxes, assumed that equation 2.2 is solved for Q_m (Mittaz et al., 2002). If so, the net energy flux is functioning as an energy source for melting. The influencing factors regarding Q_g are explained below. Throughout the winter, the surface energy balance is mainly dominated by the radiation balance, despite the high albedo of the snow cover (Plüss, 1997): The net radiation is negative or near zero in the premelting season, while it is mainly positive in the melt season. At the same time, the turbulent fluxes show small long term averages.

2.4 Subsurface thermal regime

Once the near-surface temperature regime is defined through the surface energy balance, the temperature signal is transferred into the ground. The main heat transfer mechanism is conduction (Smerdon et al., 2003), but due to air or water flows, heat can also be transferred through advective processes (Delaloye & Lambiel, 2005; Kane et al., 2001; Romanovsky & Osterkamp, 2000). The conductive heat flux Q_g is given by:

$$Q_g = -K(dT/dz) \tag{2.3}$$

where dT/dz is the thermal gradient and K the thermal conductivity [W $m^{-1}K^{-1}$], i.e. the rate of heat transfer in the ground. The thermal conductivity of the ground is strongly dependent on lithology, content of air, water and ice, because the range in thermal properties between these ground constituting components is high (Table 7.1). This is why the spatio-temporal variations in the composition of the ground substrate are crucial regarding the response of ground temperatures to changes in atmospheric conditions (Staub et al., 2015).

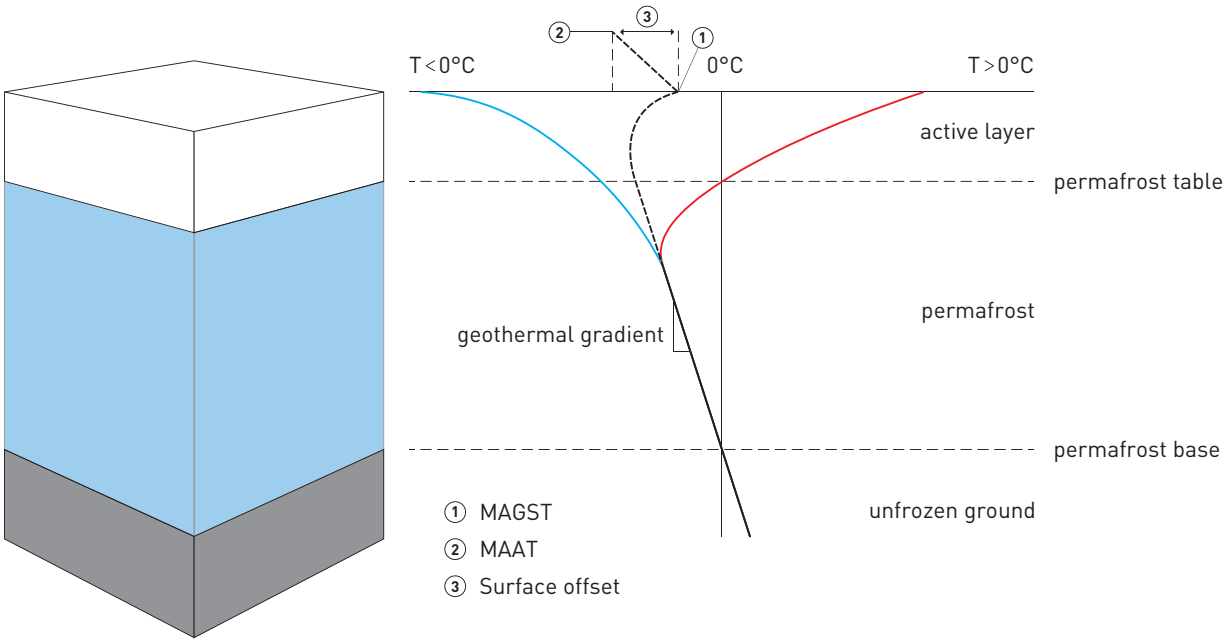

Figure 2.2: Schematic profile of the ground thermal regime in permafrost, illustrating annual maximum and minimum temperatures, active layer, permafrost table, permafrost base, geothermal gradient, MAGST (①), MAAT (②) and surface offset (③). Modified from Noetzli and Gruber (2005), Osterkamp and Burn (2003) and Smith and Riseborough (2002).

As result of these processes, the uppermost ground layer in permafrost terrain is subject to seasonal thawing and refreezing due to its direct contact with the atmosphere (Bonnaventure

& Lamoureux, 2013). The thickness of this *active layer* is thermally defined as a function of the maximum depth of the 0°C isotherm in summer, whereas thaw progression is mainly controlled by the surface energy balance, topo-climatic factors, composition of the ground and three-dimensional effects (Noetzli et al., 2007; Zenklusen Mutter & Phillips, 2012). The upper boundary of permafrost is at the base of the active layer, and the base of permafrost occurs where ground temperatures rise above 0°C at depth as a result of the geothermal gradient (Osterkamp & Burn, 2003). Figure 2.2 shows a schematic profile of ground thermal regime in permafrost.

3 Data and study sites

3.1 Ground surface temperature measurements

In Alpine terrain, an extensive set of measured GST time series is available. Moreover, the amount of ongoing GST measurements in the context of permafrost monitoring is unique. The GST time series analyzed in this thesis were collected from various monitoring projects: The Swiss Permafrost Monitoring Network (PERMOS), the TEMPS (The Evolution of Mountain Permafrost in Switzerland) project, PermaSense and ARPA VDA (L'Agenzia Regionale per la Protezione dell' Ambiente della Valle d'Aosta). These monitoring projects are described briefly in the following.

The largest part of the analyzed GST measurements comes from PERMOS. PERMOS observes mountain permafrost in the Swiss Alps and has taken root and passed from first steps in the 1990s until today. The main goal of PERMOS is to document the state of permafrost in the Swiss Alps on a long-term basis (Vonder Mühll et al., 2008). PERMOS focuses on borehole and kinematic sites. In addition, GST measurements are performed at most of the observation sites in order to capture the influence of the differing types of surface material

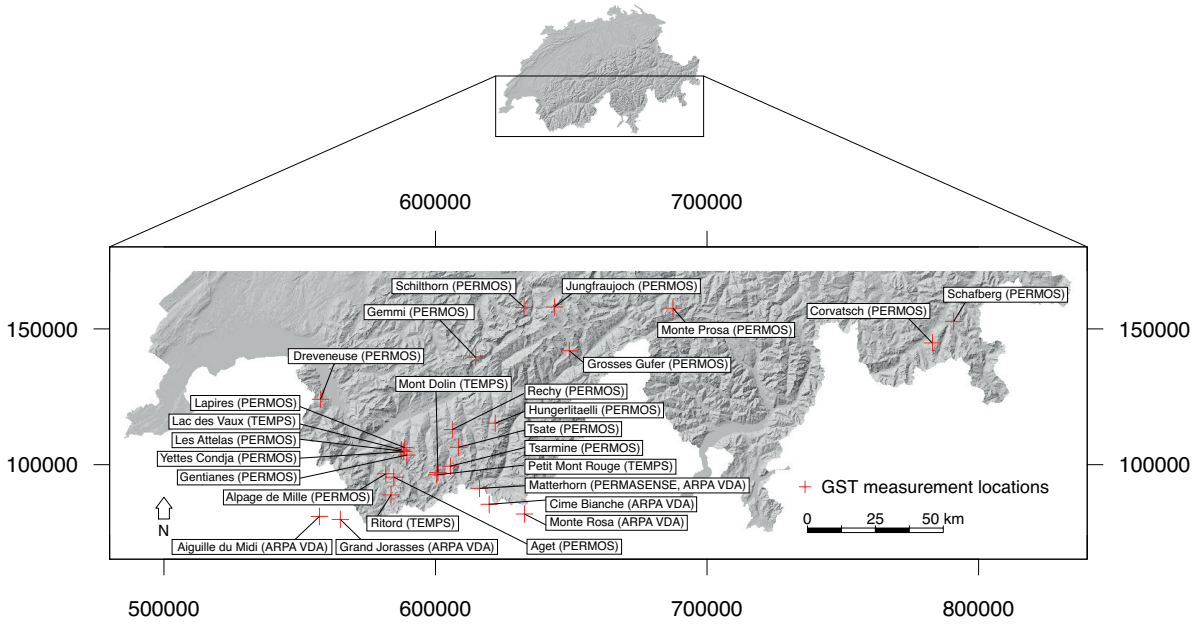

Figure 3.1: Locations of GST measurement sites with corresponding projects given in brackets.

and topographic settings, as well as the spatial variability of the changes. Regarding the GST measurements, the sampling design was only planned for each site. On the scale of the Swiss Alps, the measurement locations are distributed without a higher-level measurement strategy, resulting in a clustered and somehow random distribution of GST measurement locations. Aside from PERMOS, data from the TEMPS project is analyzed. TEMPS was a project funded by the Swiss National Science Foundation (2011 – 2015), carried out by several Swiss partners. Within TEMPS, all available GST time series from various projects were brought together. Table 3.1 describes the sites from PERMOS and TEMPS, where GST time series are measured. See Figure 3.1 for the location of the corresponding sites. Descriptions of the single GST measurement devices are found in Table 7.2, Table 7.3, Table 7.8 and Table 7.10.

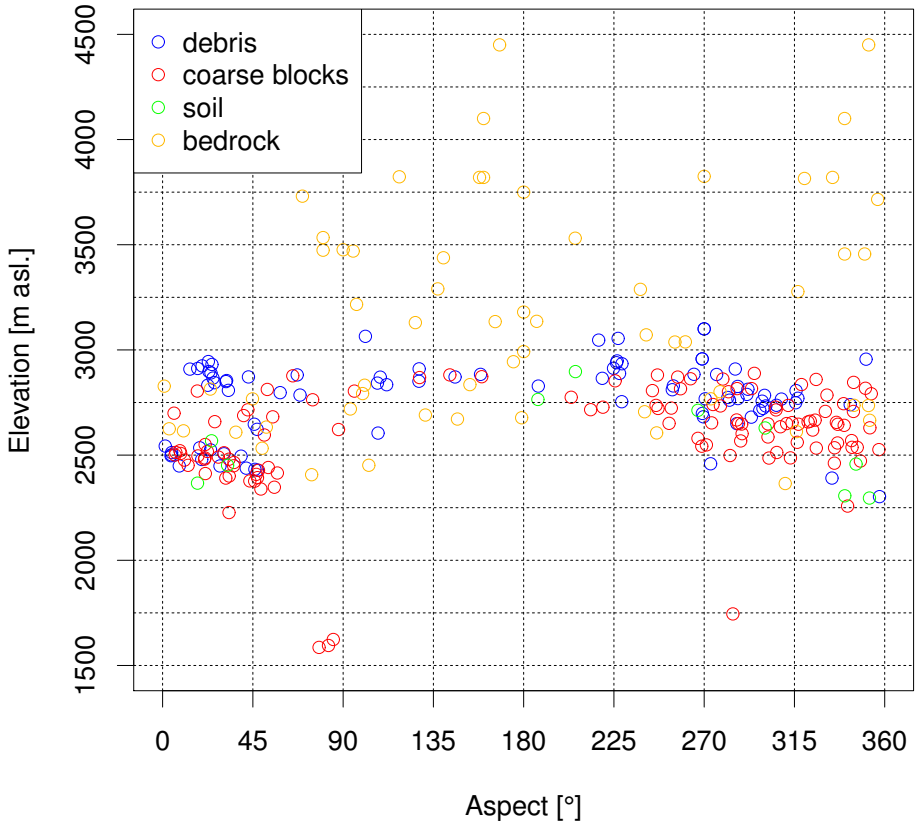

Figure 3.2: Distribution of elevation, aspect and type of surface material from GST measurement devices of which data is analyzed. Because aspect is recorded from the north clockwise, 0° and 360° represent the northern orientation, 90° the eastern orientation, 180° the southern orientation and 270° the western orientation.

In order to complement the data set from PERMOS and TEMPS with GST time series mea-

Table 3.1: Description of PERMOS and TEMPS sites with GST measurements. TEMPS sites are indicated with (T) in the column *Abbr.* Data source: PERMOS.

Abbr	Name	Landforms	Types of surface material	Range of elevation [m asl.]
AGE	Aget	rock glacier	debris, coarse blocks	2800 - 2900
MIL	Alpage de Mille	rock glacier	soil, coarse blocks, debris	2200 - 2500
COR	Corvatsch	rock glacier, talus slope	bedrock, coarse blocks, soil	2500 - 3300
DRE	Dreveneuse	talus slope	coarse blocks	1560 - 1630
GFU	Gemmi	rock glacier, solifluction lobe	soil, coarse blocks, debris	2460 - 2750
GEN	Gentianes	moraine	soil, coarse blocks, debris	2870 - 2895
GGU	Grosses Gufer	rock glacier	debris	2200 - 2700
HUT	Hungerlitaelli	rock glacier	coarse blocks	2500 - 3000
JFJ	Jungfraujoch	crest	bedrock	2850 - 3750
LDV (T)	Lac des Vaux	rock glacier	debris, coarse blocks	2720 - 2800
LAP	Lapires	talus slope	bedrock, coarse blocks, debris, soil	2380 - 2700
ATT	Les Attelas	talus slope	soil, debris, coarse blocks	2620 - 2800
MDO	Mont Dolin	rock glacier, talus slope	soil, debris	2760 - 2860
MPR	Monte Prosa	rock glacier	coarse blocks	2440 - 2520
PMR (T)	Petit Mont Rouge	rock glacier, talus slope	debris, coarse blocks	2590 - 2700
REC	Rechy	rock glacier	bedrock, coarse blocks	2600 - 3100
RTD (T)	Ritord	crest, rock glacier, push moraine, moraine	debris, coarse blocks	2500 - 2900
SBE	Schafberg	rock glacier	coarse blocks	2730 - 2760
SCH	Schilthorn	crest	bedrock, debris	2400 - 3000
TMI	Tsarmine	rock glacier	coarse blocks	2460 - 2600
TSA	Tsate	crest	bedrock, debris	3030 - 3070
YET	Yettes Condja	rock glacier	bedrock, debris, coarse blocks	2600 - 2800

sured at high elevations as well as in steep bedrock, data from the projects PermaSense and ARPA VDA is included. PermaSense is a consortium of researchers and research projects, developing, deploying and operating wireless sensing systems in high-mountain environments. ARPA VDA is a agency for ecological monitoring, located in the Valtournenche valley in northern Italy. Table 7.9 describes the single GST time series from the projects PermaSense and ARPA VDA analyzed in this thesis. Additionally, see Hasler et al. (2011) for a detailed description of the PermaSense field site at Matterhorn.

In total, data from 275 GST measurement locations is analyzed. Figure 3.2 and Figure 3.3 present the distribution of elevation, aspect, slope and type of surface material of these sites. Note that in the data set there is a bias towards northerly exposed devices, slope angles $< 40°$, elevations < 3000 m asl. and coarse blocks as type of surface material. The reasons for this bias are 1) early focus on these sites, 2) easy accessibility and 3) little attention on permafrost in steep bedrock in earlier years.

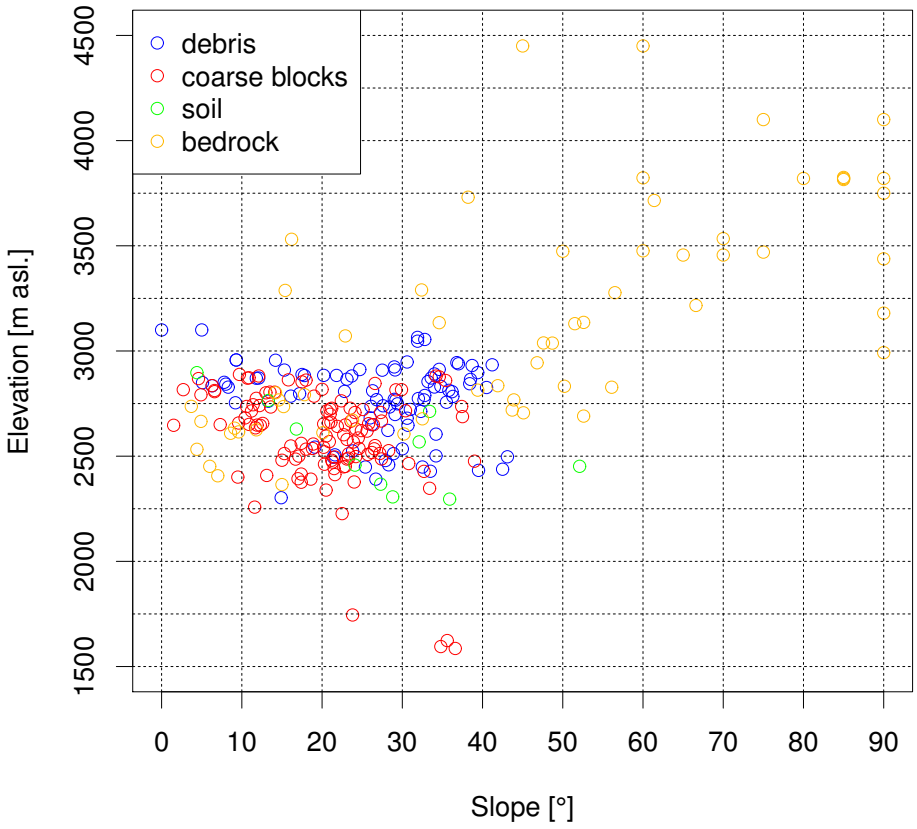

Figure 3.3: Distribution of elevation, slope and type of surface material from GST measurement devices of which data is analyzed.

GST are typically measured 5 – 20 cm below the ground surface in order to prevent exposure of the measurement device to direct solar radiation or wind. GST measurement intervals vary between 10 minutes and 3 hours. The majority of the GST time series analyzed in this thesis are measured with logger types Geotest UTL-1 (± 0.1°C accuracy, 0.23 – 0.27°C resolution), Geotest UTL-3 (< 0.1°C accuracy, 0.02°C resolution), Maxim iButton (± 0.5°C accuracy, 0.0625°C resolution) and Geoprecision M-Log5W (± 0.1°C accuracy, 0.01°C resolution). The application of the loggers UTL-1, UTL-3 and iButton is in soil, debris and coarse blocks, whereas M-Log5W is designed for bedrock.

3.2 Ground temperature measurements

The ground temperature time series studied in this thesis were all measured in the framework of PERMOS. The corresponding GT measurement sites are located around the inner-alpine zone with a focus on Valais and Upper Engadine (Figure 3.4). In total, GT time series from 18 boreholes at 9 different sites are analyzed. All of these boreholes are characterized by coarse blocks or debris as type of surface material and depths ranging between 18 – 101 m (Table 3.2). GT are commonly measured with thermistor chains (e.g. YSI Precision series 44000 and 46000) and automatic logging systems. Typical accuracies ranging from ± 0.01 – 0.2°C. The temporal resolution of GT varies between hourly sampling intervals and time series recorded once a day.

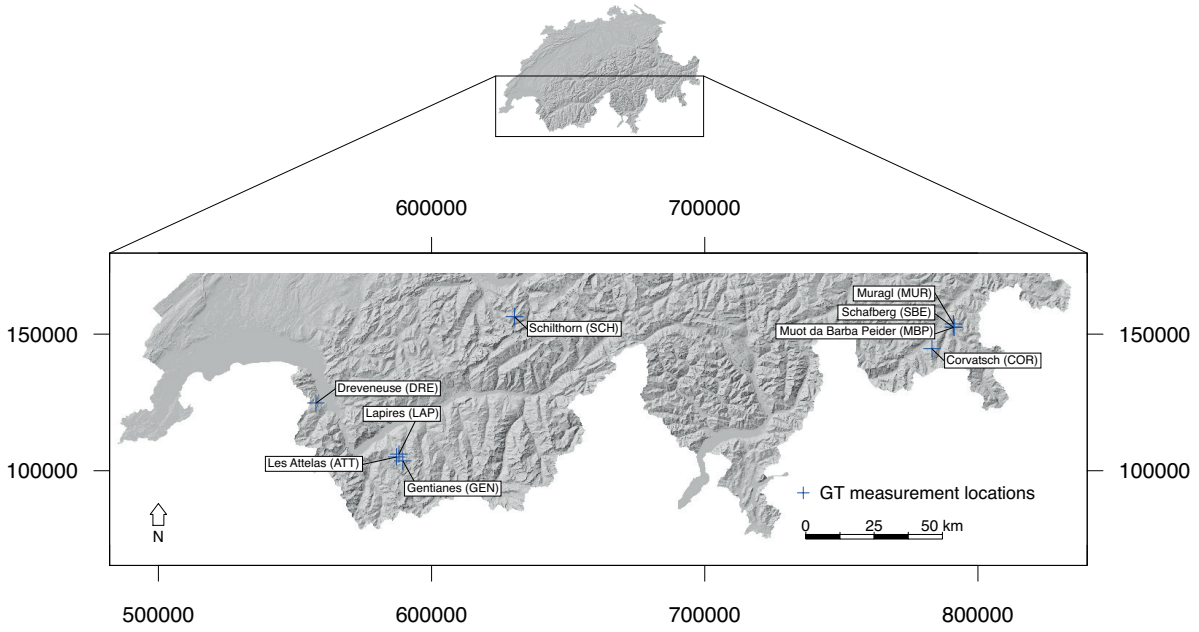

Figure 3.4: Locations of GT measurement sites from PERMOS. The abbreviations used in the naming of the measurement devices are given in brackets.

Table 3.2: Description of borehole sites. Data source: PERMOS.

Name of measurement device	Name	Landforms	Types of surface material	Depth of borehole [m]
ATT_0108	Les Attelas	talus slope	debris	26
ATT_0208	Les Attelas	talus slope	coarse blocks	21
COR_0200	Corvatsch	rock glacier	coarse blocks	63
COR_0287	Corvatsch	rock glacier	coarse blocks	62
DRE_0104	Dreveneuse	talus slope	coarse blocks	15
GEN_0102	Gentianes	moraine	debris	20
LAP_0198	Lapires	talus slope	coarse blocks	20
LAP_1108	Lapires	talus slope	coarse blocks	40
LAP_1208	Lapires	talus slope	coarse blocks	35
MBP_0296	Muot da Barba Peider	talus slope	debris	18
MUR_0199	Muragl	rock glacier	coarse blocks	70
MUR_0299	Muragl	rock glacier	coarse blocks	64
MUR_0499	Muragl	rock glacier	coarse blocks	71
SBE_0190	Schafberg	rock glacier	coarse blocks	67
SBE_0290	Schafberg	rock glacier	coarse blocks	60
SCH_5000	Schilthorn	crest	debris	101
SCH_5198	Schilthorn	crest	debris	14
SCH_5200	Schilthorn	crest	debris	100

3.3 Air temperature measurements

To study the coupling between GST and air temperature, meteorological data for all of the GST measurement sites is required. For this thesis, time series of absolute temperature values [°C] are provided by MeteoSwiss for all of the GST measurement locations for hydrological years 1995 – 2015. These time series are computed based on a grid-data product from MeteoSwiss: `TanomM8110` is a spatial analysis of deviations of monthly mean temperature from the climatological norm (1981 – 2010). It is based on homogeneous time series at about 80 stations, spatially interpolated to a regular grid. Because of its long-term consistency, it is suited for trend analysis (MeteoSwiss, 2013). Based on TanomM8110, absolute temperature values [°C] are computed in a first step, resulting in a gridded data product with 2.2 km resolution. Subsequently, the additional interpolation to the locations of the GST measurement devices is obtained by linear regression with elevation.

4 Methods

4.1 Gap filling

In order to maximize the amount of complete time series, the input data is first preprocessed. A prerequisite for analyzing GST time series is to ensure completeness of the individual time series. Often, statistical analyses are only applicable if time series are not affected by gaps of any length. However, the majority of the GST time series of PERMOS and TEMPS are affected by gaps with lengths of hours to years. Therefore, a recently introduced gap filling algorithm for ground surface temperature data developed by Staub et al. (accepted) is applied to the daily aggregated GST values of PERMOS and TEMPS first. Thereby, the aim is to maximize the amount of valid data in order to enable 1) the application of different statistical analyses and 2) reasonable calculations of aggregates and indices (Staub et al., accepted). This gap filling algorithm fills gaps with daily GST values. Gaps of a few days duration are filled by linear interpolation. Longer gaps of up to several months are filled with the quantile mapping (QM) method. The basic principle of the QM method is to fill the gap of a particular time series with data of another time series measured in the same interval. The QM method is based on the empirical cumulative distribution function (CDF) of the data (Gudmundsson et al., 2012): Given a time series with a gap, the aim is to search for another time series without gaps in the corresponding interval, so that the cumulative distributions of the data from the two time series closely resemble each other. See Staub et al. (accepted) and Gudmundsson et al. (2012) for a detailed description of the QM technique.

Once the gap filling algorithm is applied, the time series have to be divided in usable and unusable according to the uncertainty of the filled data. Because gap filled data in the context of this thesis is solely used to compute annual aggregates, this separation is done for each hydrological year of a particular time series: The uncertainty of the filled data is estimated for each hydrological year of a certain time series. Subsequently, the data is classified according to a threshold. Based on the measurement uncertainty of the loggers, this threshold ϵ_{Hyear} is set to 0.25°C. Accordingly, every hydrological year of a certain time series whose filled data has an uncertainty of < 0.25°C is determined as usable.

The uncertainty of the filled data is estimated as follows: For every filled value within a gap, the gap filling algorithm simultaneously estimates the corresponding uncertainty. Given a particular time series, these uncertainties are used to calculate the mean uncertainty of the filled data for each hydrological year. Following the approach of Staub et al. (accepted), ϵ_{Hyear} can be calculated as

$$\epsilon_{Hyear} = \pm \left(\frac{\sum_{i=1}^{n_{sto}} \epsilon_{sto,i}}{365 \times \sqrt{n_{sto,i}}} + \frac{\sum_{i=1}^{n_{sys}} \epsilon_{sys,i}}{365} \right) \tag{4.1}$$

where ϵ_{sto} are the stochastic and ϵ_{sys} the systematic errors, n_{sto} and n_{sys} the numbers of filled values within a hydrological year and i the days with filled values. ϵ_{Hyear} can be divided in stochastic and systematic errors. According to Staub et al. (accepted), stochastic errors are assumed to occur 1) when filling a short gap by linear interpolation or 2) when applying the QM method in summer. Opposite, systematic errors most likely occur due to the influence of a snow cover, resulting from the application of the QM method during winter months.

4.2 Derived indices

To analyze the data, the GST measurements taken in different time intervals have to be aggregated to certain levels of temporal resolution, depending on the method used in the analysis. Additionally, the aggregated temperature measurements can be used to calculate certain indices, containing supplementary information according to the averaged temperature measurements. Two GST related indices are used in this thesis: MAGST and the surface offset (SO). MAGST is a meaningful measure describing the thermal regime at the ground surface. It is defined and calculated as the mean of the daily mean ground surface temperature within a hydrological year. In the context of this thesis, aggregated indices on a yearly basis always correspond to the hydrological year (October 1st to September 30th). Unless specifically mentioned, hydrological years are indicated with the date of the second calendar year. The SO, a measure introduced by Smith and Riseborough (2002), describes the coupling between the lower atmospheric conditions and the ground. It is computed as

$$SO = MAGST - MAAT \tag{4.2}$$

and is often described as a function of surface characteristics and topography (Hasler et al., 2015). If MAGST is lower than MAAT, SO is negative, pointing to cooling processes at the ground surface. On the other hand, SO is positive when MAGST is higher than MAAT. A positive SO is typically found in steep and south oriented rock walls. Thereby, solar irradiation is high due to steep angles of incidence and thus leading to higher MAGST relative to MAAT.

4.3 Simple linear regression

4.3.1 Data description

To quantify the current temperature trends at the ground surface, GST time series with lengths of 15 hydrological years (2000 – 2014) are selected. The number of complete time series after gap filling is 36. Because of the gap filling approach and the consequential uncertainties regarding daily values, mean daily GST values are annually aggregated in the context of trend estimation. A simple linear regression model is applied with time as the explanatory variable. In order to account for possible seasonal warming and different influencing factors throughout the year, trends are computed for complete hydrological years as well as winter (December, January, February), spring (March, April, May), summer (June, July, August) and autumn (September, October, November). Note that in the context of this thesis, all statistical analyses are performed with R (R Core Team, 2015). In addition, the mean absolute error (MAE) is calculated according to equation 4.3 for each GST and AT time series to quantify the mean inter annual variation of the time series. Thereby, y_i stands for the MAGST of a certain year and $\overline{y}_i$ represents the mean MAGST of all hydrological years between 2000 – 2014.

$$MAE = \frac{1}{n}\sum_{i=1}^{n}|y_i - \overline{y_i}| \tag{4.3}$$

4.3.2 Methodology

Simple linear regression (SLR) provides the analysis of direct causal relations between a dependent (response) and independent (explanatory) variable. To describe this functional relationship, a model in the form of an equation can be formulated. This model is then fitted to the data. The model for SLR is

$$Y = \beta_0 + \beta_1 X + \varepsilon \tag{4.4}$$

where Y is the response variable, X the explanatory variable, β_0 and β_1 the regression coefficients and ε the random error (Schuenemeyer & Drew, 2010). Note that the linear relationship implies, that changes in the response variable are always proportional to changes in the explanatory variables. Many statistical procedures exists to fit a model to the data. In the context of this thesis, the classical procedure called *ordinary least squares* (OLS) is applied. Given a fitted model $\hat{Y}_i = \hat{\beta}_0 + \hat{\beta}_1 X_i, i = 1, ..., n$, OLS minimizes

$$\sum_{i=1}^{n} e_i^2 = \sum_{i=1}^{n}(Y_i - \hat{Y}_i)^2 = \sum_{i=1}^{n}(Y_i - \hat{\beta}_0 + \hat{\beta}_1 X_i)^2 \tag{4.5}$$

where $\hat{Y}_i$ is the predicted value for Y, Y_i the observed value of Y and e_i the estimate of ε_i, the true error at the ith observation Y_i (Figure 4.1). To estimate the model parameters β_0 and

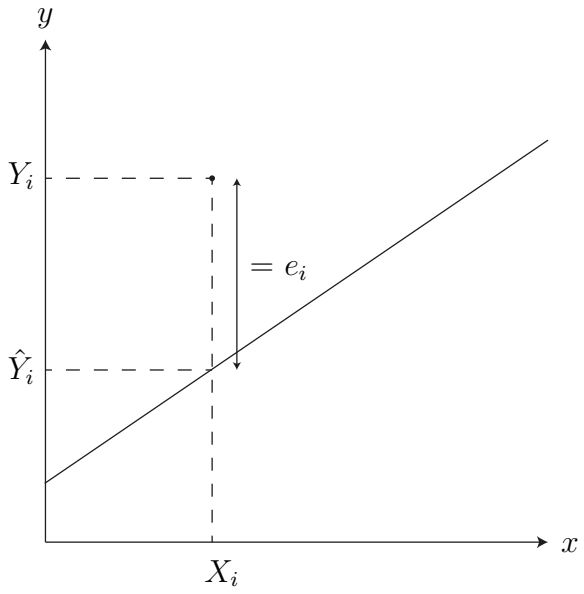

Figure 4.1: Schematic illustration of $e_i = (Y_i - \hat{Y}_i)$, the true error at the ith observation Y_i.

$\beta_1 X$, equation 4.5 has to differentiate with respect to $\hat{\beta}_0$ and $\hat{\beta}_1$. The resulting parameter estimates are

$$\hat{\beta}_1 = \frac{\sum_{i=1}^{n}(X_i - \overline{X})(Y_i - \overline{Y})}{(X_i - \overline{X})^2} \tag{4.6}$$

$$\hat{\beta}_0 = \overline{Y} - \hat{\beta}_1 \overline{X} \tag{4.7}$$

where $\overline{X}$ and $\overline{Y}$ are the means of X and Y (Stahel, 2008). Thereby, $\hat{\beta}_0$ from equation 4.7 is called the intercept, representing the intersection of the regression line with the y-axis. $\hat{\beta}_1$ is the regression coefficient of X_i and presents the slope of the regression line. Note that the absolute magnitude of the trend is defined here as the difference between the fitted value at the end ($\hat{Y}_n$) and the beginning ($\hat{Y}_1$) of a time series. After fitting the model to the data, it is critical to evaluate if the model is satisfactory for the job asked of it. A common goodness-of-fit statistic is the *coefficient of determination* R^2. The coefficient of determination is the fraction of total variability accounted for by the model (Schuenemeyer & Drew, 2010). It is

defined as

$$R^2 = \frac{SSR}{SST} = \frac{\sum_{i=1}^{n}(\hat{Y}_i - \overline{Y})^2}{\sum_{i=1}^{n}(Y_i - \overline{Y})^2} = 1 - \frac{SSE}{SST} = 1 - \frac{\sum_{i=1}^{n}(Y_i - \hat{Y}_i)^2}{\sum_{i=1}^{n}(Y_i - \overline{Y})^2} \tag{4.8}$$

where SSR is the *sum of squares due to regression*, SSE the *sum of squares due to error*, SST the *total sum of squares* and $0 \leq R^2 \leq 1$ (Ernste, 2011; Schuenemeyer & Drew, 2010). If R^2 is close to 1, the response variable is explained to a large degree by the explanatory variable. In contrast, if R^2 is close to 0, the variability of the dependent variable is little explained by the independent variable.
In the context of model evaluation, the respective model assumptions have to be reviewed. In least-squares regression, the key assumptions is $\varepsilon_i \sim N(0, \sigma_\varepsilon^2)$: Errors (residuals) are independent and normally distributed with zero mean and constant variance. In this thesis, the model assumptions are examined by means of descriptive statistics and graphs.

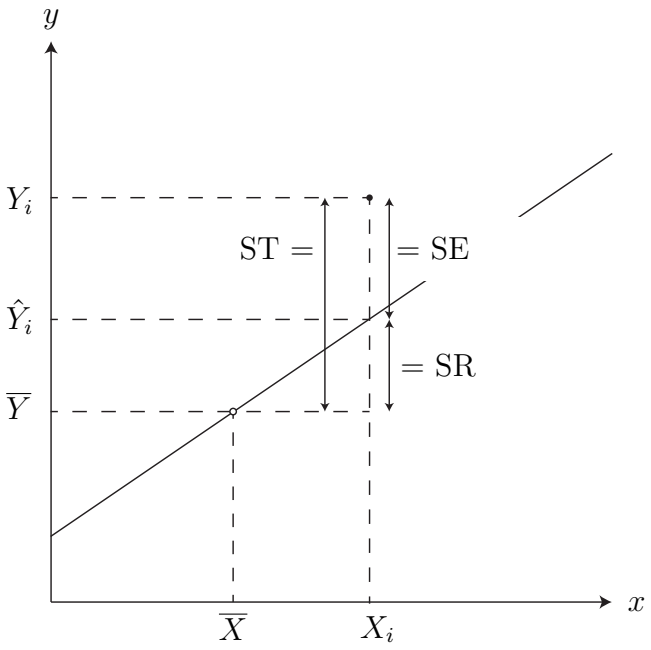

Figure 4.2: Schematic illustration of the partition of total variability based on a SLR model. The square due to error (SE) is $(Y_i - \hat{Y}_i)^2$ and represents the variability which is not explained by the SLR model. The square due to regression (SR) is $(\hat{Y}_i - \overline{Y})^2$ and stands for the variability explained by the SLR model. The total square (ST) is $(Y_i - \overline{Y})^2$ and represents the total variability.

4.3.3 Monte Carlo method and homogeneity

The outcomes of trend analysis can be influenced by the serial auto-correlation of the data. Previous studies have shown, that the null hypothesis of no trend is rejected more often than specified by the significance level if the data from time series is serially correlated (Bayazit & Önöz, 2007; Yue & Wang, 2002). This effect can be overcome by eliminating the lag-1 auto-correlation (von Storch, 1995), which is known as *prewhitening*. Because GST time series do not exhibit lag-1 auto-correlation (Figure 5.4, Figure 5.6), the data is not prewhitened.

In the context of trend analysis of GST time series, uncertainties from various sources should be taken into account. The influence of these uncertainties on estimated trends can be studied by means of the Monte Carlo method (MCM). Figure 4.3 illustrates the schematic functionality of the MCM, as it is applied in the context of this thesis: Given a GST time series, a normal distribution with 1000 random values is modeled around each measured MAGST. Thereby, μ is the measured MAGST and σ represents the standard deviation including all uncertainties. Subsequently, trends are calculated for each of the 1000 modeled time series. The range of these trends reflects the possible range of the trend from the measured data as a consequence of the influence of the different uncertainties. This approach is repeated for each GST time series, resulting in solid indications regarding the reliability of the estimated trends.

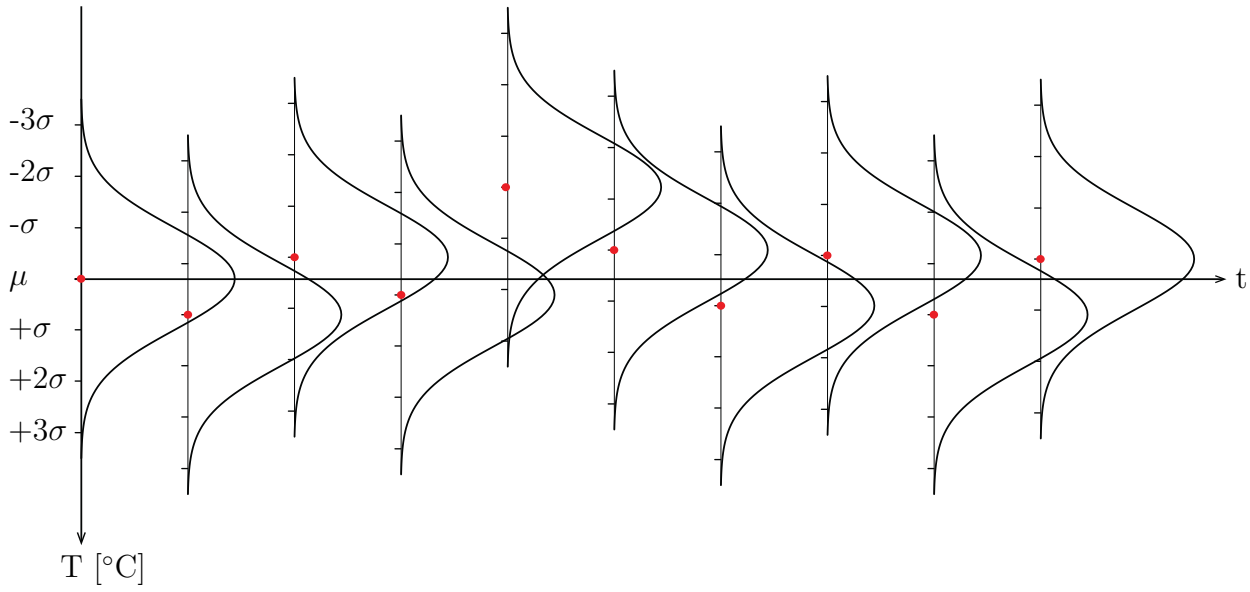

Figure 4.3: Schematic illustration of the Monte Carlo method (MCM) used in trend analysis. The curves stand for the normal distribution of the modeled MAGST with σ as the standard deviation including all uncertainties and with μ as the measured MAGST, representing the mean of the normal distribution.

Three different uncertainties are considered in the framework of trend estimation. The first

uncertainty refers to the measurement uncertainty of the loggers. The measurement uncertainty is defined as ± 0.25°C, which corresponds to the mean resolution of the UTL-1 loggers. On the one hand, the resolution of UTL-1 loggers is the most imprecise among all of the measurement devices used to measure GST. On the other hand, the UTL-1 loggers are the most widespread within the monitoring network of PERMOS. For this reason, a measurement uncertainty of ± 0.25°C (σ = 0.083°C) is considered appropriate, although this value is on the conservative side with regard to the resolutions of newer measurement devices.

The second uncertainty considered in the MCM refers to the gap filling algorithm applied in the preprocessing of the data (Section 4.1). Because some of the 15 years long time series contain filled gaps, the uncertainty from the gap filling procedure has to be incorporated. The uncertainty due to the gap filling is defined as ± 0.25°C (σ = 0.083°C), which is identical with the threshold value used to select the output data from the gap filling algorithm.

The third uncertainty refers to the homogeneity of the time series. Long climatological time series can contain variations due to non-climatic factors, which can distort or hide the true climate signal (Begert et al., 2005). Because possible inhomogeneities due to site relocation or changes in instrumentation can lead to misleading results, it is important to analyze homogenized time series in the context of changing atmospheric conditions. Although this issue is well-established in climatology, it receives little attention in the context of GST. Two factors argue against possible inhomogeneities in GST time series: 1) GST time series are calibrated at the zero curtain after the retrieving of the data and 2) measurement locations are not relocated horizontally. In contrast, vertical displacements likely occur while measuring GST. Because the measurement devices have to be dug up in order to access the data and need to be buried afterwards, changes in depth cannot be excluded. Because changes in depth lead to steps in the time series independent of changing environmental conditions, they have to be considered in trend analysis. Figure 7.3 presents MAGT from borehole `Ritigraben 0102` at depths of 0.1, 0.2 and 0.4 m. Given ± 10 cm as the range for possible changes in depth, the mean difference between MAGT measured in depth of 10 cm and MAGT measured in 20 cm depth is 0.082°C (Table 7.7). Therefore, the uncertainty in consideration of possible inhomogeneity is defined as 0.1°C (σ = 0.033°C). Adding the three uncertainties, the standard deviation in modeling the normal distribution around the measured MAGST results in 0.12°C.

4.4 Multiple linear regression

4.4.1 Data description

The influence of topographic parameters, type of ground surface material, snow cover and different regions on the spatial variability of MAGST is analyzed by means of a multiple linear regression model. For the hydrological years 2005 – 2014, every year without gaps is selected from the available data set to compute MAGST, leading to 1531 MAGST values

from 275 measurement locations at 27 sites. Subsequently, several outliers are removed. On the one hand, these are northward exposed sites with elevations > 3700 m asl. and slope angels > 45°, leading to extraordinary low MAGST. On the other hand, data from southward and eastward exposed measurement locations with elevations > 2600 m asl. and slope angles > 30° were also excluded due to extraordinary high MAGST relating to the elevation. Note that the exclusion of these measurement devices was required due to the sparse availability of such measurements rather than the extreme nature of the corresponding measurement locations. In addition, all measurement locations of the site `Dreveneuse` are excluded due to strong ventilation effects in the blocky surface material at the site. At last, all 3 measurement locations from the central Main Alpine Ridge are excluded. See Section 4.4.3 for more explanation. Finally, 1439 MAGST values from 260 measurement locations at 24 sites are used as training data to fit the multiple linear regression model.

In order to quantify the mean spatial variability of GST, the MAE is computed according to 4.3 at selected sites for hydrological years 2007 – 2011. Thereby, y_i stands for the MAGST of a certain GST measurement device and $\overline{y}_i$ represents the mean MAGST of all loggers at the corresponding site. The selected sites `Ritord` (100 measurements, 21 loggers), `Gemmi` (88 measurements, 23 loggers) and `Alpage de Mille` (83 measurements, 18 loggers) are chosen, because 28 of the 36 time series studied in the trend analysis originate from these sites. Therefore, the temporal variability can be compared with the spatial variability in a meaningful way.

4.4.2 Methodology

In the case that there is more than one explanatory variable, a multiple regression model is formulated. Many of the model procedures for formulation and fitting are equal to those in SLR. Therefore, see Section 4.3.2 for detailed explanation. The model for *multiple linear regression* (MLR) is

$$Y = \beta_0 + \beta_1 X_1 + \beta_2 X_2 + ... + \beta_k X_k + \varepsilon \tag{4.9}$$

where Y is the response variable, X_i the explanatory variables for $i = 1, ..., k$, k the number of explanatory variables and ε the random error (Ernste, 2011). Like in the SLR, the model coefficients are estimated by means of OLS. See Stahel (2008) for a detailed description of the mathematical derivation regarding the estimation of the model coefficients. In the context of MLR, the R^2 has to be adjusted to the number of explanatory variables. When an additional explanatory variable is added to a MLR model, R^2 may increase even if the new variable is not statistically significant (Schuenemeyer & Drew, 2010). To compensate

for this bias, the *adjusted* R^2

$$R^2_{adj} = 1 - \frac{\sum_{i=1}^{n}(Y_i - \hat{Y}_i)^2/(n-m-1)}{\sum_{i=1}^{n}(Y_i - \overline{Y})^2/(n-1)} = 1 - (1-R^2)\frac{n-1}{n-m-1} \tag{4.10}$$

is computed, where m is the number of regression coefficients and n the number of observations (Ernste, 2011). Note that $R^2_{adj} < R^2$ and that R^2_{adj} can be negative (Ernste, 2011).

4.4.3 Explanatory variables

Based on the physical processes influencing GST on different scales (Section 2.2), the explanatory variables of the model are selected. The model contains the explanatory variables elevation, slope, aspect, type of surface material, mean annual snow index, region, hydrological year and the interaction between aspect and slope. A step-wise model reduction according to the Akaike-Information-Criteria (Akaike, 1974) did not result in a reduction of explanatory variables. In the context of the surface energy processes, *elevation* is a proxy for air temperature, which is largely dominated by the net radiation (Hoelzle et al., 2001; Ohmura & Raschke, 2005). *Slope* and *aspect* as well as the corresponding interaction account for the dependence of direct solar radiation on terrain geometry. To ensure continuity, sine and cosine of the aspect are taken. Because cosine of 0° is 1 respective -1 for 180°, it represents north-south differences. In contrast, sine of 90° is 1 respective -1 for 270°. For this reason, sine represents east-west differences. The *type of surface material* includes the ground cover types soil, debris, coarse blocks and bedrock. Note that the transition from debris to coarse blocks is continuous and no explicit definition regarding the differentiation exists. Additionally, the classification of the data used in this thesis is done by several scientists. Hence, inconsistent classifications are likely to be present in the data. *Mean annual snow index* (MASI) represents an approximation for the thermal insulation effect of the snow cover. In the context of this thesis, the data processing technique suggested by Staub and Delaloye (2016) is applied to include the insulation effect of the snow cover in the model. Based on weekly variations of GST, the authors compute an index [0,...,1] for the thermal insulation effect of the snow cover for each day. Thereby, 0 stands for an inexistent snow cover and 1 indicates complete thermal insulation. Based on these daily values, mean annual snow index values are computed. The explanatory variable *region* is introduced to investigate whether the thermal regime at the ground surface differs significantly in different Alpine regions. Based on climatological criteria, *region* divides the measurements locations in different large-scale regions (Figure 7.8): The western Main Alpine Ridge (MAR), the eastern MAR and the western Northern Alpine Ridge (NAR). These large-scale regions are adapted from the WSL Institute for Snow and Avalanche Research SLF, where they are used for the avalanche bulletin. For the sake of simplicity, the measurement devices located in the inneralpine regions are added to the MAR. Because the amount of data from the central MAR is very small compared with the other regions, all 3 measurement locations from the

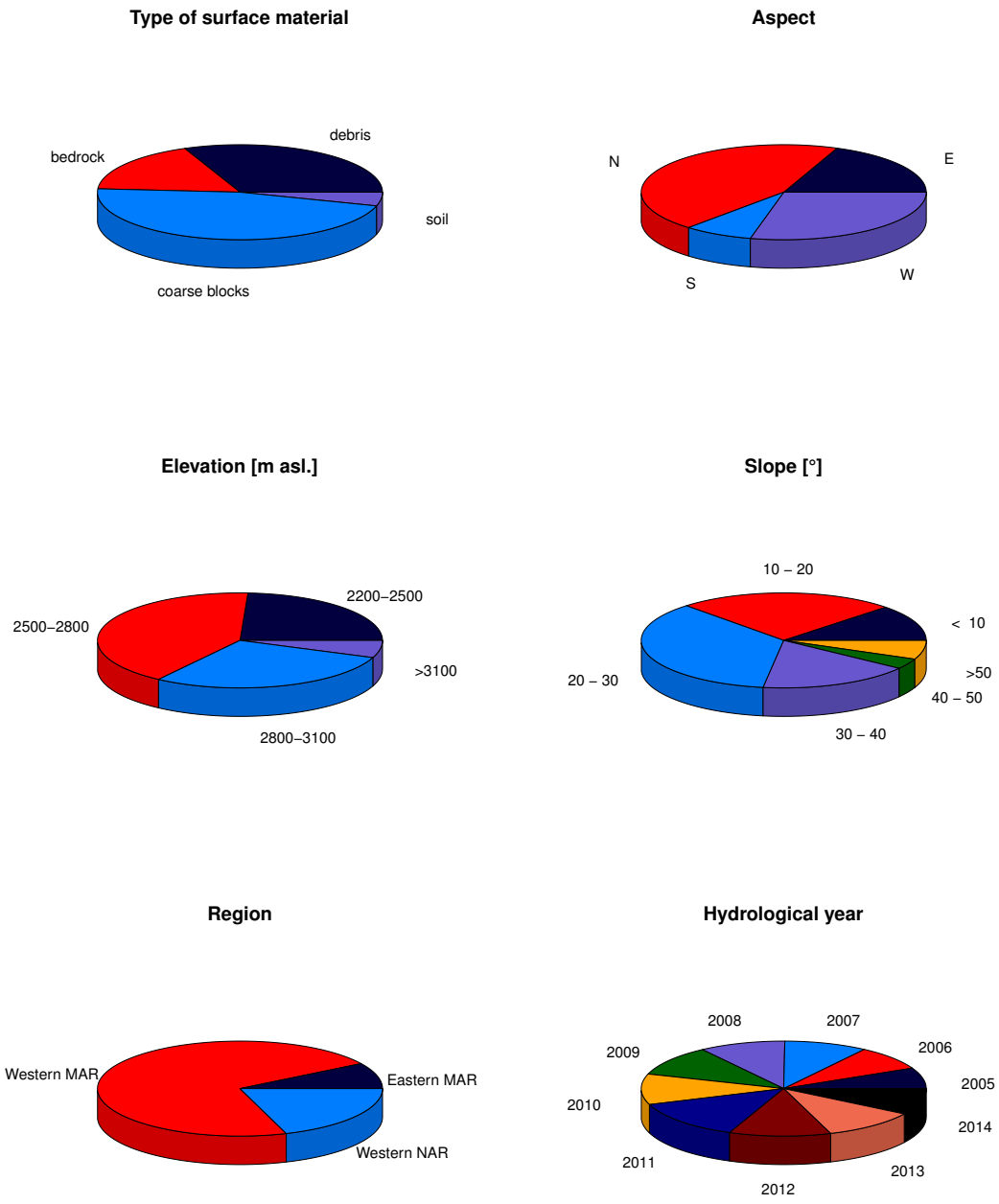

Figure 4.4: Frequency distribution of selected explanatory variables used as training data for the multiple regression model. The size of the circles correspond to the metadata of 1439 MAGST values.

central MAR (16 MAGST values) are excluded due to the lack of representativeness. Given the time period between hydrological years 2005 – 2014, *hydrological year* indicates the year of data acquisition. Figure 4.4 presents the frequency distribution of selected explanatory variables.

4.5 Correlation

4.5.1 Data description

To study the temporal similarity of GST and GT time series, Spearman's rank correlation coefficient r_{Sp} is calculated. Generally, the distribution of normalized data is altered toward a normal distribution (Grumm & Hart, 2001). However, histograms of the normalized daily temperature values of GST and GT time series indicate isolated deviations from the expected normal distribution. This is why the Pearson correlation, which is rooted in the two-dimensional normal distribution, is not applied in this context.

To analyze the temporal similarity of GST time series, 81 complete time series with a length of 4 subsequent hydrological years (2011 – 2014) are selected (Table 7.10). Then, the Spearman's rank correlation coefficient r_{Sp} is calculated for every possible pair. Correlation analysis in this context is based on daily values. For this reason, uncertainties in connection with gap filling are considered to have a major impact on the result. This is why GST time series with gaps are excluded. 18 GT time series (Table 7.13) with depths ranging between 0.5 and 1.2 m are selected to study the temporal similarity of GST and GT time series. Subsequently, every GT time series is correlated with the 81 GST time series mentioned above. Note that any of the GT time series is complete between hydrological years 2011 – 2014. In order to deal with this complication, the gaps of the GT time series are transferred to the GST time series before the computation of the Spearman's rank correlation coefficients.

4.5.2 Methodology

The concept of correlation describes the association between two random variables. *Covariance* is a measure of linear association between two random variables X and Y. The covariance is estimated as

$$\widehat{Cov}(X,Y) = \sum_{i=1}^{n} \frac{(X_i - \overline{X})(Y_i - \overline{Y})}{n-1} \tag{4.11}$$

where $\overline{X}$ and $\overline{Y}$ are the sample means (Schuenemeyer & Drew, 2010). However, the covariance measures the linear association even if the units of measurements of the random variables are different. This rarely makes sense. As a consequence, the covariance is generally divided by the standard deviation, which results in a standardized measure called the *correlation*. The correlation coefficient therefore represents an dimensionless measure for the

linear association. For two random variables X and Y, the sample correlation coefficient is defined as

$$\rho_{x,y} = \frac{\widehat{Cov}(X,Y)}{\sqrt{\sigma_x^2 \sigma_y^2}} = \frac{\sum_{i=1}^{n}(X_i - \overline{X})(Y_i - \overline{Y})}{\sqrt{\sum_{i=1}^{n}(X_i - \overline{X})^2 \sum_{i=1}^{n}(Y_i - \overline{Y})^2}} \tag{4.12}$$

where $\widehat{Cov}(X,Y)$ is the covariance of X and Y, σ_x^2 and σ_y^2 the variances of X and Y and $\overline{X}$ and $\overline{Y}$ the sample means (Schuenemeyer & Drew, 2010). Correlation coefficients imply two main characteristics. Firstly, correlation coefficients are always located between -1 and +1. Secondly, if the sign of the coefficient is positive, a higher value of Y can be expected given a high value of X. If the sign is negative, a lower value of Y can be expected given a high value of X. As mentioned above, histograms of the data indicate deviations from normal distribution. Therefore, the Spearman's rank correlation coefficient is computed, which can be applied in case of nonparametric distribution of the data. In place of the original variables X and Y, the Spearman's rank correlation coefficient uses their ranks. Each measured value x_i gets a rank $R_{x,i}$ and each measured value y_i a rank $R_{y,i}$. Transforming the values $x_1, ..., x_n$ to the ranks $1, 2, ..., n$, the distributions of the variables X and Y are ignored. To compute Spearman's rank correlation coefficient, the same formula as in equation 4.12 can be used (Schuenemeyer & Drew, 2010). Hence, the Spearman's rank coefficient is defined as

$$r_{Sp} = \frac{\sum_{i=1}^{n}(R_{x,i} - \overline{R}_x)(R_{y,i} - \overline{R}_y)}{\sqrt{\sum_{i=1}^{n}(R_{x,i} - \overline{R}_x)^2 \sum_{i=1}^{n}(R_{y,i} - \overline{R}_y)^2}} \tag{4.13}$$

4.5.3 Normalization and lag correction

The computation of Spearman's rank correlation coefficient requires independent measurements. However, GST and GT time series exhibit a strong seasonal pattern, following the variations of AT throughout the year. Therefore, raw data of GST and GT time series is dependent: Measurements with a short time interval in between are more likely to be similar than measurements with a long time interval in between. To remove this serial autocorrelation, the variables within each time series have to be normalized in order to get a constant mean and variance of time. In atmospheric sciences, this transformation toward a stationary time series is achieved by computing standardized anomalies (Wilks, 2006). Based on this method, the time series are normalized on a monthly basis by

$$z = \frac{x - \bar{x}}{s_x} \tag{4.14}$$

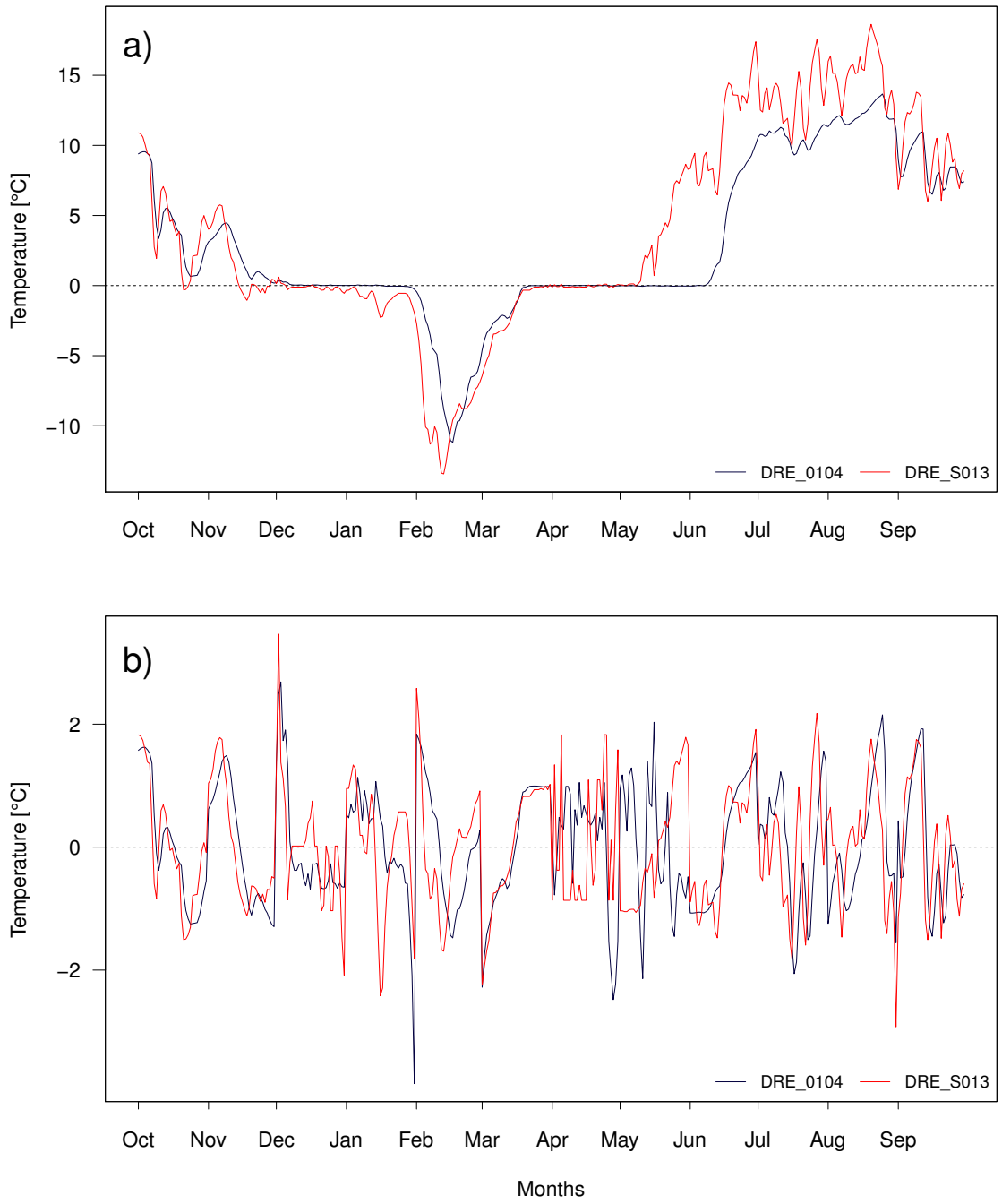

Figure 4.5: Example of GST (red) and GT (blue) time series for the hydrological year 2012 without (**a**)) and with (**b**)) normalization of the data. The GT time series is measured in 1.2 m depth.

where z is the standardized anomaly, x the raw temperature value, $\bar{x}$ the mean of the corresponding month and s_x the standard deviation of the corresponding month. See Figure 4.5 for an example of GST and GT time series without and with normalization.

The rate of heat conduction from the ground surface into the ground depends on the soil constituents. In any case, temperature signals are delayed with increasing depth. As a consequence, these lags have to be considered when correlating GST and GT time series. In order to analyze the depth, where the delay of the temperature signal is ≥ 1 day, cross-correlation coefficients are computed between GST and GT time series for differences in depth of 0.5, 0.7, 1.0 and 1.2 m. With a *cross-correlation function* the correlation between two stationary time series at different lags can be computed (Cowpertwait & Metcalfe, 2009). Such a procedure is implemented by the R function *ccf* (R Core Team, 2015). Table 7.14 presents the maximum cross-correlation coefficients with their corresponding lags. At a depth of 1.0 m, the maximum cross-correlation coefficient is found at lag one. In other words, the GT time series is one day delayed compared with the time series at the ground surface. As a consequence, GT time series with depth > 0.8 m were shifted back in time about one day before correlating them with the GST time series.

5 Results

5.1 Characteristics of ground surface temperatures

To study the characteristics of GST in a more qualitative way, 78 GST time series with lengths of 5 subsequent hydrological years are analyzed by means of descriptive statistics. Figure 5.1 **a)** shows differences > 10°C of MAGST between different types of surface material. These differences are primarily driven by heterogeneity in altitude and exposition to the sun and secondarily by variable snow conditions between measurement sites within a particular type of surface material. Using the example of minimum and maximum MAGST within the ground cover type classes coarse blocks and steep rock for the hydrological year 2010, these differences can be explained by the location of the respective measurement devices. Whereas `JFJ_R005` is situated at an altitude of 3715.5 m asl. and is northward orientated, `COR_R009` is situated at an altitude of 2853 m asl. and exhibits a southward orientation (Table 7.2). Based on these distinctions, MAGST of `JFJ_R005` is 13°C lower than MAGST of `COR_R009`. On the other hand, `ATT_S022` is located at an altitude of 2649.9 m asl. and is westwards orientated, whereas the location of `DRE_S015` has an altitude of 1623.5 m asl. and is eastwards orientated (Table 7.2), inducing a difference in MAGST of almost 9°C. Note that in the context of this thesis, *flat rock* is defined as bedrock with a slope < 30°, whereas *steep rock* is defined as bedrock with a slope ≥ 30°. See Section 6.5 for explanation.

Figure 5.1 **b)** presents inter-annual differences of MAGST and MAAT. For hydrological years 2010 – 2014, absolute differences range between ± 2°C. In steep rock, inter-annual changes of MAGST generally follow inter-annual changes of MAAT, i.e. higher (lower) MAAT leads to higher (lower) MAGST. Anomalies of these observations occur due to factors like snow cover and clouds, influencing the surface energy balance in steep rock walls. MAGST of the class flat rock is to a lesser extent coupled to MAAT. Whereas changes are positive for both MAGST and MAAT in the second hydrological year (2010/11) compared to the first one, differences in the following years are not uniform any more. The same is valid for the ground cover type classes debris, coarse blocks and soil. This indicates, that for these classes, interannual differences of MAGST are influenced by additional factors other than MAAT.

The SO indicates whether MAGST at a specific site is higher or lower than MAAT. Figure 5.2 presents SO for hydrological years 2010 – 2014. In flat and steep rock, SO is > 0°C for all hydrological years and all loggers with maximum values as high as 9°C. On the other hand, negative SO values of up to -6°C are found in the class of coarse blocks. Because SO is an altitude-corrected index, differences within different types of surface material are based on influencing factors like varying snow conditions or variable surface and subsurface charac-

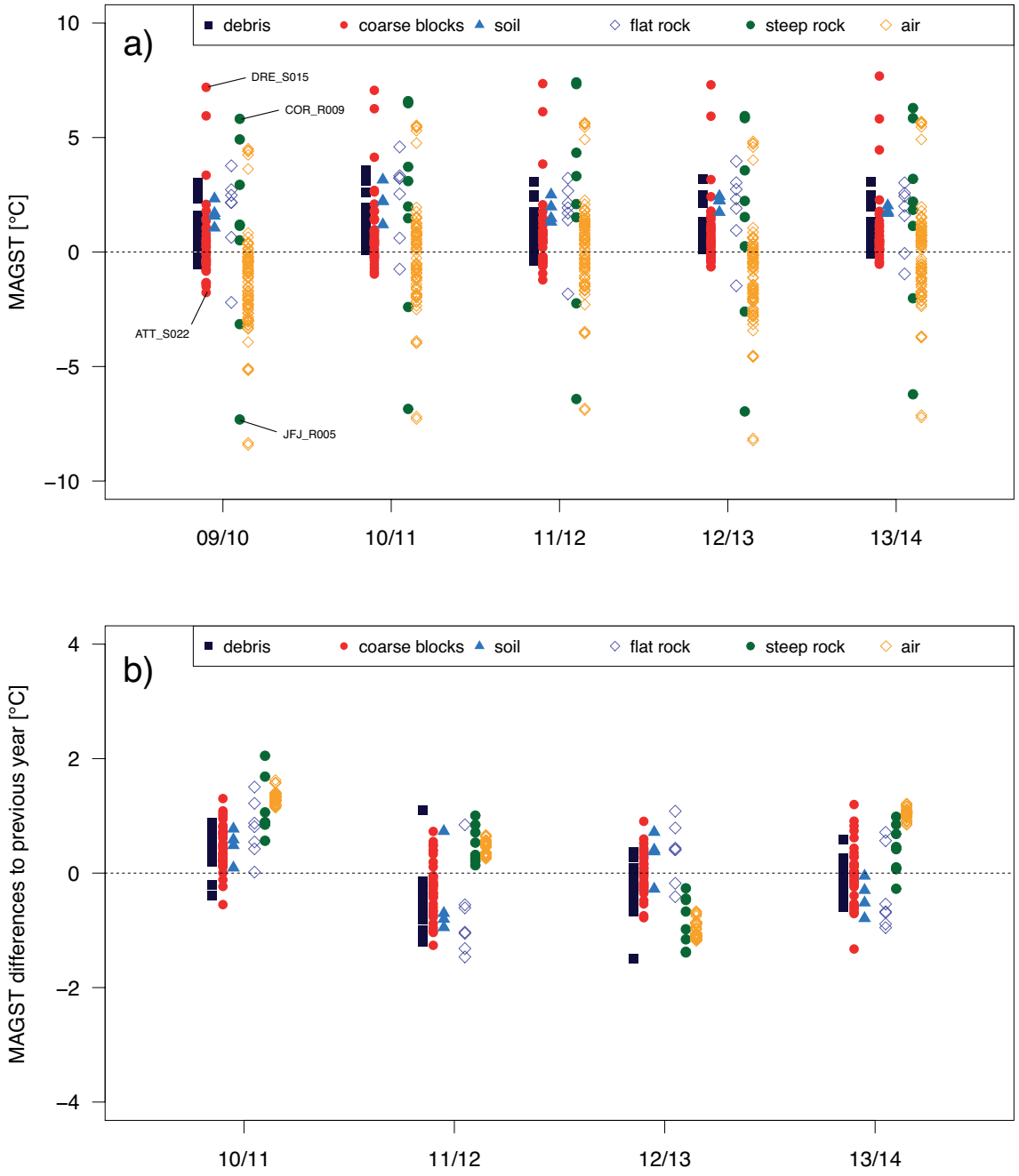

Figure 5.1: a) shows MAGST and MAAT from different measurement sites for hydrological years 2010 - 2014 separated by the type of surface material at the respective sites. The class *flat rock* is defined as bedrock with a slope $< 30°$, whereas *steep rock* is defined as bedrock with a slope $\geq 30°$. For the hydrological year 2010, the names of the measurement devices with maximum and minimum MAGST within the ground cover type classes coarse blocks and steep bedrock are given. **b)** presents differences of MAGST and MAAT of hydrological years relating to previous hydrological years.

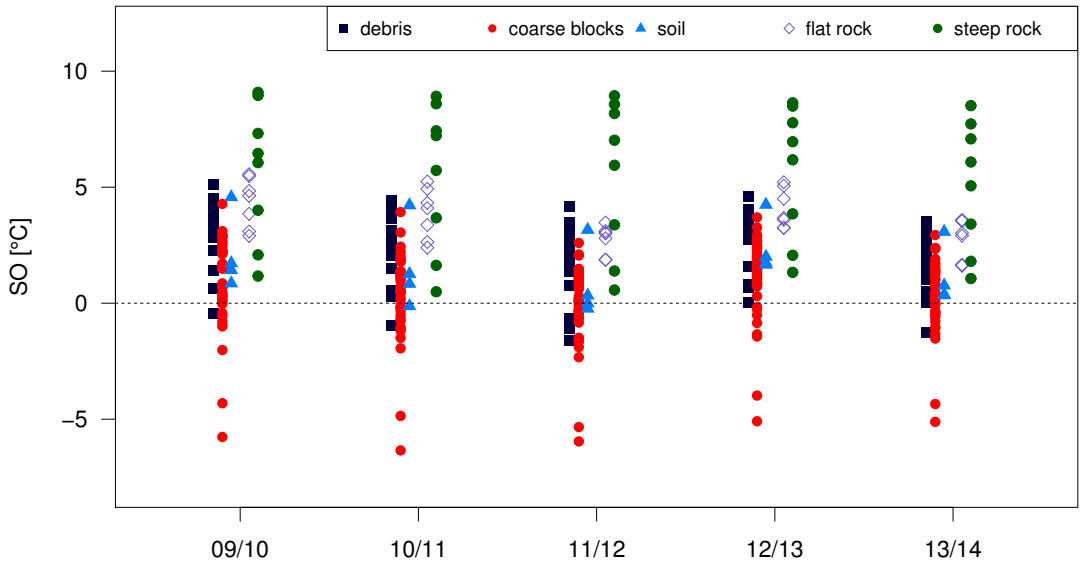

Figure 5.2: SO of hydrological years 2010 – 2014 separated by the type of surface material at the respective sites.

teristics. Differences between different types of surface material can primarily be attributed to large-scale differences in irradiation of short wave radiation, varying snow conditions and surface material specific processes.

Figure 5.3 presents MAGST and SO for hydrological years 2010 – 2014 for each measurement location. For steep and flat rock, SO is always > 0°C, independently of MAGST. In contrast to debris, coarse blocks, soil and flat rock, SO in steep rock is characterized by small interannual variations. Whereas few measurements of SO in the classes debris and soil are < 0°C in single years, the class coarse blocks is the only surface material, where SO of certain measurement devices is < 0°C during all hydrological years. However, the majority of SO in the class coarse blocks is > 0°C for all years. Whereas north exposed measurement devices in steep rock walls show differences between MAGST and MAAT of up to 5°C smaller than measurement devices situated in different expositions, this pattern is not apparent in the other types of surface material. Thus, variability in aspect primarily has an apparent influence in steep rock walls. Note that the high MAGST measured at the loggers `DRE_S013`, `DRE_S014` and `DRE_S015` is most likely the consequence of aspiration of external warm air in connection with the *chimney effect* (Section 2.2). The low SO of the measurement devices `DRE_S010` and `DRE_S012` is based on pronounced cooling processes in the blocky material.

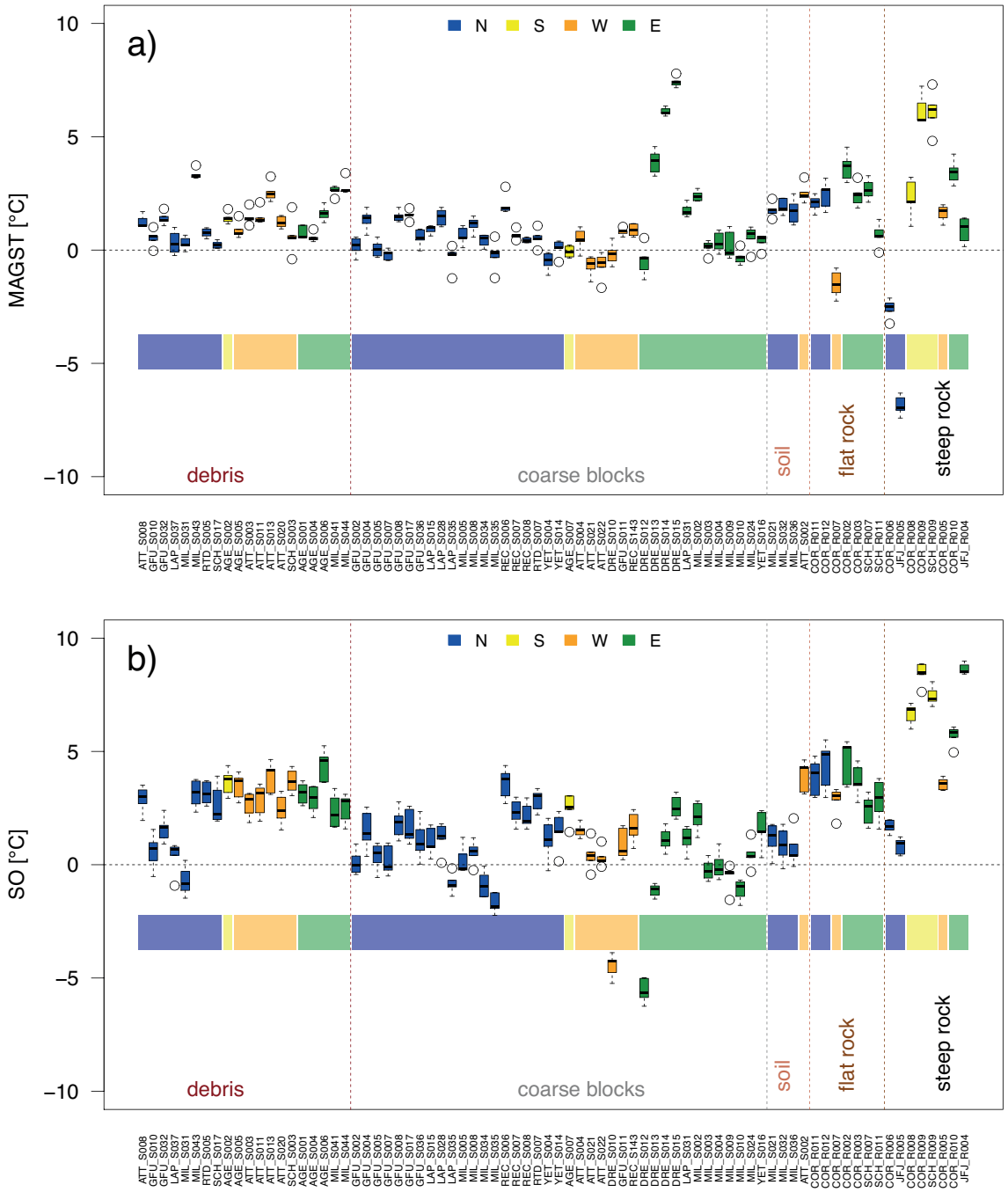

Figure 5.3: Variability of MAGST (**a**)) and SO (**b**)) of different sites for hydrological years 2010 - 2014, differentiated by exposition.

5.2 Trend

Regarding a mean of 15 hydrological years, the mean inter-annual variability is ± 0.47°C (± 0.1°C) for MAGST and ± 0.43°C (± 0.01°C) for MAAT. Trends are calculated for 36 GST time series, all measured in the Western MAR and Western NAR (Figure 5.5). Model assumption of independent residuals is verified checking the serial auto-correlation of the residuals. Five time series show a significant auto-correlation at lag 3 (Figure 5.4). Nevertheless, because no annual cycle is super-imposing the pattern of the ACF, the residuals are considered as temporal independent.

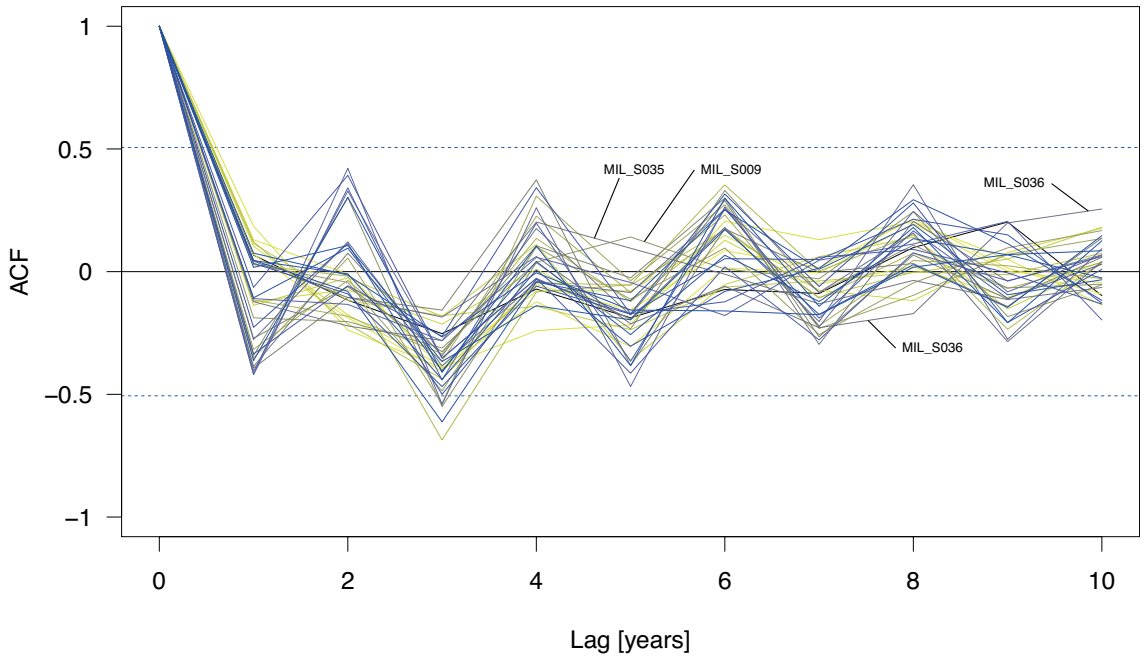

Figure 5.4: Correlogram of the residuals of each time series analyzed in trend estimation with linear regression. The x-axis gives the lag (k) and the y-axis gives the auto-correlation (r_k) at each lag. Correlation is dimensionless, so there is no unit for the y-axis. If r_k falls outside the horizontal blue dotted lines, there is evidence for auto-correlation.

Observed trends in MAGST for the time period of hydrological years 2000 – 2014 lie between -0.56°C and 1.16°C (Table 5.1). However, no trend differs significantly from zero. By means of the Monte Carlo method, 1000 time series are randomly computed for each measured time series in order to study the uncertainty of the observed trends. For two time series, single MCM trends are significant. However, since the majority of the modeled trends and all of the observed trends are statistically not significant, MCM results are not further interpreted. In the context of this thesis, trend analysis is applied to detect climate signals in GST data. For this reason, trends of MAAT are additionally analyzed at every GST measurement location in order to get a reference value of the climate signal. Observed trends in MAAT lie between -2.24°C and 2.48°C and are all highly insignificant. P-values of MAAT trends lie within the

range of 0.8 - 1. Therefore, the null hypothesis of no trend is confirmed for all MAAT time series (Table 5.1).

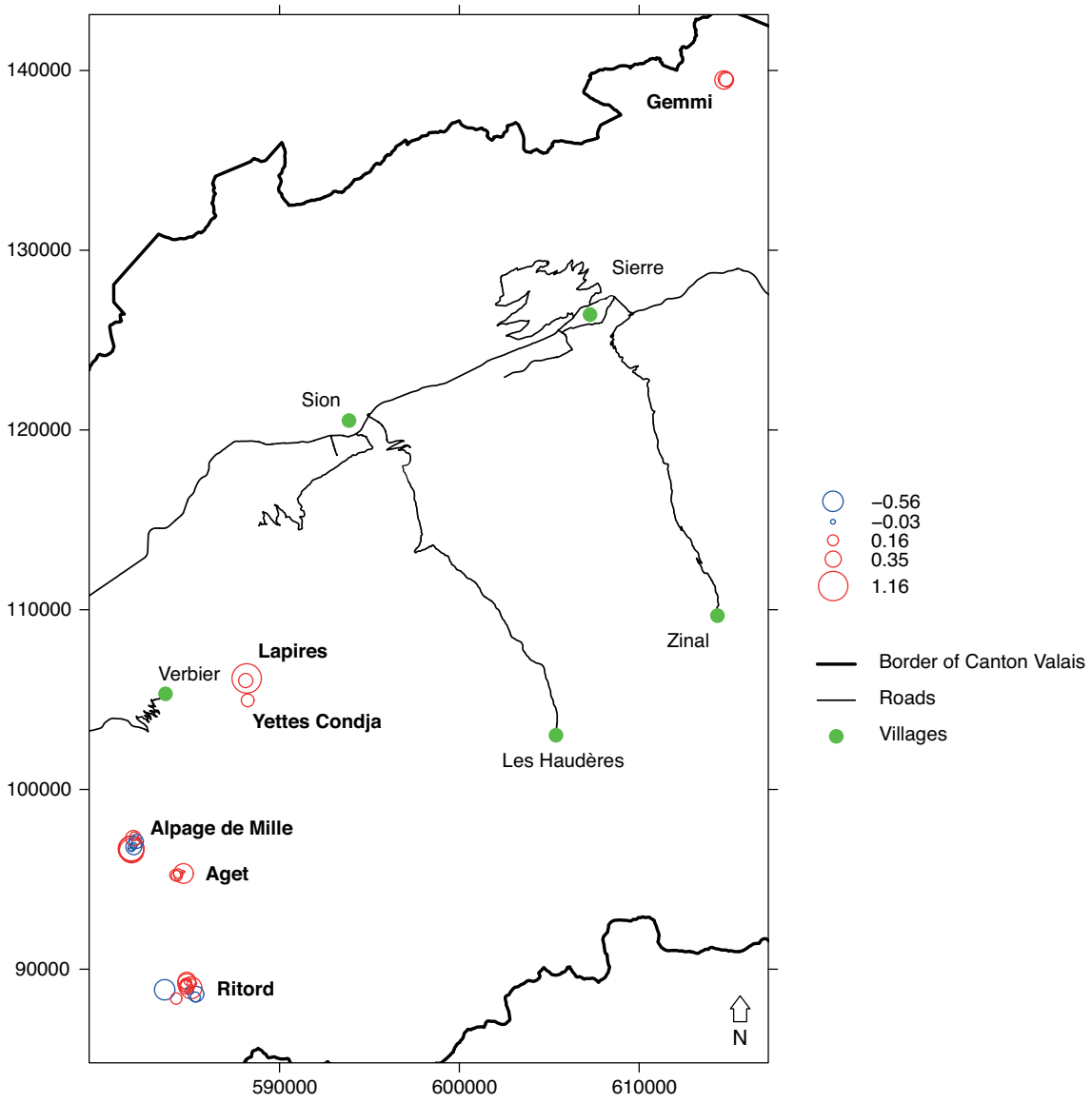

Figure 5.5: Trends of MAGST [°C] for time series with lengths of 15 years at different sites. The location of the circle refers to the location of the measurement device, the size of the circle is proportional to the value of the trend. Blue circles indicate negative, red circles indicate positive trends. Trends of filled circles are significant, trends of empty circles are not.

Table 5.1: Trends of MAGST, Monte Carlo method and MAAT for GST time series with lengths of 15 hydrological years (2000 – 2014).

Name of logger	P-value of MAGST trend	Trend of MAGST [°C]	Number of signif. trends in MCM	μ of MCM trends [°C]	σ of MCM trends [°C]	P-value of MAAT trend	Trend of MAAT [°C]
AGE_S001	0.98	0.01	0	0.02	0.1	0.98	0.99
AGE_S002	0.3	0.52	0	0.52	0.1	1	0.98
AGE_S005	0.77	0.16	0	0.16	0.1	0.99	0.89
AGE_S006	0.7	0.16	0	0.16	0.1	1	1.54
AGE_S007	0.84	0.12	0	0.11	0.1	0.99	-0.16
GFU_S003	0.6	0.29	0	0.29	0.09	0.84	0.32
GFU_S010	0.46	0.45	0	0.45	0.1	0.8	0.45
GFU_S017	0.56	0.27	0	0.27	0.1	0.82	1.37
LAP_S015	0.6	0.27	0	0.27	0.1	0.94	0.58
LAP_S028	0.06	1.16	316	1.16	0.1	0.95	-0.77
MIL_S002	0.97	-0.02	0	-0.02	0.1	0.96	2.48
MIL_S003	0.17	0.88	0	0.88	0.1	0.96	-0.54
MIL_S004	0.15	0.83	3	0.83	0.1	0.95	-0.62
MIL_S005	0.91	-0.07	0	-0.07	0.1	0.97	0.45
MIL_S009	0.91	-0.06	0	-0.06	0.1	0.99	0.01
MIL_S021	0.44	-0.33	0	-0.32	0.1	0.96	1.97
MIL_S024	0.24	0.8	0	0.81	0.1	0.97	0.05
MIL_S032	0.78	-0.1	0	-0.1	0.1	0.96	2.25
MIL_S034	0.56	0.33	0	0.34	0.1	0.96	-0.06
MIL_S035	0.85	0.1	0	0.1	0.11	0.95	-0.25
MIL_S036	0.55	-0.27	0	-0.27	0.1	0.98	2.33
RTD_S001	0.4	-0.56	0	-0.56	0.1	0.93	-1.03
RTD_S002	0.81	0.17	0	0.17	0.1	0.98	-2.24
RTD_S006	0.21	0.64	0	0.64	0.1	0.98	-1.87
RTD_S008	0.86	-0.08	0	-0.08	0.1	0.99	2.27
RTD_S009	0.92	0.06	0	0.06	0.1	0.98	-1.16
RTD_S010	0.85	-0.13	0	-0.13	0.1	1	-0.57
RTD_S011	0.55	-0.33	0	-0.34	0.1	0.98	-1.7
RTD_S014	0.79	0.11	0	0.11	0.1	0.97	1.94
RTD_S015	0.67	0.27	0	0.27	0.1	0.99	-0.95
RTD_S016	0.69	0.18	0	0.18	0.1	0.98	1.36
RTD_S017	0.72	0.15	0	0.15	0.1	0.98	0.19
RTD_S018	0.32	0.45	0	0.45	0.1	0.97	0.82
RTD_S019	0.91	0.07	0	0.07	0.1	0.99	0.66
RTD_S020	0.55	0.41	0	0.41	0.1	0.99	-1.04
YET_S004	0.77	0.22	0	0.22	0.1	0.94	-1.17

Because GST is influenced by various factors depending on the time of the year, trends are most likely present when looking at different seasons. Looking at winter (December, January, February), spring (March, April, May) and summer (June, July, August), no significant trends were found in the GST and AT data. Again, p-values are clearly above 0.05 and MCM only shows single significant trends (Table 7.4, Table 7.5, Table 7.6). However, positive significant trends are found in the GST time series for autumn (September, October, November). Again, the independence of the residuals is verified, checking the serial autocorrelation of the residuals (Figure 5.6). Aside from three time series, which show a significant auto-correlation at lag 7, no serial auto-correlation is observed. Because no distinct pattern is visible in the correlogram, the residuals are considered temporally independent.

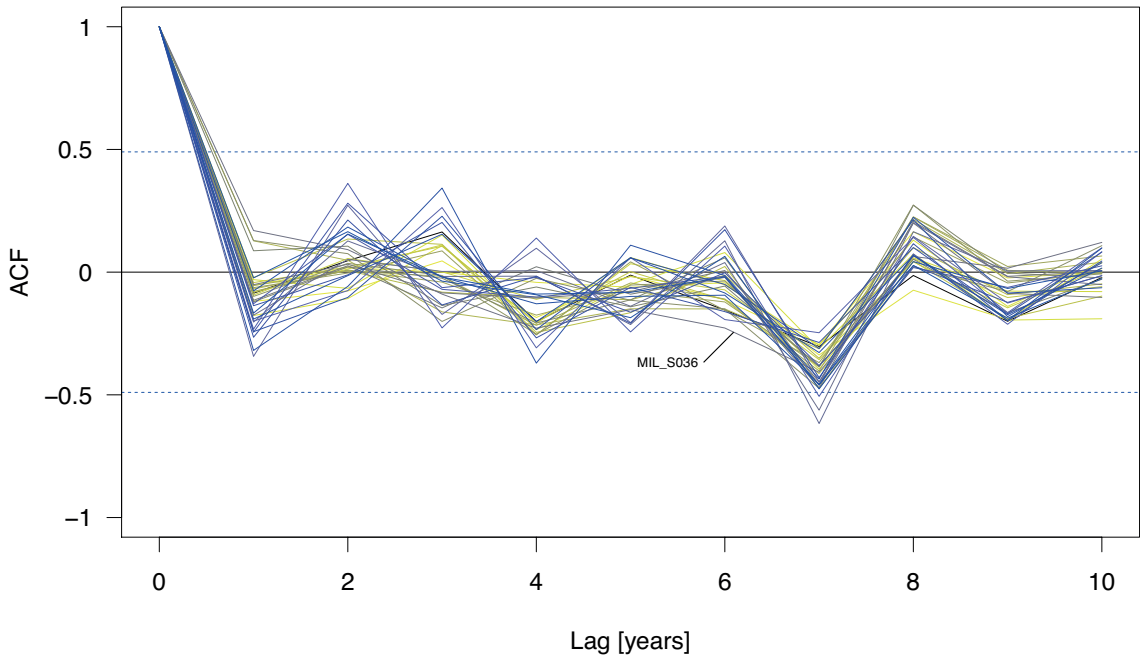

Figure 5.6: Correlogram of residuals from autumn of GST time series analyzed in trend estimation.

30 GST time series exhibit a significant trend in autumn. Looking at all trends, the observed trend values are all positive and lie between 0.53°C and 3.76°C. On the other hand, the significant trends are located within a range of 1.3 - 3.76°C (Table 5.2). For those significant trends, where all 1000 runs of MCM show a significant trend, the mean standard deviation is ± 0.11°C. In case of MAAT, no trends are present in the AT time series for autumn. P-values lie between 0.2 and 0.25 and the null hypothesis of no trend is confirmed. This indicates that the observed trends in GST for autumn are not the result of a climate signal in AT.

Table 5.2: Trends of GST, Monte Carlo method and AT for GST time series with lengths of 15 years (2000 – 2014) for autumn.

Name of logger	P-value of GST trend	Trend of GST [°C]	Number of signif. trends in MCM	μ of MCM trends [°C]	σ of MCM trends [°C]	P-value of AT trend	Trend of AT [°C]
AGE_S001	0.02	1.51	985	1.53	0.11	0.22	-0.04
AGE_S002	0	2.52	1000	2.59	0.11	0.22	-0.19
AGE_S005	0.01	2.02	1000	2.11	0.12	0.22	0.09
AGE_S006	0	1.94	1000	1.98	0.11	0.22	0.63
AGE_S007	0.05	1.44	489	1.49	0.12	0.22	-0.14
GFU_S003	0.06	2.14	225	2.12	0.12	0.21	-0.19
GFU_S010	0.01	2.81	1000	2.95	0.12	0.21	-0.22
GFU_S017	0.01	2.32	1000	2.46	0.12	0.2	-0.48
LAP_S015	0.01	2.61	1000	2.74	0.12	0.23	-0.78
LAP_S028	0	3.43	1000	3.43	0.1	0.24	-2.68
MIL_S002	0.03	1.98	923	2.16	0.12	0.24	0.88
MIL_S003	0	3.22	1000	3.37	0.12	0.25	-1.92
MIL_S004	0	3.25	1000	3.37	0.11	0.24	-1.39
MIL_S005	0.01	2.48	1000	2.55	0.12	0.25	-0.18
MIL_S009	0.01	2.79	1000	2.84	0.11	0.24	-0.32
MIL_S021	0.04	1.72	422	1.86	0.11	0.25	0.64
MIL_S024	0	3.76	1000	3.9	0.11	0.24	-2.61
MIL_S032	0.03	1.72	898	1.89	0.12	0.25	1.29
MIL_S034	0.01	2.76	1000	2.8	0.11	0.24	-1.45
MIL_S035	0.01	2.7	1000	2.78	0.11	0.25	-1.44
MIL_S036	0.02	1.57	986	1.73	0.11	0.25	1.46
RTD_S001	0.04	1.77	941	1.74	0.11	0.25	-1.09
RTD_S002	0.07	1.39	398	1.36	0.1	0.22	-1.24
RTD_S006	0.01	1.83	1000	1.81	0.11	0.23	-1.42
RTD_S008	0.01	1.93	1000	1.95	0.12	0.22	0.89
RTD_S009	0.1	1.14	134	1.07	0.11	0.23	-0.85
RTD_S010	0.08	1.3	84	1.27	0.11	0.21	-0.84
RTD_S011	0.32	0.53	0	0.45	0.11	0.22	-0.94
RTD_S014	0.01	1.87	1000	1.89	0.12	0.22	0.68
RTD_S015	0.04	1.59	998	1.54	0.11	0.22	-1.47
RTD_S016	0	2.48	1000	2.55	0.12	0.23	0.33
RTD_S017	0.01	2.16	1000	2.15	0.11	0.23	-0.16
RTD_S018	0	2.23	1000	2.31	0.12	0.22	-0.1
RTD_S019	0.11	0.93	27	0.91	0.11	0.22	-0.15
RTD_S020	0.03	1.3	942	1.29	0.11	0.23	-0.6
YET_S004	0.04	1.83	601	1.87	0.11	0.23	-1.7

5.3 Spatial variability

In order to quantify the mean spatial variability of GST, the MAE is computed for selected sites. The mean of the MAE for hydrological years 2007 – 2011 is 0.88°C (± 0.06°C) for `Ritord`, 0.5°C (± 0.07°C) for `Gemmi` and 0.96°C (± 0.15°C) for `Alpage de Mille`. This results in an overall mean MAE of 0.78°C (± 0.1°C) for the selected sites. Thus, the mean spatial variability is in the range of ± 0.78°C within an elevational band of 230 m. The mean range of maximum differences for the corresponding sites is 3.2°C (± 0.36°C).

The spatial variability of MAGST in Alpine terrain is analyzed by means of a multiple linear regression model. With an adjusted R-squared of 0.6, the model explains 60% of the variability in MAGST. The p-value is $< 2.22 \times 10^{-16}$ and the model therefore highly significant. Table 5.3 presents the model coefficients of the continuous explanatory variables. All variables differ significantly from zero. Note that the explanatory variable slope is centered at its mean. Since the model contains interaction terms of sin(aspect) and cos(aspect) with slope, a centering of slope produces more meaningful values of the coefficients sin(aspect) and cos(aspect). If slope is centered at its mean, sin(aspect) and cos(aspect) show the average effect at the mean of the slope. However, to analyze the influence of aspect in connection with slope, the variables sin(Aspect), cos(Aspect), Slope, sin(Aspect):Slope and cos(Aspect):Slope cannot be considered individually. Because these explanatory variables refer to the same effect and differ all significantly from zero, only the sum of the single influences shows the overall effect.

Table 5.3: Coefficients and p-values of the explanatory variables of the multiple linear regression model.

	Coefficients	p-value
(Intercept)	12.7257	
SurfType		0.000
Elevation	-0.0045	0.000
sin(Aspect)	0.1056	0.007
cos(Aspect)	-1.2353	0.000
Slope	0.0214	0.000
MASI	2.7551	0.000
Region		0.000
HYear		0.000
sin(Aspect):Slope	0.0119	0.000
cos(Aspect):Slope	-0.0385	0.000

MAGST decreases with a lapse rate of -4.5°C km^{-1}. The effect of exposition to the sun on MAGST is strongly influenced by slope angle. On gentle slopes with slope angles of 10°, differences between east and west are 0.45°C and 3.24°C between north and south. On steeper slopes, differences between varying aspects cause much larger differences in MAGST.

Between east and west, MAGST on east facing slopes with a slope angle of 50° is 1.4°C higher than on west facing slopes. On the other hand, MAGST on north facing slopes with a slope angle of 50° is 6.32°C lower than on south facing slopes. Maximum thermal insulation of the snow cover increases MAGST by 2.76°C compared to sites with absent snow cover.

Table 5.4: Coefficients of the categorical explanatory variables of the multiple linear regression model.

Explanatory variables	Factors	Coefficients	Signif. codes
SurfType	Soil	0.01	
	Debris	-0.20	***
	Coarse blocks	-0.82	***
	Bedrock	1.00	***
Region	Eastern MAR	0.40	***
	Western MAR	-0.22	***
	Western NAR	-0.17	***
HYear	2005	-0.37	***
	2006	-0.80	***
	2007	0.31	***
	2008	-0.20	**
	2009	0.34	***
	2010	-0.14	*
	2011	0.56	***
	2012	0.21	**
	2013	0.03	
	2014	0.06	

0 '***' 0.001 '**' 0.01 '*' 0.05 '.' 0.1 ' ' 1

Table 5.4 shows the model coefficients of the categorical variables. All categorical explanatory variables differ significantly from zero (Table 5.3), whereat single dummy variables (Soil, 2013, 2014) are not significant. The type of surface material has a large influence on the thermal regime at the ground surface. MAGST in coarse blocks is about 0.6°C lower than in debris and around 1.8°C lower than in bedrock. Furthermore, MAGST in bedrock is about 1.2°C higher than in debris. Because soil as a dummy variable of surface material has a value close to zero, it is not significant. Nonetheless, it shows that MAGST in soil is higher than in coarse blocks and debris. MAGST differs in different regions significantly. In the eastern MAR, MAGST is 0.57°C higher than in the western NAR and 0.62°C higher than in the western MAR. In the western MAR, MAGST is 0.05°C lower than in the western NAR. Because data from a time period of 10 hydrological years (2005 – 2014) is used to analyze the spatial variability of MAGST, hydrological year as an explanatory variable is introduced. Between consecutive hydrological years, differences range between 0.35 and 1.11°C, which can be attributed to inter-annual variations of MAAT. Since the dummy variables 2013 and 2014 have values close to zero, they are not significant.

Model assumptions are not violated. Figure 7.5 shows the independence of the residuals, Figure 7.6 proves the normal distribution of the residuals and Figure 7.7 displays the constant variance of the residuals. Temporal independence of the residuals is studied checking the serial auto-correlation of the residuals. Given the time period between hydrological years 2005 – 2014, only measurement devices with data for every year are considered in studying the temporal independence. It is assumed, that the result is valid for the data of all measurement devices. Although one time series shows a significant auto-correlation at lag 2, the residuals can be regarded as temporal independent (Figure 5.7).

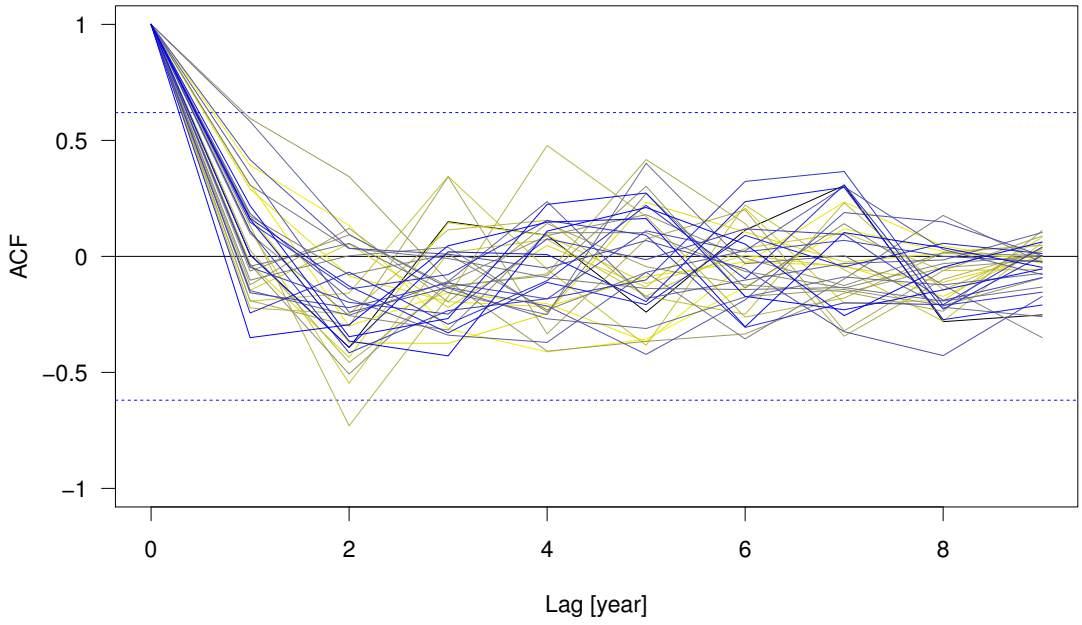

Figure 5.7: Correlogram of the residuals of each time series with data for hydrological years 2005 – 2014, in order to estimate the temporal independence of the data used in the regression model. The x-axis gives the lag (k) and the y-axis gives the auto-correlation (r_k) at each lag. Correlation is dimensionless, so there is no unit for the y-axis. If r_k falls outside the horizontal blue dotted lines, there is evidence for auto-correlation.

In geostatistics, the spatial correlation is modeled by the semivariogram. Therefore, the spatial auto-correlation of the residuals is analyzed estimating the semivariogram. For the residuals of the multiple linear regression model, the semivariance is independent of distance at any distance (Figure 5.8). Hence, the residuals are spatially not auto-correlated, i.e. they are spatially independent.
Due to the lack of an independent data set, the validation of the model behavior is performed by means of a 10-fold cross-validation. In doing so, the data is first randomly partitioned in 10 subsets of equal size. Afterwards, one of the subsets is excluded as validation data. Then, the model is set up with the remaining 9 subsets. Subsequently, for each point in the

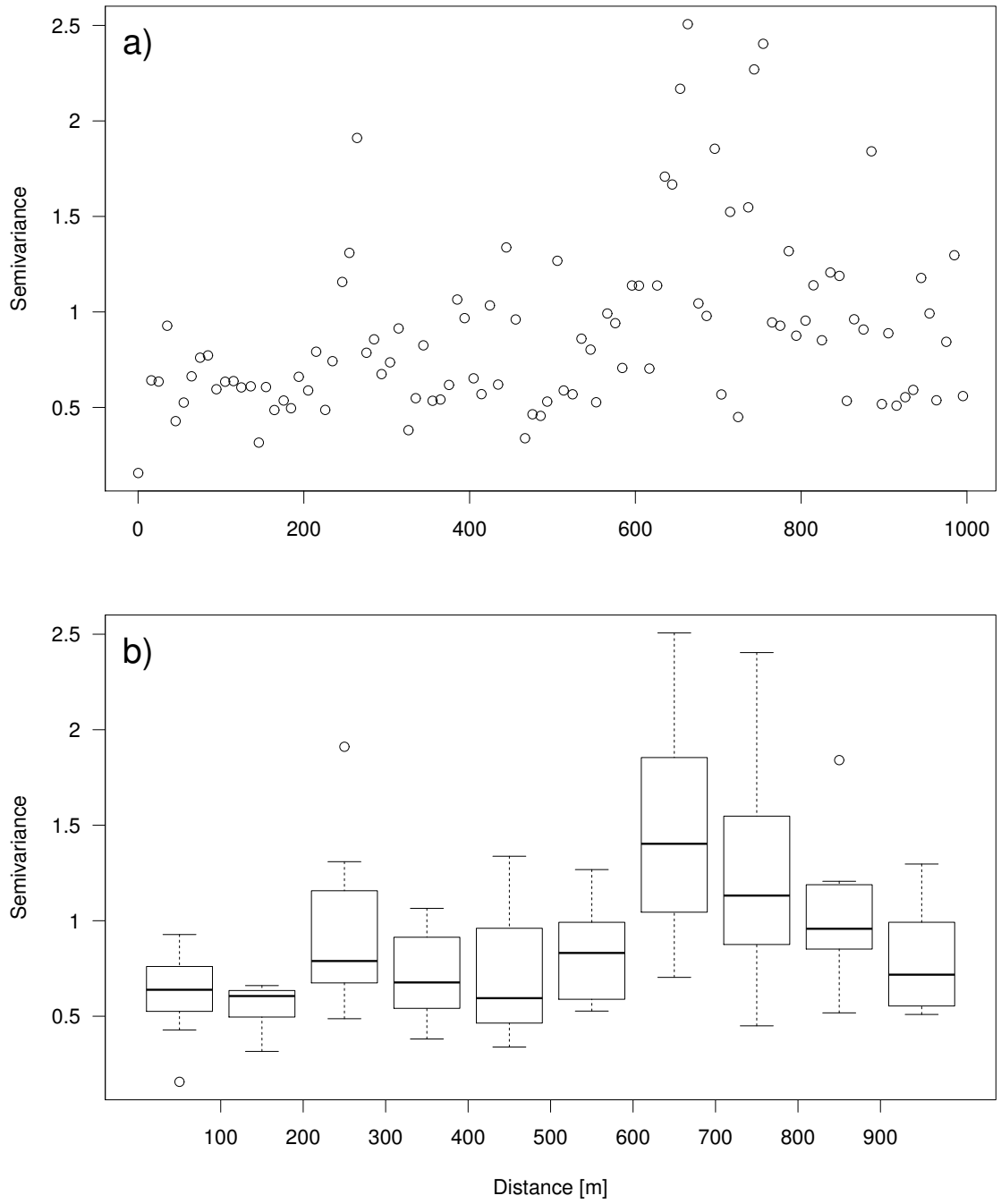

Figure 5.8: Semivariograms of the residuals from the multiple linear regression model. The semivariogram plots semivariance as a function of distance. Any point in the semivariogram refers to a pair of points in the data set. **a)** shows the semivariogram with grouped data points for a distance interval of 10 m, whereas **b)** presents boxplots of the grouped data points for each 100 m interval between 0 and 1000 m. If no increase in semivariance with distance is present, the data can be considered as spatially independent.

validation data, the residuals are estimated. This procedure is repeated as long as all of the 10 subsets once served as validation data. The root mean square error of residuals from the 10-fold cross-validation is 0.94°C whereas the root mean square error is 0.92°C using the complete data set as training data. To estimate the uncertainty of the model coefficients, 95% confidence intervals are calculated. The 95% confidence level expresses that 95% of the (hypothetically) observed confidence intervals will hold the true value of the parameter. Accordingly, the computed confidence intervals do not necessarily include the true values of the parameters. Table 5.5 presents the 95% confidence intervals of the multiple linear regression model. With the exception of MASI, confidence intervals are rather small. This indicates that the estimations of the model coefficients are reliable.

Table 5.5: 95% confidence intervals of the model coefficients from the multiple linear regression model.

Coefficient	2.5 %	97.5 %
(Intercept)	12.0337	13.4177
debris	-0.2969	-0.0943
bedrock	0.8465	1.1557
coarse blocks	-0.9138	-0.7250
soil	-0.1750	0.2027
Elevation	-0.0048	-0.0043
sin(Aspect)	0.0292	0.1820
cos(Aspect)	-1.3356	-1.1351
Slope	0.0170	0.0258
MASI	2.2977	3.2125
Eastern MAR	0.2654	0.5333
Western MAR	-0.3086	-0.1403
Western NAR	-0.2742	-0.0757
2005	-0.5440	-0.2006
2006	-0.9558	-0.6388
2007	0.1583	0.4572
2008	-0.3518	-0.0587
2009	0.1994	0.4875
2010	-0.2815	0.0038
2011	0.4342	0.6920
2012	0.0734	0.3463
2013	-0.1157	0.1784
2014	-0.0953	0.2115
sin(Aspect):Slope	0.0069	0.0168
cos(Aspect):Slope	-0.0430	-0.0340

5.4 Temporal variability

5.4.1 Ground surface temperatures

To analyze the influence of distance, type of surface material, snow cover and topographic variables on the similarity of GST time series, correlations for each pair of GST time series are calculated. Because the correlated time series have been normalized in the preprocessing of the data, systematic differences in absolute GST values exert no influence on the correlation coefficients. See Section 4.5.2 for more explanations regarding the normalization of the data. Additionally, see Figure 7.12, Figure 7.13, Figure 7.14, Figure 7.15 and Figure 7.16 for examples of GST time series with different correlation coefficients.

Figure 5.9 presents the relationship of distance and Spearman's rank correlation coefficient between GST time series for all pairs of GST time series. With a correlation coefficient of -0.35, the correlation is slightly negative. Hence, the correlation between GST time series is decreasing with increasing distance. However, differences are distinct between different

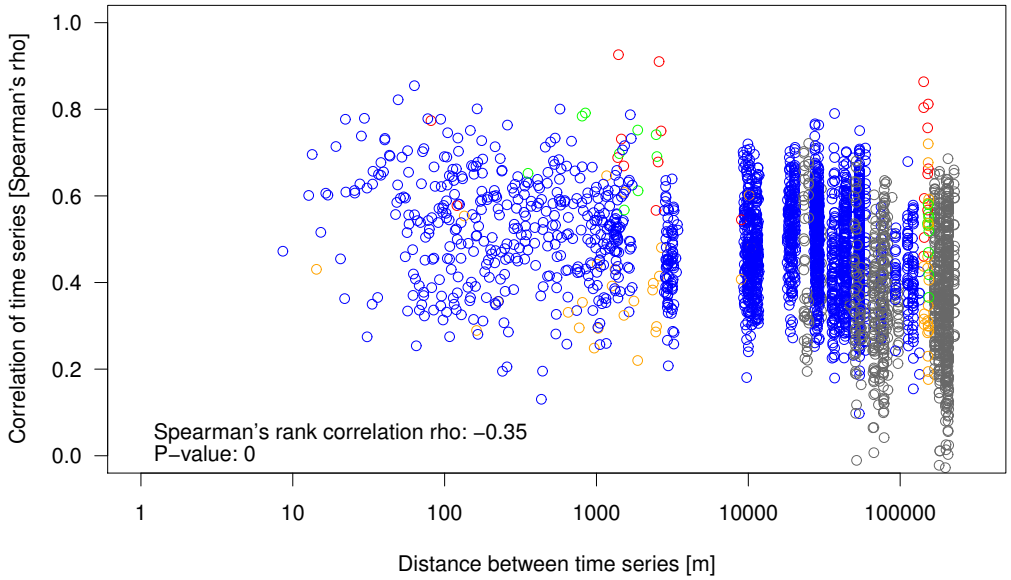

Figure 5.9: Correlation of distance and Spearman's rank correlation coefficient between all possible pairs of GST time series. The colors of the circles refer to the combination of the types of surface material within each pair: red = steep bedrock / steep bedrock, green = flat bedrock / flat bedrock, orange = steep bedrock / flat bedrock, blue = loose material / loose material, gray = steep or flat bedrock / loose material. *Flat bedrock* is defined as bedrock with a slope $< 30°$, whereas *steep bedrock* is defined as bedrock with a slope $\geq 30°$. *Loose material* is the supergroup of soil, debris and coarse blocks.

types of surface material and variations in slope angle. The highest correlation coefficients are found between GST time series measured in bedrock. Figure 7.10 indicates that correlations are higher if both time series are measured in steep or flat bedrock. Correlations of time series between steep and flat bedrock are lower and correlation coefficients of pairs with steep bedrock for both time series are not decreasing with increasing distance. On the other hand, correlation coefficients between time series with flat bedrock as type of surface material decrease with increasing distance. The variation of correlation coefficients at distances around 100 km is large and dominated by pairs of GST time series with mixed type of surface material. Note that mixed type in this context refers to the difference between bedrock and *loose material* (coarse blocks, debris, soil). Differentiation within those groups is not considered. By trend, correlation coefficients between time series with mixed type of surface material are higher if bedrock is flat (Figure 5.10). For pairs of time series with coarse blocks, debris or soil as type of surface material (blue circles in Figure 5.9), variations in correlation coefficients cannot be explained by the possible combinations of the surface material (Figure 7.11).

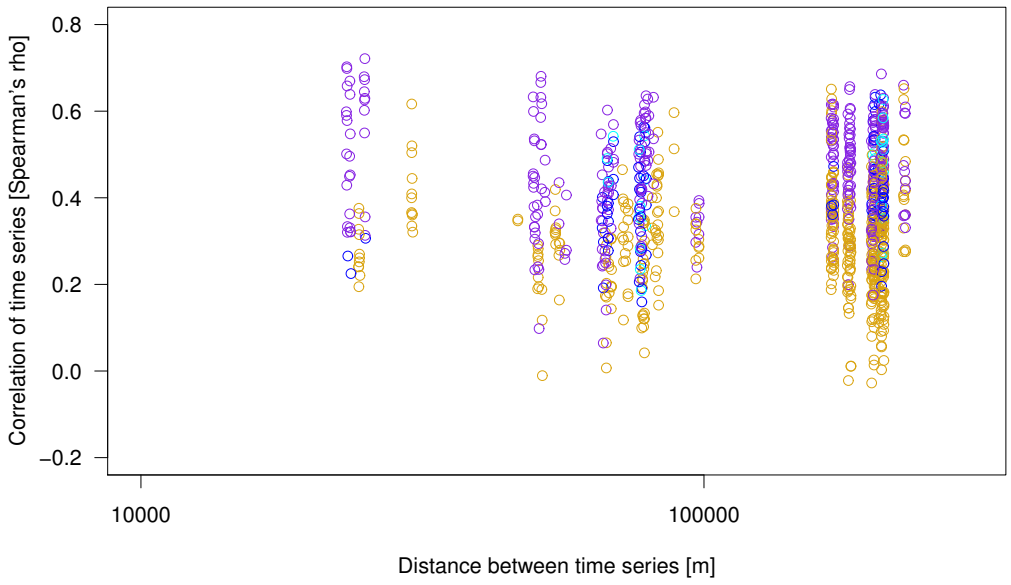

Figure 5.10: Correlation of distance and Spearman's rank correlation coefficient between all possible pairs of GST time series with mixed type of surface material. Mixed type in this context refers to the difference between bedrock and loose material. Differentiation within those groups is not considered. The colors of the circles refer to the combination of the types of surface material within each pair: violet = flat bedrock / coarse blocks, blue = flat bedrock / debris, cyan = flat bedrock / soil, gold = steep bedrock / coarse blocks or debris or soil. *Flat bedrock* is defined as bedrock with a slope $< 30°$, whereas *steep bedrock* is defined as bedrock with a slope $\geq 30°$.

Table 5.6: 20 highest correlation coefficients between GST time series with corresponding meta data. The colors indicate different groups: red = type of surface material is steep bedrock for both measurement devices, blue = type of surface material is coarse blocks or debris and distances are < 1700 m, green = type of surface material is flat bedrock for both measurement devices, brown = type of surface material is coarse blocks and distances are between 27 km and 37 km. Yellow indicates differences of > 90° in the orientation to the sun between the measurement devices.

Correlation coefficient	GST device[1]	GST device[2]	Distance [m]	SurfType[1]	SurfType[2]	Slope[1] [°]	Slope[2] [°]	Aspect[1] [°]	Aspect[2] [°]
0.926	COR_R005	COR_R006	1395.5	bedrock	bedrock	43.9	56.5	273.3	316.7
0.910	COR_R008	COR_R009	2583.0	bedrock	bedrock	32.4	41.9	137.2	153.2
0.864	COR_R006	JFJ_R005	142796.8	bedrock	bedrock	56.5	61.4	316.7	356.5
0.855	GFU_S004	GFU_S031	63.2	coarse blocks	coarse blocks	17.1	25.7	6.2	9.0
0.822	ATT_S005	ATT_S021	49.4	debris	coarse blocks	26.2	27.4	286.3	286.2
0.812	COR_R009	SCH_R009	153027.7	bedrock	bedrock	41.9	32.5	153.2	179.0
0.804	COR_R005	JFJ_R005	142912.0	bedrock	bedrock	43.9	61.4	273.3	356.5
0.801	GFU_S004	GFU_S036	163.7	coarse blocks	coarse blocks	17.1	18.9	6.2	336.5
0.801	MIL_S008	MIL_S035	574.9	coarse blocks	coarse blocks	24.0	22.5	43.5	33.1
0.791	COR_R002	COR_R012	845.4	bedrock	bedrock	4.4	14.6	49.6	44.8
0.790	DRE_S013	MIL_S009	36973.5	coarse blocks	coarse blocks	36.6	33.4	78.0	55.7
0.787	ATT_S022	LAP_S031	1669.5	coarse blocks	coarse blocks	26.4	17.0	287.1	47.3
0.784	COR_R011	COR_R012	804.5	bedrock	bedrock	15.2	14.6	351.9	44.8
0.779	ATT_S004	ATT_S005	29.6	coarse blocks	debris	20.2	26.2	273.7	286.3
0.778	GFU_S002	GFU_S011	77.5	coarse blocks	coarse blocks	20.3	27.4	334.9	313.0
0.777	GFU_S011	GFU_S017	94.2	coarse blocks	coarse blocks	27.4	23.3	313.0	27.8
0.777	LAP_S042	LAP_S043	22.2	debris	coarse blocks	21.6	23.3	30.6	30.6
0.774	COR_R009	COR_R010	81.3	bedrock	bedrock	41.9	50.2	153.2	100.7
0.766	GFU_S011	REC_S002	27489.7	coarse blocks	coarse blocks	27.4	22.9	313.0	301.8
0.764	MIL_S004	REC_S002	29094.7	coarse blocks	coarse blocks	13.1	22.9	46.7	301.8

Table 5.7: 20 most distant GST time series with correlation coefficients > 0.7 and corresponding meta data. The colors indicate different groups: red = type of surface material is steep bedrock for both measurement devices, blue = type of surface material is coarse blocks or debris, brown = type of surface material is flat bedrock for one measurement device and steep bedrock for the other one. Yellow indicates differences of > 90° in the orientation to the sun between the measurement devices.

Correlation coefficient	GST device[1]	GST device[2]	Distance [m]	SurfType[1]	SurfType[2]	Slope[1] [°]	Slope[2] [°]	Aspect[1] [°]	Aspect[2] [°]
0.864	COR_R006	JFJ_R005	142796.8	bedrock	bedrock	56.5	61.4	316.7	356.5
0.812	COR_R009	SCH_R009	153027.7	bedrock	bedrock	41.9	32.5	153.2	179.0
0.804	COR_R005	JFJ_R005	142912.0	bedrock	bedrock	43.9	61.4	273.3	356.5
0.790	DRE_S013	MIL_S009	36973.5	coarse blocks	coarse blocks	36.6	33.4	78.0	55.7
0.766	GFU_S011	REC_S002	27489.7	coarse blocks	coarse blocks	27.4	22.9	313.0	301.8
0.764	MIL_S004	REC_S002	29094.7	coarse blocks	coarse blocks	13.1	22.9	46.7	301.8
0.763	GFU_S004	REC_S002	27488.0	coarse blocks	coarse blocks	17.1	22.9	6.2	301.8
0.757	COR_R008	SCH_R009	151698.5	bedrock	bedrock	32.4	32.5	137.2	179.0
0.751	GFU_S002	MIL_S004	54101.8	coarse blocks	coarse blocks	20.3	13.1	334.9	46.7
0.720	COR_R005	SCH_R010	152989.7	bedrock	bedrock	43.9	23.8	273.3	147.0
0.716	GFU_S002	REC_S002	27567.1	coarse blocks	coarse blocks	20.3	22.9	334.9	301.8
0.711	MIL_S004	REC_S143	29092.1	coarse blocks	coarse blocks	13.1	10.9	46.7	252.5
0.711	DRE_S013	MIL_S035	36597.4	coarse blocks	coarse blocks	36.6	22.5	78.0	33.1
0.710	DRE_S013	GFU_S036	59075.5	coarse blocks	coarse blocks	36.6	18.9	78.0	336.5
0.710	GFU_S017	REC_S002	27507.3	coarse blocks	coarse blocks	23.3	22.9	27.8	301.8
0.708	GFU_S004	MIL_S004	54045.0	coarse blocks	coarse blocks	17.1	13.1	6.2	46.7
0.705	GFU_S011	MIL_S004	54029.2	coarse blocks	coarse blocks	27.4	13.1	313.0	46.7
0.704	GFU_S002	MIL_S009	53926.5	coarse blocks	coarse blocks	20.3	33.4	334.9	55.7
0.702	ATT_S022	GFU_S002	44206.9	coarse blocks	coarse blocks	26.4	20.3	287.1	334.9
0.700	ATT_S005	GFU_S011	44159.1	debris	coarse blocks	26.2	27.4	286.3	313.0

Table 5.6 shows the 20 highest correlation coefficients between GST time series. Correlation coefficients range between 0.764 and 0.926. Four different settings can be differentiated, all leading to high correlation coefficients: 1) First of all, GST time series measured in steep bedrock show the highest correlation coefficients, independently of distances between them (the GST time series with the third highest correlation coefficient are located 140 km apart). Hence, the location plays a minor role in terms of correlations if the GST time series are measured in steep bedrock. 2) Secondly, GST time series located in close proximity which are characterized by coarse blocks or debris as their type of surface material show high correlations. 3) Thirdly, GST time series measured in flat bedrock are correlating very well. 4) And fourthly, GST time series characterized by the surface material coarse blocks and distances between each other in the range of 27 – 37 km indicate high correlations. Note that within those groups, differences in aspect are less than 90° in most cases.

Table 5.7 presents the 20 most distant GST time series with a correlation coefficient > 0.7. As before, GST time series measured in steep bedrock are characterized by high correlation coefficients, even over distances of > 140 km. In addition, a correlation coefficient of 0.72 is found between two time series characterized by steep and flat bedrock. On the other hand, correlations > 0.7 between GST time series of the surface material coarse blocks and debris are found within a radius of 60 km. Differences in slope angle and aspect are small in most of these cases. For distances > 70 km within the class coarse blocks, correlation coefficients are smaller. They range between 0.5 and 0.6, whereas aspect is similar with only a few exceptions (Table 7.12).

In contrast to the high correlation coefficients, the lowest correlation coefficients are generally found between GST time series, characterized by different types of surface material (Table 5.8). The biggest differences of GST time series are observed between pairs of type steep bedrock with soil, debris or coarse blocks. Additionally, distances range between 50 and 210 km and differences in aspect are $> 90°$ except in one example. However, note that low correlation coefficients are not strictly linked to different types of surface material and long distances. For example, a low correlation coefficient of 0.097 is present within the same type of surface material and a distance of 54 km.

In the context of GST, a low correlation coefficient between two time series of the same type of surface material does not necessarily imply a big difference in MAGST. Table 7.11 shows the comparison of correlation coefficients with the related mean difference of MAGST for hydrological years 2011 – 2014 by means of three examples. The biggest difference in MAGST is present between the GST time series with the highest correlation coefficient, whereupon the mean difference of MAGST for the lowest correlation coefficient is < 0.4°C.

Table 5.8: 20 lowest correlation coefficients between GST time series with corresponding meta data. The colors indicate different groups: blue = type of surface material is coarse blocks for both measurement devices, red = type of surface material is steep bedrock for one logger and soil, debris or coarse blocks for the other one, green = type of surface material is flat bedrock for one measurement device and coarse blocks for the other one. Yellow indicates differences of $> 90°$ in the orientation to the sun between the measurement devices.

Correlation coefficient	GST device[1]	GST device[2]	Distance [m]	SurfType[1]	SurfType[2]	Slope[1] [°]	Slope[2] [°]	Aspect[1] [°]	Aspect[2] [°]
0.097	GFU_S005	MIL_S010	53798.2	coarse blocks	coarse blocks	20.3	20.5	8.6	49.0
0.093	COR_R009	MIL_S010	208481.9	bedrock	coarse blocks	41.9	20.5	153.2	49.0
0.091	COR_R008	MIL_S021	206547.7	bedrock	soil	32.4	27.3	137.2	17.4
0.080	COR_R008	MIL_S041	206737.5	bedrock	debris	32.4	39.5	137.2	46.0
0.080	COR_R008	LAP_S037	198601.4	bedrock	debris	32.4	21.4	137.2	39.1
0.065	LAP_S037	SCH_R009	67080.0	debris	bedrock	21.4	32.5	39.1	179.0
0.065	LAP_S015	SCH_R010	66239.3	coarse blocks	bedrock	27.2	23.8	6.6	147.0
0.058	COR_R008	MIL_S010	206536.3	bedrock	coarse blocks	32.4	20.5	137.2	49.0
0.056	COR_R008	MIL_S044	206744.0	bedrock	debris	32.4	33.5	137.2	47.3
0.042	MIL_S043	SCH_R009	78384.0	debris	bedrock	42.5	32.5	41.7	179.0
-0.028	COR_R008	LAP_S015	198527.7	bedrock	coarse blocks	32.4	27.2	137.2	6.6
0.025	COR_R009	LAP_S015	200408.0	bedrock	coarse blocks	41.9	27.2	153.2	6.6
0.024	COR_R009	MIL_S043	208687.8	bedrock	debris	41.9	42.5	153.2	41.7
-0.022	COR_R008	REC_S008	180510.9	bedrock	coarse blocks	32.4	20.0	137.2	350.4
0.014	COR_R010	LAP_S015	200476.1	bedrock	coarse blocks	50.2	27.2	100.7	6.6
0.012	COR_R010	REC_S008	182427.4	bedrock	coarse blocks	50.2	20.0	100.7	350.4
0.011	COR_R009	REC_S008	182360.0	bedrock	coarse blocks	41.9	20.0	153.2	350.4
-0.011	REC_S008	SCH_R009	51638.0	coarse blocks	bedrock	20.0	32.5	350.4	179.0
0.007	LAP_S015	SCH_R009	67076.9	coarse blocks	bedrock	27.2	32.5	6.6	179.0
0.003	COR_R008	MIL_S043	206740.8	bedrock	debris	32.4	42.5	137.2	41.7

5.4.2 Ground temperatures

In order to analyze the temporal similarities of GT and GST time series, GT time series are correlated with each GST time series described in Table 7.10. Note that the GT measurement devices are located in depths between 0.5 m and 1.2 m whereas the type of surface material is either debris or coarse blocks (Table 7.13).

Figure 5.11 presents the correlation of the Spearman's rank correlation coefficient and distance of GT and GST time series. Due to a correlation coefficient of -0.07, the temporal similarity of GT and GST time series can be regarded as independent of distance. However, within distances of < 5 km, the correlation coefficients decrease with increasing distance (Figure 7.17). The highest correlation coefficients are found between time series located within distances of < 1 km. However, correlation coefficients of 0.0 are found within the same distance. Differentiating the pairs of GT and GST time series according to their type of surface material, no distinct pattern is evident. In general, correlation coefficients with steep bedrock as type of surface material for the GST time series are less than 0.5 (Figure 5.12). Furthermore, correlation coefficients with flat bedrock as type of surface material for the GST time series are as high as 0.7. Nonetheless, with correlation coefficients of $<$

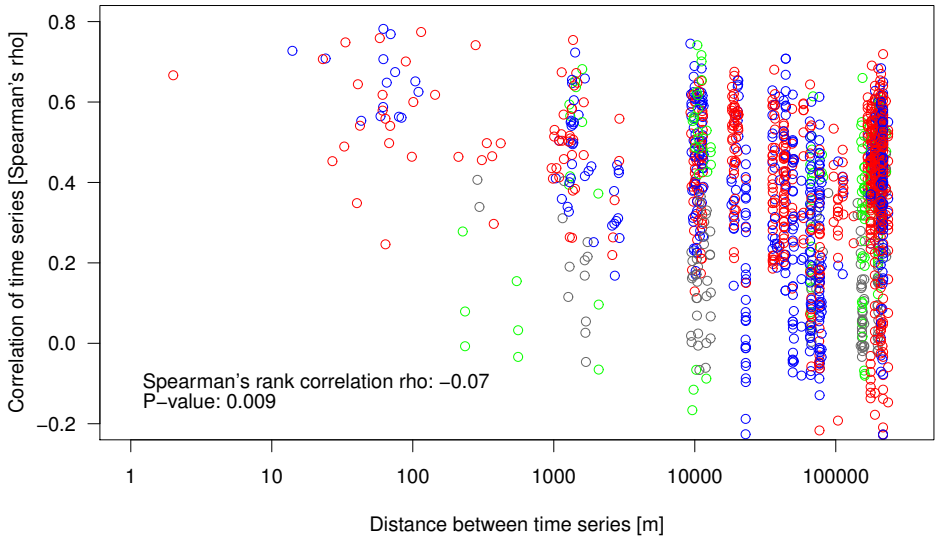

Figure 5.11: Correlation of distance and Spearman's rank correlation coefficient between GT and GST time series. The colors of the circles refer to the combination of the types of surface material within each pair. The first type of surface material refers to the GT time series, the second one to the GST time series: red = debris or coarse blocks for both time series, gray = debris or coarse blocks / steep bedrock, green = debris or coarse blocks / flat bedrock, blue = mixed type of surface material: debris or coarse blocks / soil or debris or coarse blocks. *Flat bedrock* is defined as bedrock with a slope $< 30°$, whereas *steep bedrock* is defined as bedrock with a slope $\geq 30°$.

0.0, the range is large. For the same type of surface materials, both high and low correlation coefficients are found (Figure 7.18). At distances around 200 km, correlation coefficients range between -0.2 and 0.7.

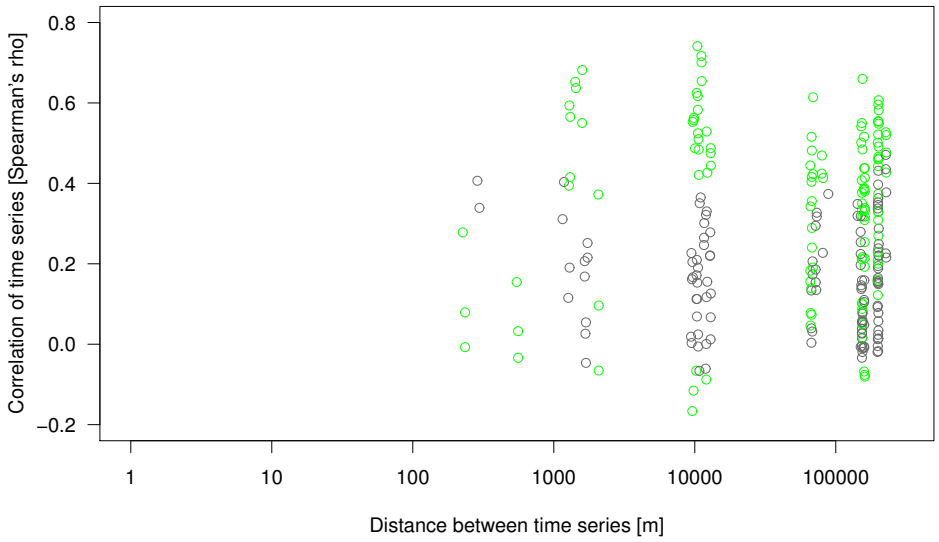

Figure 5.12: Correlation of distance and Spearman's rank correlation coefficient between GT and GST time series with bedrock as type of surface material for the GST time series. The colors of the circles refer to the combination of the types of surface material within each pair. The first type of surface material refers to the GT time series, the second one to the GST time series: green = debris or coarse blocks / flat bedrock, gray = debris or coarse blocks / steep bedrock. *Flat bedrock* is defined as bedrock with a slope $< 30°$, whereas *steep bedrock* is defined as bedrock with a slope $\geq 30°$.

Table 5.9 presents the 20 highest correlation coefficients between GT and GST time series. With a maximum value of 0.782, they are generally lower compared with maximum correlation coefficients of GST time series (Table 5.6). More than half of the highest correlation coefficients are found between time series with distances of 14 – 1500 m. However, distances of < 30 m do not imply higher correlation coefficients than distances of > 30 m. Within those high correlation coefficients resulting from time series in close proximity, the type of surface material is either debris or coarse blocks for both measurement devices or mixed with debris for one logger and coarse blocks for the other one. The sequential arrangement of these pairs indicates that the different combinations of surface material do not lead to different correlation coefficients within distances of < 1500 m. More important are related courses of GT and GST during winter and summer. Figure 7.19 indicates that comparable snow regimes due to similar precipitation patterns and topographic settings are leading to similar temperature courses in winter. On the other hand, similar characteristics in slope and aspect are leading to similar temperature courses over summer.

Table 5.9: 20 highest correlation coefficients between GT and GST time series. The colors indicate different groups: red = type of surface material is coarse blocks or debris for both measurement devices with distances < 1400 m or type of surface material is debris for one logger and coarse blocks for the other one or vice versa with distances < 1500 m, green = type of surface material is coarse blocks for GT measurement device and flat bedrock for GST measurement device, brown = type of surface material is either coarse blocks for both measurement devices or debris for GT logger and coarse blocks for GST logger with a distances between 9 km and 216 km. Yellow indicates differences of > 90° in the orientation to the sun between the measurement devices.

Correlation coefficient	GT device[1]	GST device[2]	Distance [m]	SurfType[1]	SurfType[2]	Slope[1] [°]	Slope[2] [°]	Aspect[1] [°]	Aspect[2] [°]
0.782	LAP_0198	LAP_S037	61.9	coarse blocks	debris	25	21.4	45	39.1
0.774	LAP_1108	LAP_S028	114.6	coarse blocks	coarse blocks	25	22.9	45	12.7
0.769	ATT_0208	ATT_S005	69.6	coarse blocks	debris	30	26.2	270	286.3
0.759	LAP_0198	LAP_S015	58.3	coarse blocks	coarse blocks	25	27.2	45	6.6
0.754	LAP_1108	ATT_S021	1370.1	coarse blocks	coarse blocks	25	27.4	45	286.2
0.748	ATT_0108	ATT_S005	33.3	debris	debris	25	26.2	270	286.3
0.745	ATT_0108	MIL_S035	9302.7	debris	coarse blocks	25	22.5	270	33.1
0.741	LAP_1108	LAP_S031	278.9	coarse blocks	coarse blocks	25	17.0	45	47.3
0.741	MBP_0296	COR_R011	10431.9	debris	bedrock	38	15.2	315	351.9
0.727	ATT_0108	ATT_S022	14.0	debris	coarse blocks	25	26.4	270	287.1
0.723	LAP_1108	ATT_S005	1417.1	coarse blocks	debris	25	26.2	45	286.3
0.719	MUR_0299	MIL_S035	216526.2	coarse blocks	coarse blocks	15	22.5	315	33.1
0.717	MUR_0299	COR_R011	11147.6	coarse blocks	bedrock	15	15.2	315	351.9
0.708	ATT_0108	ATT_S021	24.1	debris	coarse blocks	25	27.4	270	286.2
0.708	ATT_0108	GFU_S002	44198.1	debris	coarse blocks	25	20.3	270	334.9
0.708	ATT_0108	GFU_S011	44126.0	debris	coarse blocks	25	27.4	270	313.0
0.707	ATT_0208	ATT_S021	23.0	coarse blocks	coarse blocks	30	27.4	270	286.2
0.707	ATT_0108	ATT_S004	61.8	debris	coarse blocks	25	20.2	270	273.7
0.701	MUR_0499	COR_R011	11164.5	coarse blocks	bedrock	15	15.2	225	351.9
0.701	ATT_0208	ATT_S004	89.2	coarse blocks	coarse blocks	30	20.2	270	273.7

Table 5.10: 20 most distant GT and GST time series with a correlation coefficient > 0.6. The colors indicate different groups: red = type of surface material is coarse blocks for both measurement devices, blue = measurement devices have different types of surface material: debris or coarse blocks for GT logger and soil or debris or coarse blocks for GST logger, green = type of surface material is debris for GT measurement device and flat bedrock for GST measurement device. Yellow indicates either differences of > 90° in the orientation to the sun between the measurement devices or large irradiation differences due to a slope angle of 0° for the GT measurement device.

Correlation coefficient	GT device[1]	GST device[2]	Distance [m]	SurfType[1]	SurfType[2]	Slope[1] [°]	Slope[2] [°]	Aspect[1] [°]	Aspect[2] [°]
0.719	MUR_0299	MIL_S035	216526.2	coarse blocks	coarse blocks	15	22.5	315	33.1
0.684	MUR_0299	ATT_S005	209542.1	coarse blocks	debris	15	26.2	315	286.3
0.683	COR_0287	ATT_S004	199975.2	coarse blocks	coarse blocks	10	20.2	315	273.7
0.670	MUR_0299	ATT_S021	209495.2	coarse blocks	coarse blocks	15	27.4	315	286.2
0.654	COR_0287	MIL_S035	206741.1	coarse blocks	coarse blocks	10	22.5	315	33.1
0.650	MBP_0296	MIL_S008	216780.7	debris	coarse blocks	38	24.0	315	43.5
0.643	COR_0287	MIL_S008	206945.3	coarse blocks	coarse blocks	10	24.0	315	43.5
0.640	MUR_0499	MIL_S035	216553.5	coarse blocks	coarse blocks	15	22.5	225	33.1
0.637	COR_0200	AGE_S007	204848.8	coarse blocks	coarse blocks	10	12.1	315	143.2
0.622	MUR_0299	MIL_S032	216494.2	coarse blocks	soil	15	35.9	315	352.4
0.617	MUR_0299	LAP_S031	208149.3	coarse blocks	coarse blocks	15	17.0	315	47.3
0.617	MBP_0296	MIL_S035	216562.4	debris	coarse blocks	38	22.5	315	33.1
0.614	MUR_0199	MIL_S035	216571.1	coarse blocks	coarse blocks	15	22.5	315	33.1
0.614	MUR_0299	MIL_S008	216747.5	coarse blocks	coarse blocks	15	24.0	315	43.5
0.614	MBP_0296	LAP_S028	208377.8	debris	coarse blocks	38	22.9	315	12.7
0.612	MUR_0499	LAP_S031	208176.8	coarse blocks	coarse blocks	15	17.0	225	47.3
0.607	ATT_0108	COR_R011	201307.9	debris	bedrock	25	15.2	270	351.9
0.603	SBE_0290	MIL_S035	216154.6	coarse blocks	coarse blocks	0	22.5	NA	33.1
0.602	COR_0287	DRE_S013	226369.7	coarse blocks	coarse blocks	10	36.6	315	78.0
0.600	MUR_0499	ATT_S005	209569.6	coarse blocks	debris	15	26.2	225	286.3

Nonetheless, high correlation coefficients between measurement devices with debris or coarse blocks as type of surface material are not restricted to small distances between the loggers. For distances of 9 – 216 km, correlation coefficients between 0.708 and 0.745 are found. Note that differences in aspect are less than 90° in most cases.

At distances > 200 km, many time series show correlation coefficients > 0.6. This leads to the above mentioned correlation coefficient of -0.07 between Spearman's rank correlation coefficient and distance for GT and GST time series. Table 5.10 shows the 20 most distant GT and GST time series with a correlation coefficient > 0.6. In general, two groups can be differentiated. On one hand, GT and GST time series both measured in coarse blocks correlate well over distances > 200 km. Coarse blocks can prevent the ground from being isolated through a snow cover in winter. This leads to a cooling of the time series, independent of the location (Figure 7.20). On the other hand, time series with mixed types of surface material show correlation coefficients > 0.6. Two settings can be differentiated, leading to these correlation coefficients. Firstly, an unequal course during the summer months due to differences in slope and aspect and a similar course over winter based on comparable snow regimes (Figure 7.21). Secondly, equal courses during the summer months in combination with varying courses over the winter (Figure 7.21). Additionally, a good correlation is found between time series with debris and flat bedrock as type of surface material.

Table 5.11 presents the 20 lowest correlation coefficients between GT and GST time series. For GT time series and GST time series measured in steep bedrock, which are characterized by pronounced diurnal variations, correlation coefficients are around 0.0 (Figure 7.23). Furthermore, a low correlation coefficient is found between time series with debris as type of surface material for GT measurement device respective flat bedrock for GST measurement device (Figure 7.24). Despite the low slope angle, the GST time series shows diurnal variations also in winter time, which causes the low correlation. Low correlation coefficients between time series measured in coarse blocks, debris or soil can be attributed largely to different snow regimes and great differences in slope angle and aspect (Figure 7.25). Aside from a few exceptions, differences in aspect are large.

Table 5.11: 20 lowest correlation coefficients between GT and GST time series. The colors indicate different groups: red = type of surface material is debris or coarse blocks for GT measurement devices and steep bedrock for GST measurement device, green = type of surface material is coarse blocks for both measurement devices and distances are > 190 km, blue = type of surface material is debris or coarse blocks for both measurement devices or debris for GT logger and soil or coarse blocks for GST measurement devices, brown = type of surface material is debris for GT measurement devices and flat bedrock for GST logger. Yellow indicates either differences of > 90° in the orientation to the sun between the measurement devices or large irradiation differences due to a slope angle of 0° for the GT measurement device. *Flat bedrock* is defined as bedrock with a slope < 30°, whereas *steep bedrock* is defined as bedrock with a slope ≥ 30°.

Correlation coefficient	GT device[1]	GST device[2]	Distance [m]	SurfType[1]	SurfType[2]	Slope[1] [°]	Slope[2] [°]	Aspect[1] [°]	Aspect[2] [°]
-0.011	SCH_5200	MIL_S032	76494.0	debris	soil	30	35.9	45	352.4
-0.010	SCH_5000	COR_R010	154694.3	debris	bedrock	30	50.2	45	100.7
0.010	SBE_0190	LAP_S035	207771.4	coarse blocks	coarse blocks	0	21.6	NA	21.3
0.009	SCH_5000	GFU_S002	22928.4	debris	coarse blocks	30	20.3	45	334.9
-0.009	SBE_0190	SCH_R009	159004.7	coarse blocks	bedrock	0	32.5	NA	179.0
0.008	SBE_0190	REC_S007	189943.5	coarse blocks	coarse blocks	0	13.5	NA	17.3
-0.007	SCH_5200	SCH_R011	234.8	debris	bedrock	30	17.8	45	99.7
-0.007	SCH_5000	GFU_S003	22950.1	debris	coarse blocks	30	21.3	45	347.9
-0.007	SBE_0190	AGE_S007	214370.3	coarse blocks	coarse blocks	0	12.1	NA	143.2
-0.006	SBE_0190	JFJ_R005	150147.7	coarse blocks	bedrock	0	61.4	NA	356.5
-0.006	MUR_0299	SCH_R009	159024.5	coarse blocks	bedrock	15	32.5	315	179.0
-0.006	SCH_5200	JFJ_R005	10557.2	debris	bedrock	30	61.4	45	356.5
0.005	SCH_5000	AGE_S002	76286.9	debris	debris	30	8.3	45	187.3
0.005	SBE_0190	YET_S004	208240.9	coarse blocks	coarse blocks	0	11.4	NA	339.5
-0.005	LAP_0198	COR_R008	198576.6	coarse blocks	bedrock	25	32.4	45	137.2
-0.004	SCH_5200	COR_R006	153341.2	debris	bedrock	30	56.5	45	316.7
-0.004	SCH_5200	ATT_S022	67097.3	debris	coarse blocks	30	26.4	45	287.1
0.004	LAP_1208	SCH_R009	67163.2	coarse blocks	bedrock	25	32.5	45	179.0
0.003	SBE_0190	COR_R009	9489.1	coarse blocks	bedrock	0	41.9	NA	153.2
0.001	SBE_0190	COR_R008	12059.9	coarse blocks	bedrock	0	32.4	NA	137.2

6 Discussion

6.1 General explanatory notes

Previous studies of the spatial and temporal variability of MAGST reported substantial variations on the small-scale. In southern Norway, Isaksen et al. (2011) measured a variability of ± 1.5 – 2.0°C within distances of 30 – 50 m and more than 3°C within distances of 100 m. A variability of up to 6°C was documented within areas of 0.5 km^2 for sites in Svalbard and southern Norway (Gisnås et al., 2014). Pogliotti et al. (2015) found that the mean range of spatial variability (2.5 ± 0.1°C) can far exceed the mean range of observed inter-annual variability (1.6 ± 0.1°C) in the southern side of the European Alps. In Switzerland, Gubler et al. (2011) measured differences in MAGST of up to 6°C within an elevational band of 300 m in gentle mountain slopes and variations of up to 2.5°C at distances of less than 14 m in homogeneous terrain.

Spatial and temporal variability of MAGST observed within the context of this thesis are substantial but less pronounced. Exploratory analysis revealed, that the mean inter-annual variability of MAGST for 36 GST loggers is about ± 0.47°C (± 0.1°C) regarding a mean of 15 hydrological years (Section 5.2). However, absolute inter-annual differences can be up to ± 2°C (Figure 5.1). Within an elevational band of 230 m, the mean spatial variability at the same sites is ± 0.78°C (± 0.1°C) regarding a mean of 5 hydrological years. Thereby, the mean range of maximum differences is 3.2 ± 0.36°C within distances of 10 – 1750 m. At the corresponding sites, bedrock as type of surface material is absent. Additionally, aside from two exceptions, aspect is either east, north or west. Therefore, variations in the environmental settings are not pronounced at most, leading to smaller temperature differences than found by Gubler et al. (2011) in an elevational band of 300 m.

In summary, it can be said that the mean range of spatial variability clearly exceeds the mean range of inter-annual variability. The high variability of MAGST in both space and time is reflected in the absence of serial and spatial auto-correlation in the analyzed data set. In the context of the multiple linear regression model, the semivariogram (Figure 5.8) shows that the residuals are not spatially auto-correlated, indicating a pronounced variability on the small-scale. Additionally, any GST time series exhibits systematic serial auto-correlation. In the following sections, the influence of air temperature, aspect and slope, ground cover type, snow cover and meteorological conditions on GST is discussed. Furthermore, the data set and the measurement set-up are evaluated.

6.2 Data set

The analyzed data set involves certain characteristics, which have to be remembered in the context of the interpretation of the results. First of all, the data consists exclusively of single point measurements and is characterized by a low spatial density on the fine-scale. Therefore, the limited reliability regarding the truthful representation of the surrounding environmental condition needs to be kept in mind. Secondly, the distribution of elevation, aspect, type of surface material and slope of the single GST measurement devices is not balanced. This is why certain loggers had to be excluded in the context of the multiple linear regression model (Section 4.4.1). Generally, logger with 1) a southward orientation 2) slope angles $> 40°$ 3) elevations > 3000 m asl. and 4) soil or bedrock as type of surface material are under represented (Figure 3.2, Figure 3.3, Figure 4.4). Thus, absolute values respecting these categories need to be interpreted with caution. Furthermore, data from steep bedrock influenced by snow cover is non-existent. Nonetheless, the analyzed data set has a high reliability due to its temporal support of several years.

6.3 Air temperature

Regarding a period of 15 hydrological years (2000 – 2014), the mean inter-annual variability of MAAT is ± 0.43°C (± 0.01°C), which is practically the same as the mean inter-annual variability of MAGST (± 0.47°C) for the same time period (Section 5.2). This indicates that on the continental scale, the inter-annual variability of GST is largely influenced by the inter-annual variability of AT. However, MAGST time series are strongly modified by variable snow conditions, resulting in heterogeneous courses compared with MAAT time series (Figure 7.2).

The influence of inter-annual variations of MAAT on MAGST is apparent in the explanatory variable *HYear* of the multiple regression model (Section 5.3). The corresponding coefficients represent the inter-annual variations of MAAT, which have a significant influence on MAGST. When comparing the coefficients of *HYear* with measured AT time series in the corresponding time period (Figure 7.9), this explanation appears plausible. Even though differences are evident, warmer and colder years coincide well. The mean range of HYear between hydrological years 2005 – 2014 is about 1°C (Table 5.4), which corresponds well with the mean inter-annual variability of MAAT of ± 0.43°C.

During the last century, global MAAT has risen by about 0.7°C (Trenberth et al., 2007). However, for hydrological years 2000 – 2014, seasonal and annual MAAT trends at GST measurement locations in the western Alps proved to be insignificant (Table 5.1, Table 5.2). These observations of no or even slightly negative temperature trends in AT time series in certain time periods are observed worldwide (Easterling & Wehner, 2009; Meehl et al., 2011) and known as *hiatus periods*. Due to natural climate variability, periods as long as a decade or two of interrupting the general warming trend are likely to occur (Easterling & Wehner, 2009). The last hiatus period was observed between 2000 – 2009 (Meehl et al., 2011), which

strongly overlaps with the time period used for the trend analysis in this thesis. Therefore, the absence of MAAT trends for the time period of 2000 – 2014 appears plausible, even though Swiss annual surface air temperatures have incraesed by +1.75°C between 1864 and 2012 (Brönnimann et al., 2014). Against this backdrop, the absence of MAGST trends for hydrological years 2000 – 2014 is a result of the limited length of GST time series.

MAGST decreases with an overall lapse rate of -4.5°C km^{-1}. For the Alps, Rolland (2003) reports yearly lapse rates of MAAT ranging from -5.4 to -5.8°C km^{-1}, which indicates a strong coupling of GST gradients to those of the air. The observed MAGST lapse rate lies in the range of MAGST lapse rates found in other studies. In Norway and Iceland, lapse rates within the range of 5 – 7°C km^{-1} are observed (Etzelmüller et al., 2007; Farbrot et al., 2008; Hauck et al., 2004; Heggem et al., 2005). Additionally, MAGST gradients of -5.6°C km^{-1} and -4.0°C km^{-1} are found in Switzerland and Czech Republic (Gubler et al., 2011; Šafanda, 1999). The relatively low lapse rate of -4.5°C km^{-1} can possibly be explained by the characteristic of the analyzed data set: On the one hand, GST measurement locations at elevations > 3000 m asl. are under represented. As a consequence, the altitudinal variation, which underlies the computation of the lapse rate, is biased. On the other hand, the use of a mean value for temperature lapse rate may be problematic since it may not be representative of the environmental conditions in a particular region (Minder et al., 2010). In the Cascade Mountains, Minder et al. (2010) found geographic (windward vs lee side) differences in lapse rates to be substantial. Because the MAGST lapse rate of this study is computed based on data from all over the Alps, an underestimation of actual lapse rates is possible. However, complex terrain geometry and small-scale variability of ground cover types and snow cover influence the coupling between atmosphere and ground surface. Therefore, MAGST lapse rate can be altered markedly.

6.4 Aspect and slope

The thermal regime at the ground surface is strongly influenced by aspect and slope angle. Given a slope angle of 10°, differences between north and south orientated slopes are around 3.2°C (Table 5.3). This contrast is increasing with increasing steepness. For slope angles of 50°, MAGST is about 6.3°C lower in north facing slopes than it is in south facing slopes. These differences in MAGST regarding varying slope angles and aspects clearly indicates the influence of the incoming solar radiation. Due to differences in the angle of incidence, steep south orientated slopes receive more direct solar radiation than south orientated slopes with gentle slope angles, leading to an increase in GST with increasing slope angle. In north orientated slopes, the effect of varying steepness on GST is opposite: Since direct solar radiation is reduced in steep terrain compared with gentle slopes, GST in north orientated slopes is decreasing with increasing slope angles. Because the angle of incidence is a function of seasonality, differences vary during the year. These findings, regarding differences in MAGST measured at locations with varying slope angles and aspects, agree with other studies. Hasler et al. (2011) found differences of 1 – 8°C between sun-exposed and shaded locations for slope angles ranging between 30 and 90°. In Switzerland, ranges of up to 10°C

are reported for MAGST measured in near vertical bedrock (PERMOS, 2013). Moreover, for idealized ridges with slope angles of 60°, modeled differences in MAGST between north and south facing slopes are found to be as high as 8°C (Noetzli et al., 2007). The major influence of incoming solar radiation on MAGST is confirmed in the SO found in steep rock walls. In south and east orientated slopes with slope angles > 30°, MAGST is 5 – 9°C higher than MAAT (Figure 5.3). These differenecs agree with SO of 4.1 – 5°C found in steep and south orientated rock walls in British Columbia (Hasler et al., 2015). Thereby, the high amount of solar irradiation leads to a fast snowmelt and thus warming of the ground. On the other hand, SO of 1– 2°C in steep and north orientated rock walls can be explained by the reduced insolation of direct solar radiation. However, the thermal regime of rock walls can be strongly influenced by snow cover (Haberkorn et al., 2015), leading to lower MAGST due to insulation during months with most intense solar radiation. See Section 6.5 for explanations regarding the influence of the snow cover on MAGST in steep rock walls.

Between east and west orientated slopes, differences in MAGST are 0.45°C for slope angles of 10° and 1.4°C for slope angles of 50°. Since the insolation of direct solar radiation is similar between east and west facing slopes, these differences can be attributed to the formation of convective clouds during afternoons (Gubler et al., 2011). Thereby, the insolation of direct solar radiation is reduced in the afternoon, leading to colder west exposed slopes. However, there is scope for interpretation. In areas characterized by great relief variations and steep topography, the above mentioned differences in MAGST between aspects are an important source of three-dimensional patterns in the subsurface thermal regime (Noetzli & Gruber, 2009). Note that the existing GST measurement devices with slope angles > 40° are strongly biased towards bedrock (Figure 3.3). Therefore, results regarding GST differences in steep terrain mainly refer to bedrock and do not have universal validity.

18 out of the 20 highest correlation coefficients between GST time series result from time series measured in similar topographic settings: Differences regarding the orientation to the sun are < 90° (Table 5.6). On the other hand, 19 out of the 20 lowest correlation coefficients between GST time series result from time series with differences in aspect of > 90° (Table 5.8). The same is valid for correlation coefficients between GST and GT time series: 16 out of the 20 highest correlation coefficients between GST and GT time series result from time series, whose measurement locations are characterized by differences of < 90° regarding the orientation to the sun (Table 5.9). On the contrary, 13 out of the 20 lowest correlation coefficients between GST and GT time series result from time series with differences in aspect of > 90° (Table 5.11). Again, this clearly indicates the influence of the incoming solar radiation on the thermal regime at the ground surface. However, similarities in aspect are largely the consequence of small distances between the measurement locations and thus correspond to the general orientation of the relief (Table 5.6, Table 5.9). In other words, meteorological conditions and precipitation patterns tend to be similar between those measurement locations. Furthermore, the type of surface material is equal in the majority of cases regarding high correlation coefficients. Thus, similar micro-climate conditions are very likely. Finally, high correlation coefficients are found between time series with differences in

aspect > 90°. Therefore it is assumed, that aspect is not the main driving factor regarding the similarity of GST and GT time series. Nonetheless, large (small) differences in aspect likely increase (decrease) the trend of correlation coefficients, although the influence of aspect is overprinted by effects of ground properties and snow variability.

6.5 Ground cover type

In general, MAGST in coarse blocks is about 0.6°C lower than in debris, about 0.8°C lower than in soil and around 1.8°C lower than in bedrock (Table 5.4). Accordingly, MAGST in bedrock is about 1.2°C higher than in debris. The cooling effect of coarse blocky ground cover on the ground thermal regime is in agreement with worldwide observations: Juliussen and Humlum (2008) found a temperature anomaly of 1.3 – 2.0°C in openwork blocky debris in central-eastern Norway. In northern Tien Shan, Gorbunov et al. (2004) observed that MAGST inside blocky materials is 2.5 – 4.0°C cooler than air temperature above the surface. Furthermore, S. A. Harris and Pedersen (1998) measured negative temperature anomalies of 4 – 7°C in coarse blocks in Canada and China. In addition, Hanson and Hoelzle (2004) observed pronounced cooling processes in the bouldery active layer of the rock glacier Murtèl in Switzerland. Thereby, low temperatures most likely result from the displacement of warmer air through cold, denser air trapped in the furrows.

The descriptive analysis in this thesis showed that MAGST in coarse blocks can be up to 6°C cooler than MAAT above the surface (Figure 5.2). The cooling effect of coarse material on subsurface temperatures is usually explained by advective heat transfer through air movement in early winter. Additionally, the insulating effect of the snow cover is likely to be reduced by protruding blocks, increasing the negative thermal anomaly. See Section 2.2 for detailed explanations and additional hypotheses. However, the cooling effect of openwork block fields is not observed in any case. MAGST measured in coarse blocks can be up to 4°C higher than the corresponding MAAT (Figure 5.2). This finding confirms the observations of Hasler et al. (2015), where no clear difference in SO between the surface types coarse debris, fine soil, rock and forest was found. On the one hand, this indicates the influence of the snow cover. As long as the snow cover is thick and persistent, the ground thermal regime is decoupled from the atmosphere, leading to an increase in MAGST. At sites with medium size boulders, above-average precipitation and little influence of wind, this is likely to be expected. On the other hand, uncertainties regarding the classification of the different types of surface material need to be taken into consideration. The differentiation between the classes coarse blocks and debris is done by several individuals. Thereby, any classification scheme is used. This is why the classifications are most likely inconsistent. Additionally, the spatial variability of the substrate at the ground surface need to be kept in mind.

Correlation coefficients of GST time series with coarse blocks, debris or soil as type of surface material range between 0.3 and 0.8 within distances of < 100 m (Figure 7.11). Beside the influence of snow cover, these variations result from pronounced small-scale heterogeneity of the substrate at the ground surface. This explains, among others, the absent spatial auto-

correlation (Figure 5.8). Because cooling processes depend on the coarse size of the material at the ground surface, MAGST in debris is relatively higher due to its smaller grain size (Figure 5.2). In fine grained material like soil, SO is likely in the range of 4 – 6°C due to the insulating effect of the snow cover (Farbrot et al., 2013; Lewkowicz et al., 2012).

MAGST in bedrock is generally higher than in the other types of surface material. Depending on the slope angle, this increase is caused by various processes. Higher temperatures in flat bedrock base on the absence of 1) pronounced cooling processes due to the homogeneous nature of the substrate and 2) the influence of an insulating snow cover. SO in flat bedrock is exclusively positive, ranging between 3 – 5°C (Figure 5.3). In the course of this, note that the inter-annual variability can be up to 2°C, clearly indicating the influence of snow cover. The same is true for soil, debris and coarse blocks. In steep bedrock, higher temperatures are mainly caused by 1) the absence of cooling processes and 2) the high irradiation of direct solar radiation in west, south and east oriented slopes. At the same time, the influence of snow cover is largely reduced, leading to a direct coupling of the ground thermal regime with the atmosphere. Firstly, this is shown in Figure 5.1: Inter-annual changes of MAGST generally follow inter-annual changes of MAAT. Secondly, the inter-annual variability of SO in steep bedrock is < 1°C. Thirdly, 3 of the seven highest correlation coefficients between GST time series result from time series which are characterized by distances of > 140 km between each other, slope angles $> 30°$ and bedrock as type of surface material (Table 5.6). These high correlation coefficients result from 1) little influence of snow cover on MAGST in steep bedrock and 2) minor small scale variation in AT. As a consequence, correlation coefficients are not decreasing with increasing distances (Figure 7.10).

However, snow depths between 1.5 – 2 m are reported for 60 to 75° steep rock walls (Haberkorn et al., 2015). In addition, Hasler et al. (2011) found a decrease of MAGST of up to 3°C in 45 – 70° rock faces. This observation is attributed to the effect of a thin snow cover, reflecting the solar irradiation in summer and thus cooling the thermal regime at the ground surface. This finding is supported by Magnin et al. (2015), who confirmed that thin snow covers in steep rock walls lower the surface temperature if present. Finally, Figure 5.1 reveals opposite differences of MAAT and MAGST to previous years in hydrological year 2014. Thus, thermal regimes in steep bedrock cannot be regarded as independent of snow cover, although the influence is most likely reduced. In the literature, the term *steep bedrock* is generally equated with a reduced influence of snow cover. However, no definition regarding the corresponding slope angle exist. Within the context of this thesis, all GST time series measured in bedrock at slope angles $> 30°$ reveal the lack of an insulating snow cover. Therefore, steep bedrock is defined as bedrock with a slope angle $\geq 30°$. Nonetheless, it needs to be kept in mind, that this value neither is a threshold for the influence of the snow cover nor has universal validity.

In general, correlation coefficients of GST time series are high, if both types of surface material are the same (Table 5.6). However, aside from steep bedrock, variations within a certain type of ground cover are large (Figure 7.11). Additionally, correlation coefficients of

GST time series characterized by different types of surface material can be surprisingly high (Figure 5.10, Figure 7.11). This indicates, that the effect of the type of ground cover on the correlation coefficient is controlled by the influence of the snow cover. This hypothesis is supported by several observations: The most striking differences regarding correlation coefficients of GST time series are caused by differences in slope angle (Table 5.8, Figure 5.10), which indicates the dominant influence of the snow regime on the similarity between GST time series. The same is true for correlation coefficients of GST and GT time series: Consistent differences due to variable types of ground cover are only present if GST time series are measured in steep bedrock (Figure 5.12). Otherwise, differences in the type of surface material do not reveal any pattern (Figure 5.11). Therefore, differences in type of surface material play a minor role, possibly because heat conduction into the ground has a filtering influence on GT.

6.6 Snow cover

Maximum thermal insulation of the snow cover increases MAGST by 2.76°C (Table 5.3). This net warming effect most likely results from the low thermal conductivity, which is a function of snow depth: An increasing snow height increases the thermal resistance of the snow cover (Bernhard et al., 1998). As a consequence, the cooling effects of high surface albedo and energy reduction due to latent heat consumption are secondary in connection with a thick snow cover. According to Luetschg et al. (2008), snow depths > 0.6 m effectively insulate the ground from the atmosphere, given coarse blocks as ground cover material. At the same time, Wüthrich et al. (2010) found that the mean of maximum snow depth at altitudes > 1500 m asl. is likely to be > 0.6 m in Switzerland. Although snow depth is largely influenced by redistribution due to wind and avalanches (Luetschg et al., 2004) and thus strongly depends on local topography, it can be assumed, that snow cover by trend has an insulating (net warming) effect on the ground thermal regime in Alpine terrain. In soil, debris and flat bedrock, SO of up to 5°C are found (Figure 5.2). Consequently, this net warming is attributed to the insulating property of the snow cover. However, this warming effect only applies to gentle slopes without cooling processes in the ground cover material. The above mentioned observations correspond well with other findings: Farbrot et al. (2011) found SO of 4.5°C at sites with a thick and prolonged snow cover.

The decoupling of the ground from the atmosphere by snow cover can lead to opposite courses of MAAT and MAGST: Figure 5.1 shows differences of MAGST and MAAT relating to previous hydrological years. In 2012, MAAT is higher than 2011, whereupon MAGST measured in flat bedrock is lower. This can be attributed to a late snow onset date along with low atmospheric temperatures, which has a cooling effect on the ground thermal regime. In 2013, the reverse effect can be observed: MAAT is lower than 2012, whereas MAGST in flat rock is higher apart from two exceptions. Accordingly, this can be attributed to an early snow onset date, insulating the ground from low AT. Therefore, the date of first winter snow insulation of the snow cover plays, among the depth of the snow cover, a major role regarding the thermal regime at the ground surface.

For autumn, significant seasonal trends are found in the GST time series for hydrological years 2000 – 2014 (Table 5.2). These trends mainly occur due to low temperatures in 1999 and above-average temperatures in 2014 (Figure 7.4). At the same time, corresponding trends in MAAT are insignificant, excluding climate signal as a driving force. Figure 7.2 reveals that in terms of MAGST, the atmospheric signal is strongly overlaid by varying inter-annual snow conditions. This indicates, that within short observation periods ($\leq$ 15 years), trends are appearing coincidentally due to varying snow conditions. Same observations were made in the Upper Engadine. Regarding a time period of 8 years, Schneider et al. (2012) found that instead of atmospheric temperatures, the subsurface thermal regime is rather influenced by height and duration of the snow cover. As a consequence, MAGST trends strongly depend on chosen period of time and season. In summary, the effect of variable snow conditions on MAGST exceed the effect of MAAT on MAGST in short term observation. These results are confirmed by Luetschg et al. (2008): Numerical model simulations indicate that snow depth is the most important factor influencing the ground thermal regime, even more important than climatic factors.

As mentioned above, the spatial and temporal variability of the snow cover is crucial concerning the temporal similarity of GST and GT time series. Independent of other influencing factors, it can lead to similar courses of GST and GT time series: Correlation coefficients of up to 0.7 are found in GST time series with coarse blocks and flat bedrock as type of ground cover (Figure 5.10), which indicates similar influence of snow cover. Additionally, 3 of the 20 highest correlation coefficients between GST and GT time series are located in moderate proximity ($<$ 12 km), where the type of surface material is flat bedrock and debris or coarse blocks (Table 5.9). However, the snow cover is likely the dominant factor of influencing spatial variability in GST. Gisnås et al. (2014) found a variability of MAGST of up to 6°C within areas of 0.5 km^2, which is explained by variation in snow height. In the context of this thesis, correlation coefficients of GST time series with coarse blocks as type of surface material are found in the range of 0.2 – 0.7 at distances between 100 m and 80 km (Figure 7.11). The same is true for GST and GT time series (Figure 7.18). These variations, within a single class of ground cover type, can most likely be attributed to highly variable snow regimes, even within a certain type of ground cover. In all probability, this leads, among the heterogeneity of the substrate at the ground surface, to the absent spatial auto-correlation at short distances (Figure 5.8).

6.7 Meteorological conditions

In Alpine terrain, the thermal regime at the ground surface differs significantly in different regions (Section 5.3). MAGST in the eastern MAR (Upper Engadine) is 0.57°C higher than in the western NAR (Bernese Oberland, north of Valais) and 0.62°C higher than in the western MAR (south of Valais) (Table 5.4). In the western NAR, MAGST is 0.05°C higher than in the western MAR. These differences can be attributed to variable climatic regimes within Alpine terrain. On the one hand, differences in cloudiness are distinctive.

Figure 6.1: Hours of sunshine for the SwissMetNet stations `Piz Corvatsch` (red), `Jungfraujoch` (purple) and `Zermatt` (blue) for hydrological years 2005 – 2014. The horizontal lines represent the corresponding means. Data source: MeteoSwiss.

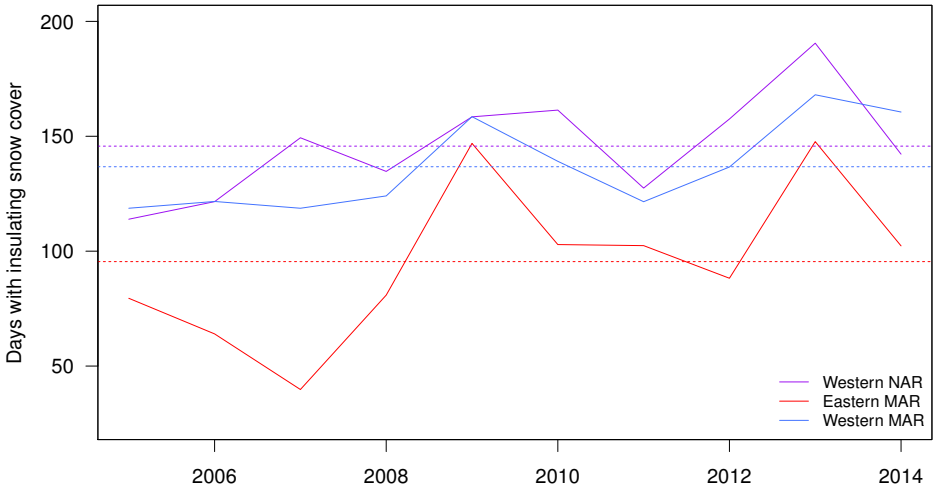

Figure 6.2: Average number of days with insulating snow cover for the regions western NAR, western MAR and eastern MAR for hydrological years 2005 – 2014. An isolating snow cover is defined as $snow_2 > 0.5$, whereat $snow_2$ is an index suggested by Staub and Delaloye (2016), which quantifies the isolating properties of the snow cover based on weekly variations of GST.

Figure 6.1 shows the annual sums of hourly sunshine for three different SwissMetNet stations for hydrological years 2005 – 2014. Thereby, the weather station `Piz Corvatsch` is located in close proximity to the measurement devices. In the eastern MAR, `Jungfraujoch` lies in between the measurement locations of the western NAR and `Zermatt` is representing the western MAR. On average, `Piz Corvatsch` receives 1980 hours of sunshine per year, `Jungfraujoch` 1780 and `Zermatt` 1690 hours. Although the extrapolation of these point measurements on the corresponding regions is afflicted with great uncertainty, they still indicate large differences in insolation between the regions. On the other hand, snow regimes are very diverse. Figure 6.2 presents the average number of days with an insulating snow cover for the three different regions. On average, an insulating snow cover in the eastern MAR is present for 95 days, in the western NAR for 145 days and in the western MAR for 136 days. Even though the inter-annual variability is pronounced, the duration of the insulating snow cover in the eastern MAR is consistently the lowest. Nonetheless, conclusion regarding the influence of the snow cover on MAGST can only be drawn, if the timing of the snow cover is known. A short duration of an insulating snow cover can have a warming effect, if the onset of the snow cover is in early winter and thus preventing the ground thermal regime from cooling. Furthermore, the absence of a snow cover in spring leads to a warming of the ground, because solar irradiation is not reflected and energy is not used for melting.

A study regarding snow onset and disappearance dates within the Swiss Alps reveals a significant trend in snow cover duration for the eastern Alps: By trend, the duration of the snow cover has decreased for about three weeks during the last 60 years, whereas the snow onset date tends to be later in the year compared with the other regions (Buchmann, 2016). Therefore, higher temperatures in the eastern MAR are attributed to a combined effect of solar irradiation and duration of snow cover: longer sunshine duration combined with shorter duration of an insulating snow cover leads to an additional warming of the ground by direct solar radiation. Because the average number of days with an insulating snow cover is similar for western NAR and western MAR, the difference of 0.05°C is attributed to the difference regarding the hours of sunshine. In the light of the continental scale, these findings reveal the influence of climate (e.g. precipitation patterns, cloudiness) on the ground thermal regime. However, further studies are needed to verify this hypothesis.

With a correlation coefficient of -0.35, the similarity of two GST time series is dependent on the distance between them (Figure 5.9). Maximum correlation coefficients of GST time series with soil, debris and coarse blocks as types of surface material start to decrease at distances $>$ 40 km (Figure 7.11). Among others, this can be attributed to the influence of varying precipitation patterns, leading to different snow regimes at sites with similar ground properties. Due to a correlation coefficient of -0.07, the similarity of GT and GST time series is independent of distance. At distances $>$ 40 km, no decrease in maximum correlation coefficients is observed, although differences in precipitation patterns are likely to be expected. Since GT is measured in depths between 0.5 – 1.2 m, their sensitivity regarding changing environmental conditions at the ground surface is reduced due to the influence of subsurface characteristics. According to the heat transfer mechanisms, GT represent the

mean of a thermal regime at the ground surface. Hence, the control of varying precipitation patterns on GT is likely reduced compared with GST.

6.8 Measurement set-up

In Alpine terrain, MAGST is influenced by variable cloudiness and precipitation patterns. In order to accommodate for these regional differences, a spatially balanced measurement set-up is a prerequisite. However, within the Swiss Alps, the distribution of GST measurement sites is in piecemeal fashion (Figure 3.1). The bias towards GST sites located within the western MAR is strong, which is reflected in data: About three-quarter of the data analyzed by means of the multiple regression model and 33 out of 36 GST time series studied in the trend analysis originate from the western MAR (Figure 4.4, Figure 5.5). Furthermore, data measured in the central MAR had to be excluded in the context of the multiple regression model due to the lack of representativeness. Accordingly, the influence of central MAR on corresponding MAGST remains unknown due to the small amount of data. As mentioned in Section 6.2, the uneven distribution of the data regarding elevation, aspect, slope and type of surface material is even more pronounced. Measurement devices representing extreme measurement locations (slope angles $> 40°$, elevations > 3000 m asl.) are very few. Furthermore, east and south orientated measurement locations are strongly under represented. Nonetheless, reliable results regarding the influencing factors of GST are based on a balanced distribution of the measurement locations. In terms of future analyses, extensions and set-up changes of the existing monitoring set-up should be used to fill these gaps where possible.

7 Conclusions and outlook

This thesis analyzes the unique data set of GST time series collected by PERMOS, extended with data from various other permafrost research programs in the Swiss, French and Italian Alps. Thereby, the spatial and temporal variability of GST is studied by means of different statistical methods. Furthermore, the measurement set-up and the available data set are evaluated in terms of future analyses. Below, the research questions of this thesis are set in connection to the results and findings of the preceding chapters. Additionally, future research needs are mentioned.

How is the spatial variability of GST influenced by topographic parameters, type of ground surface material, snow cover and different regions in Alpine terrain?

In general, the spatial variability of GST in Alpine terrain is pronounced and significantly influenced by elevation, slope angle, aspect, type of ground surface material, snow cover and different regions. No spatial auto-correlation is found in the data set. This indicates a high spatial variability of GST due to highly variable snow regimes on small-scale observations as well as a pronounced heterogeneity within 1) a certain type of ground surface material and 2) small-scale topography. On the one hand, the topographic parameters influence the spatial variability of GST based on the interaction of slope and aspect: Differences found in MAGST between north and south orientated slopes are around 3.2°C given a slope angle of 10° and 6.3°C given a slope angle of 50°. Since the incoming solar radiation in south-exposed slopes increases with increasing slope angle but decreases with increasing slope angles in north orientated slopes, differences are marked in steep terrain. Because the insolation of direct solar radiation is similar between east and west facing slopes, differences in MAGST are less pronounced. West facing slopes are 0.4°C lower than east-exposed slopes given a slope angle of 10° and 1.4°C lower given a slope angle of 50°. As another component of the topographic parameters, elevation influences MAGST based on the coupling of air temperature gradients with those of the ground surface. Thereby, MAGST decreases with an average lapse rate of -4.5°C km^{-1} within Alpine terrain.

Differences in the type of ground surface material make a big difference regarding the thermal regime at the ground surface: MAGST in coarse blocks is about 1.8°C lower than in bedrock, about 0.8°C lower than in soil and about 0.6°C lower than in debris. Accordingly, MAGST in debris is about 1.2°C lower than in bedrock and about 0.2°C lower than in soil. These differences can be attributed primarily to various cooling processes in open work blocky material, varying insulating properties of the snow cover and the influence of solar irradiation in steep bedrock. The influence of the snow cover on the spatial variability of

GST is crucial. A thick and persistent snow cover can increase MAGST by up to 2.8°C due to its thermal insulation properties. Thereby, the low thermal conductivity of the snow cover leads to a decoupling of the ground thermal regime from atmospheric conditions, preventing the ground from cooling during the winter months for all surface materials. Finally, it has been shown for the first time, that MAGST on a continental scale differs significantly in different regions. MAGST measured in the eastern MAR is 0.57°C higher than in the western NAR and 0.62°C higher than in the western MAR. According to an exploratory analysis, the observed differences can be attributed to variable climatic regimes, respectively to different meteorological conditions: In the Upper Engadine, longer sunshine duration combined with shorter duration of an insulating snow cover possibly leads to an additional warming of the ground by direct solar radiation.

Although the data set is characterized by a low spatial density on the small-scale, it has a high reliability due to its extensive range and its temporal support of up to 15 years. Thus, the above mentioned results regarding the spatial variability of GST in Alpine terrain can be considered as rules of thumb. Nonetheless, the uneven distribution of measurement locations within the data set (cf. Section 6.2) as well as the missing categories (e.g. steep bedrock influenced by snow cover) must be kept in mind.

What is the temporal variability of GST within the Swiss Alps?

Regarding a time period of 15 hydrological years, the mean inter-annual variability of MAGST (± 0.47°C) is very much like the mean inter-annual variability of MAAT (± 0.43°C). This indicates that the inter-annual variability of GST is primarily controlled by the inter-annual variability of AT. However, absolute inter-annual differences of MAGST can be up to 2°C and the mean range of spatial variability exceeds the mean range of inter-annual variability. This pronounced temporal variability is reflected in the absence of climate signals in the GST time series: Annual trends of MAGST are not significant in the considered time period, whereby the same is true for MAAT. Since time series with a length of 15 hydrological years are quite short in terms of trend analysis and the observation period is largely overlaid by an atmospheric hiatus period, the absent climate signal appears plausible. 30 seasonal GST trends for autumn are significant, whereby no trends are found in the corresponding AT time series. This indicates that the observed trends are independent of AT. This is confirmed by exploratory analysis, showing that these trends appear coincidentally due to below and above average temperatures at the beginning and the end of the analyzed time series. Thus, the effect of variable snow conditions on MAGST exceeds the effect of MAAT on MAGST in short term observations.

To study the temporal similarity of GST and GT time series, Spearman's rank correlation coefficients are calculated. With a correlation coefficient of -0.35, the variability between GST time series increases with increasing distance. Among others, this can be attributed to variable precipitation patterns over large distances. Regarding GST, the highest correlation coefficients are found between time series measured in steep bedrock, whereby distances

range between 1.4 and 140 km. This indicates, that in steep bedrock the influence of the snow cover is most likely reduced. Accordingly, the thermal regime at the ground surface is strongly linked with air temperatures. Generally, the snow cover is an important influencing factor regarding the temporal variability of GST time series. Although the influence of aspect and type of surface material is apparent, their effect on the thermal regime at the ground surface is most likely overlaid by the influence of the snow cover. For distances up to 200 km, the temporal variability between GST and GT time series is independent of distance. Nonetheless, for distances less than 5 km, the variability between GST and GT time series increases with increasing distance. This highlights the question regarding the representativeness of GT measured in boreholes. However, due to the little amount of GST measurement locations in close proximity to boreholes, this question remains unanswered.

How could the measurement set-up of GST monitoring in Alpine terrain be improved in terms of future analyses?

Regarding the measurement set-up and the corresponding data set, the following conclusions can be drawn: Although the distribution of measurement locations on the scale of the Swiss Alps do not follow any higher-level measurement strategy, statistical analysis regarding the spatial and temporal variability of GST are feasible. Thereby, the gap filling algorithm proved to be crucial in respect of meaningful results. Only by its application, the extensive range of the data set could be achieved. For hydrological years 2005 – 2014, 1439 MAGST values from 260 measurement locations at 24 sites are analyzed in the context of the multiple linear regression model. Regarding the estimation of trends, 36 GST time series with lengths of 15 hydrological years (2000 – 2014) are studied based on annually aggregated values. Furthermore, correlations are computed for 81 GST time series with lengths of 4 subsequent hydrological years.

However, the distribution of elevation, aspect, type of surface material and slope is not balanced in the analyzed data set. As a consequence, the informative value regarding the underrepresented categories is limited. In order to improve the explanatory power in the context of future analyses, potential new loggers should be installed at 1) south and east facing slopes, 2) slope angles $> 40°$, 3) elevations > 3000 m asl. and 4) in bedrock or soil. Whenever possible, existing measurement devices in those categories should be continued. In general, measurement devices located at 1) north orientated slopes, 2) coarse blocks and 3) slope angles between 10 and 30° are strongly over represented. The unbalanced measurement setup is further biased by the spatial distribution of the measurement locations. In Alpine terrain, the distribution of measurement locations is in piecemeal fashion with a strong tendency towards western MAR. This imbalance is further enhanced, because most of the longest GST time series are located in the western MAR. In order to achieve a spatially balanced measurement setup, potential new loggers should therefore be installed in regions other than the lower Valais.

The following questions and research needs are raised by the results of this thesis:

- The snow depth is a major factor influencing the ground thermal regime. Thus, the future evolution of snow conditions in the context of climate warming and its influence on the ground thermal regime needs to be further investigated. Possible research topics in this context are the systematic analysis of 1) trends regarding the evolution of snow heights, 2) the effect of a rising snow line on permafrost and 3) the influence of changing snow onset dates, snow durations and snow disappearance dates on permafrost.
- MAGST differs significantly in different regions. However, the corresponding explanation is only verified qualitatively. Therefore, further research is needed to study the variable meteorological conditions in different Alpine regions as well as their influence on the thermal regime at the ground surface. This could be achieved by measuring the essential meteorological parameters (e.g. hours of sunshine, direct solar radiation, precipitation) at selected sites, in order to 1) compare them among each other and 2) set them in relation with the corresponding ground thermal regimes.
- The analyzed data set proved to be of use to study the influencing factor of MAGST on the continental scale. However, it remains unclear, whether these measurements truthfully represent their surrounding ($\leq$ 100 m^2) environmental conditions. As a consequence, small-scale variations need to be quantified regularly.
- In order to assess the representativeness of GT regarding the thermal regime of its nearby environment, additional GST loggers should be installed in close proximity ($\leq$ 100 m) to selected boreholes.

The results of this thesis supported and extended findings of previous studies and highlighted future research needs. It is hoped that they make a contribution for a deeper understanding of the spatial and temporal variability of GST in Alpine terrain.

References

Akaike, H. (1974). A new look at the statistical model identification. *IEEE Transactions on Automatic Control*, *19*(6), 716–723. doi: 10.1109/TAC.1974.1100705

Appenzeller, C., Begert, M., Zenklusen, E., & Scherrer, S. C. (2007). Monitoring climate at Jungfraujoch in the high Swiss Alpine region. *Science of the Total Environment*, *391*, 262–268. doi: 10.1016/j.scitotenv.2007.10.005

Barry, R. G. (2008). Geographical controls of mountain meteorological elements. In *Mountain weather and climate* (3rd ed., pp. 24–124). Cambridge University Press.

Bayazit, M., & Önöz, B. (2007). To prewhiten or not to prewhiten in trend analysis? *Hydrological Sciences Journal*, *52*(4), 611–624. doi: 10.1623/hysj.53.3.669

Begert, M., Schlegel, T., & Kirchhofer, W. (2005). Homogeneous temperature and precipitation series of Switzerland from 1864 to 2000. *International Journal of Climatology*, *25*, 65–80. doi: 10.1002/joc.1118

Bernhard, L., Sutter, F., Haeberli, W., & Keller, F. (1998). Processes of snow/permafrost-interaction at high-mountain site, Murtel/Corvatsch, Eastern Swiss Alps. In *Proceedings of the 7th international conference on permafrost* (pp. 35–41). Yellowknife (Canada).

Blunden, J., & Arndt, D. S. (2015). State of the Climate in 2014. *Bulletin of the American Meteorological Society*, *96*(7), 1–238. doi: 10.1175/2015BAMSStateoftheClimate.1

Boeckli, L., Brenning, A., Gruber, S., & Noetzli, J. (2012). Permafrost distribution in the European Alps: calculation and evaluation of an index map and summary statistics. *The Cryosphere*, *6*(4), 807–820. doi: 10.5194/tc-6-807-2012

Bonnaventure, P. P., & Lamoureux, S. F. (2013). The active layer: A conceptual review of monitoring, modelling techniques and changes in a warming climate. *Progress in Physical Geography*, *37*, 352–376. doi: 10.1177/0309133313478314

Brönnimann, S., Appenzeller, C., Croci-Maspoli, M., Fuhrer, J., Grosjean, M., Hohmann, R., Ingold, K., Knutti, R., Liniger, M. A., Raible, C. C., Röthlisberger, R., Schär, C., Scherrer, S. C., Strassmann, K., & Thalmann, P. (2014). Climate change in Switzerland: A review of physical, institutional, and political aspects. *Wiley Interdisciplinary Reviews: Climate Change*, *5*, 461–481. doi: 10.1002/wcc.280

Buchmann, M. (2016). *Changes of snow onset and disappearance dates during the last 60 years in the Swiss Alps* (Master Thesis). ETH Zurich.

Cowpertwait, P. S., & Metcalfe, A. V. (2009). Forecasting strategies. In *Introductory time series with r* (pp. 45–66). Dordrecht: Springer.

Delaloye, R., & Lambiel, C. (2005). Evidence of winter ascending air circulation throughout talus slopes and rock glaciers situated in the lower belt of alpine discontinuous per-

mafrost (Swiss Alps). *Norsk Geografisk Tidsskrift - Norwegian Journal of Geography*, *59*, 194–203. doi: 10.1080/00291950510020673

Delaloye, R., Reynard, E., Lambiel, C., Marescot, L., & Monnet, R. (2003). Thermal anomaly in a cold scree slope (Creux du Van, Switzerland). In *Proceedings of the 8th international conference of permafrost* (pp. 175–180). Zürich (Switzerland).

Easterling, D. R., & Wehner, M. F. (2009). Is the climate warming or cooling? *Geophysical Research Letters*, *36*. doi: 10.1029/2009GL037810

Ernste, H. (2011). *Angewandte Statistik in Geografie und Umweltwissenschaften*. Zürich: vdf.

Etzelmüller, B., Farbrot, H., Gudmundsson, A., Humlum, O., Tveito, O. E., & Björnsson, H. (2007). The Regional Distribution of Mountain Permafrost in Iceland. *Permafrost and Periglacial Processes*, *18*(December 2006), 185–199. doi: 10.1002/ppp

Etzelmüller, B., & Frauenfelder, R. (2009). Factors Controlling The Distribution of Mountain Permafrost in The Northern Hemisphere and Their Influence on Sediment Transfer. *Arctic, Antarctic, and Alpine Research*, *41*(1), 48–58. doi: 10.1657/1523-0430-41.1.48

Etzelmüller, B., Hoelzle, M., Heggem, F., Solbjørg, E., Isaksen, K., Mittaz, C., Vonder Mühll, D., Ødegård, R. S., Haeberli, W., & Sollid, J. L. (2001). Mapping and modelling the occurrence and distribution of mountain permafrost. *Norsk Geografisk Tidsskrift - Norwegian Journal of Geography*, *55*(4), 186–194. doi: 10.1080/00291950152746513

Farbrot, H., Hipp, T. F., Etzelmüller, B., Isaksen, K., Ødegård, R. S., Schuler, T. V., & Humlum, O. (2011). Air and ground temperature variations observed along elevation and continentality gradients in Southern Norway. *Permafrost and Periglacial Processes*, *22*(4), 343–360. doi: 10.1002/ppp.733

Farbrot, H., Isaksen, K., & Etzelmüller, B. (2008). Present and past distribution of mountain permafrost in Gaissane Mountains, Northern Norway. In *Proceedings of the 9th international conference on permafrost* (pp. 427–432). Fairbanks (Alaska).

Farbrot, H., Isaksen, K., Etzelmüller, B., & Gisnås, K. (2013). Ground Thermal Regime and Permafrost Distribution under a Changing Climate in Northern Norway. *Permafrost and Periglacial Processes*, *24*, 20–38. doi: 10.1002/ppp.1763

French, H. M. (2007). *The periglacial environment* (3rd ed.). Wiley.

Gisnås, K., Westermann, S., Schuler, T. V., Litherland, T., Isaksen, K., Boike, J., & Etzelmüller, B. (2014). A statistical approach to represent small-scale variability of permafrost temperatures due to snow cover. *The Cryosphere*, *8*, 2063–2074. doi: 10.5194/tcd-8-509-2014

Goodrich, L. E. (1982). The influence of snow cover on the ground thermal regime. *Canadian Geotechnical Journal*, *19*, 421–432. doi: 10.1039/B910216G

Gorbunov, A. P., Marchenko, S. S., & Seversky, E. V. (2004). The thermal environment of blocky materials in the mountains of Central Asia. *Permafrost and Periglacial Processes*, *15*, 95–98. doi: 10.1002/ppp.478

Gruber, S. (2005). *Mountain permafrost: transient spatial modelling, model verification and the use of remote sensing* (Ph.D. thesis). University of Zurich.

Gruber, S. (2012). Derivation and analysis of a high-resolution estimate of global permafrost zonation. *The Cryosphere*, *6*, 221–233. doi: 10.5194/tc-6-221-2012

Gruber, S., & Haeberli, W. (2007). Permafrost in steep bedrock slopes and its temperature-related destabilization following climate change. *Journal of Geophysical Research: Earth Surface*, *112*(2), 1–10. doi: 10.1029/2006JF000547

Gruber, S., & Haeberli, W. (2009). Mountain permafrost. In *Permafrost soils* (pp. 33–44). Springer. doi: 10.1007/978-3-540-69371-0

Gruber, S., & Hoelzle, M. (2001). Statistical Modelling of Mountain Permafrost Distribution: Local Calibration and Incorporation of Remotely Sensed Data. *Permafrost and Periglacial Processes*, *12*, 69–77. doi: 10.1002/ppp

Gruber, S., & Hoelzle, M. (2008). The cooling effect of coarse blocks revisited: a modeling study of a purely conductive mechanism. In *Proceedings of the 9th international conference on permafrost* (pp. 557–561). Fairbanks (Alaska).

Grumm, R. H., & Hart, R. (2001). Standardized anomalies applied to significant cold season weather events: Preliminary findings. *Weather and Forecasting*, *16*, 736–754. doi: 10.1175/1520-0434(2001)016<0736:SAATSC>2.0.CO;2

Gubler, S., Fiddes, J., Keller, M., & Gruber, S. (2011). Scale-dependent measurement and analysis of ground surface temperature variability in alpine terrain. *The Cryosphere*, *5*, 431–443. doi: 10.5194/tc-5-431-2011

Gudmundsson, L., Bremnes, J. B., Haugen, J. E., & Engen-Skaugen, T. (2012). Technical Note : Downscaling RCM precipitation to the station scale using statistical transformations – a comparison of methods. *Hydrology and Earth System Sciences*, *16*, 3383–3390. doi: 10.5194/hess-16-3383-2012

Haberkorn, A., Hoelzle, M., Phillips, M., & Kenner, R. (2015). Snow as a driving factor of rock surface temperatures in steep rough rock walls. *Cold Regions Science and Technology*, *118*, 64–75. doi: 10.1016/j.coldregions.2015.06.013

Haeberli, W., Arenson, L., Delaloye, R., Gruber, S., Isaksen, K., Kneisel, C., Krautblatter, M., Noetzli, J., & Phillips, M. (2010). Permafrost on mountain slopes – development and challenges of a young research field. *Journal of Glaciology*, *56*(200), 1043–1058. doi: 10.3189/002214311796406121

Haeberli, W., & Guodong, C. (1993). Mountain permafrost and climatic change. *Permafrost and Periglacial Processes*, *4*, 165–174. doi: 10.1002/ppp.3430040208

Hanson, S., & Hoelzle, M. (2004). The thermal regime of the active layer at the Murtèl rock glacier based on data from 2002. *Permafrost and Periglacial Processes*, *15*, 273–282. doi: 10.1002/ppp.499

Harris, C., Arenson, L., Christiansen, H. H., Etzelmüller, B., Frauenfelder, R., Gruber, S., Haeberli, W., Hauck, C., Hölzle, M., Humlum, O., Isaksen, K., Kääb, A., Kern-Lütschg, M., Lehning, M., Matsuoka, N., Murton, J. B., Noetzli, J., Phillips, M., Ross, N., Seppälä, M., Springman, S. M., & Vonder Mühll, D. (2009). Permafrost and climate in Europe: Monitoring and modelling thermal, geomorphological and geotechnical responses. *Earth-Science Reviews*, *92*, 117–171. doi: 10.1016/j.earscirev.2008.12.002

Harris, C., Vonder Mühll, D., Isaksen, K., Haeberli, W., Sollid, J. L., King, L., Holmlund, P., Dramis, F., Guglielmin, M., & Palacios, D. (2003). Warming permafrost in European mountains. *Global and Planetary Change*, *39*, 215–225. doi: 10.1016/j.gloplacha.2003.04.001

Harris, S. A., & Pedersen, D. E. (1998). Thermal Regimes Beneath Coarse Blocky Materials. *Permafrost and Periglacial Processes*, *9*, 107–120. doi: 10.1002/(SICI)1099-1530(199804/06)9

Hasler, A., Geertsema, M., Foord, V., Gruber, S., & Noetzli, J. (2015). The influence of surface characteristics, topography and continentality on mountain permafrost in British Columbia. *The Cryosphere*, *9*(3), 1025–1038. doi: 10.5194/tc-9-1025-2015

Hasler, A., Gruber, S., & Haeberli, W. (2011). Temperature variability and offset in steep alpine rock and ice faces. *The Cryosphere*, *5*(4), 977–988. doi: 10.5194/tc-5-977-2011

Hauck, C., Isaksen, K., Vonder Mühll, D., & Sollid, J. L. (2004). Geophysical surveys designed to delineate the altitudinal limit of mountain permafrost: An example from Jotunheimen, Norway. *Permafrost and Periglacial Processes*, *15*(3), 191–205. doi: 10.1002/ppp.493

Heggem, E. S. F., Juliussen, H., & Etzelmüller, B. (2005). Mountain permafrost in Central-Eastern Norway. *Norsk Geografisk Tidsskrift - Norwegian Journal of Geography*, *59*, 94–108. doi: 10.1080/00291950510038377

Herz, T., King, L., & Gubler, H. (2003). Microclimate within coarse debris of talus slopes in the alpine periglacial belt and its effects on permafrost. In *Proceedings of the 8th international conference of permafrost* (pp. 383–387). Zürich (Switzerland).

Hipp, T. F., Etzelmüller, B., Farbrot, H., Schuler, T. V., & Westermann, S. (2012). Modelling borehole temperatures in Southern Norway – insights into permafrost dynamics during the 20th and 21st century. *The Cryosphere*, *6*(3), 553–571. doi: 10.5194/tc-6-553-2012

Hoelzle, M. (1996). Mapping and modelling of mountain permafrost distribution in the Apls. *Norsk Geografisk Tidsskrift - Norwegian Journal of Geography*, *50*, 11–15.

Hoelzle, M., Mittaz, C., Etzelmüller, B., & Haeberli, W. (2001). Surface energy fluxes and distribution models of permafrost in European mountain areas: an overview of current developments. *Permafrost and Periglacial Processes*, *12*, 53–68. doi: 10.1002/ppp385

Isaksen, K., Ødegård, R. S., Etzelmüller, B., Hilbich, C., Hauck, C., Farbrot, H., Eiken, T., Hygen, H. O., & Hipp, T. F. (2011). Degrading mountain permafrost in Southern Norway: Spatial and temporal variability of mean ground temperatures, 1999-2009. *Permafrost and Periglacial Processes*, *22*(4), 361–377. doi: 10.1002/ppp.728

Isaksen, K., Sollid, J. L., Holmlund, P., & Harris, C. (2007). Recent warming of mountain permafrost in Svalbard and Scandinavia. *Journal of Geophysical Research*, *112*, 1–11. doi: 10.1029/2006JF000522

Juliussen, H., & Humlum, O. (2008). Thermal Regime of Openwork Block Fields on the Mountains Elagahogna and Solen, Central-eastern Norway. *Permafrost and Periglacial Processes*, *19*, 1–18. doi: 10.1002/ppp

Kane, D. L., Hinkel, K. M., Goering, D. J., Hinzman, L. D., & Outcalt, S. I. (2001). Non-conductive heat transfer associated with frozen soils. *Global and Planetary Change*, *29*, 275–292. doi: 10.1016/S0921-8181(01)00095-9

Lewkowicz, A. G., Bonnaventure, P. P., Smith, S. L., & Kuntz, Z. (2012). Spatial and thermal characteristics of mountain permafrost, northwest canada. *Geografiska Annaler, Series A: Physical Geography*, *94*(2), 195–213. doi: 10.1111/j.1468-0459.2012.00462.x

Luetschg, M., Lehning, M., & Haeberli, W. (2008). A sensitivity study of factors influencing

warm / thin permafrost in the Swiss Alps. *Journal of Glaciology*, *54*(187), 696–704.

Luetschg, M., Stoeckli, V., Lehning, M., Haeberli, W., & Ammann, W. (2004). Temperatures in two boreholes at Flüela Pass, Eastern Swiss Alps: the effect of snow redistribution on permafrost distribution patterns in high mountain areas. *Permafrost and Periglacial Processes*, *15*, 283–297. doi: 10.1002/ppp.500

Magnin, F., Deline, P., Ravanel, L., Noetzli, J., & Pogliotti, P. (2015). Thermal characteristics of permafrost in the steep alpine rock walls of the Aiguille du Midi (Mont Blanc Massif, 3842 m a.s.l). *The Cryosphere*, *9*, 109–121. doi: 10.5194/tc-9-109-2015

Meehl, G. A., Arblaster, J. M., Fasullo, J. T., Hu, A., & Trenberth, K. E. (2011). Model-based evidence of deep-ocean heat uptake during surface-temperature hiatus periods. *Nature Climate Change*, *1*, 360–364. doi: 10.1038/nclimate1229

MeteoSwiss. (2013). Anomalies of Mean Temperature: TanomD8110, TanomM8110, TanomY8110. *Documentation of MeteoSwiss Grid-Data Products*, 3.

Minder, J. R., Mote, P. W., & Lundquist, J. D. (2010). Surface temperature lapse rates over complex terrain: Lessons from the Cascade Mountains. *Journal of Geophysical Research*, *115*. doi: 10.1029/2009JD013493

Mittaz, C., Imhof, M., Hoelzle, M., & Haeberli, W. (2002). Snowmelt Evolution Mapping Using an Energy Balance Approach over an Alpine Terrain an Energy Snowmelt Evolution Balance over an Mapping Using Approach Terrain Alpine. *Arctic, Antarctic, and Alpine Research*, *34*, 274–281.

Morard, S., Delaloye, R., & Lambiel, C. (2010). Pluriannual thermal behavior of low elevation cold talus slopes in western Switzerland. *Geographica Helvetica*, *65*, 124–134. doi: 10.5194/gh-65-124-2010

Noetzli, J., & Gruber, S. (2005). Alpiner Permafrost – ein Überblick. *Jahrbuch des Vereins zum Schutz der Bergwelt*, *70*, 111–121.

Noetzli, J., & Gruber, S. (2009). Transient thermal effects in Alpine permafrost. *The Cryosphere*, *2*, 85–99. doi: 10.5194/tcd-2-185-2008

Noetzli, J., Gruber, S., Kohl, T., Salzmann, N., & Haeberli, W. (2007). Three-dimensional distribution and evolution of permafrost temperatures in idealized high-mountain topography. *Journal of Geophysical Research*, *112*, 1–14. doi: 10.1029/2006JF000545

Ohmura, A., & Raschke, E. (2005). Energy budget at the earth's surface. In M. Hantel (Ed.), *Observed global climate.* Berlin, Heidelberg: Springer Berlin Heidelberg.

Osterkamp, T. E., & Burn, C. R. (2003). Permafrost. In J. R. Holton, J. A. Curry, & J. A. Pyle (Eds.), *Encyclopedia of atmospheric sciences* (pp. 1717–1729). doi: 10.1016/B0-12-227090-8/00311-0

PERMOS. (2013). Permafrost in Switzerland 2008/2009 and 2009/2010. *Glaciological Report Permafrost*, *10/11*.

Plüss, C. (1997). The energy balance over an Alpine snowcover. *Zürcher Geographische Schriften*, *65*, 115.

Pogliotti, P., Guglielmin, M., Cremonese, E., Morra di Cella, U., Filippa, G., Pellet, C., & Hauck, C. (2015). Warming permafrost and active layer variability at Cime Bianche, Western European Alps. *The Cryosphere*, *9*, 647–661. doi: 10.5194/tc-9-647-2015

R Core Team. (2015). *R: A Language and Environment for Statistical Computing.* Vienna,

Austria: R Foundation for Statistical Computing. Retrieved from `https://www.r-project.org/`

Rolland, C. (2003). Spatial and seasonal variations of air temperature lapse rates in alpine regions. *Journal of Climate*, *16*(7), 1032–1046. doi: 10.1175/1520-0442(2003)016<1032:SASVOA>2.0.CO;2

Romanovsky, V. E., & Osterkamp, T. E. (2000). Effects of unfrozen water on heat and mass transport processes in the active layer and permafrost. *Permafrost and Periglacial Processes*, *11*, 219–239. doi: 10.1002/1099-1530(200007/09)11:3<219::AID-PPP352>3.0.CO;2-7

Romanovsky, V. E., Smith, S. L., & Christiansen, H. H. (2010). Permafrost thermal state in the polar northern hemisphere during the international polar year 2007-2009: A synthesis. *Permafrost and Periglacial Processes*, *21*(2), 106–116. doi: 10.1002/ppp.689

Šafanda, J. (1999). Ground surface temperature as a function of slope angle and slope orientation and its effect on the subsurface temperature field. *Tectonophysics*, *306*(3-4), 367–375. doi: 10.1016/S0040-1951(99)00066-9

Schneider, S., Hoelzle, M., & Hauck, C. (2012). Influence of surface and subsurface heterogeneity on observed borehole temperatures at a mountain permafrost site in the Upper Engadine, Swiss Alps. *The Cryosphere*, *6*(2), 517–531. doi: 10.5194/tc-6-517-2012

Schuenemeyer, J. H., & Drew, L. J. (2010). Regression. In *Statistics for earth and environmental scientists* (pp. 99–149). John Wiley & Sons, Inc. doi: 10.1002/9780470650707.ch4

Smerdon, J. E., Pollack, H. N., Enz, J. W., & Lewis, M. J. (2003). Conduction-dominated heat transport of the annual temperature signal in soil. *Journal of Geophysical Research*, *108*, 1–6. doi: 10.1029/2002JB002351

Smith, M. W., & Riseborough, D. W. (2002). Climate and the limits of permafrost: a zonal analysis. *Permafrost and Periglacial Processes*, *13*(1), 1–15. doi: 10.1002/ppp.410

Stahel, W. A. (2008). *Statistische Datenanalyse: Eine Einführung für Naturwissenschaftler* (5th ed.). Wiesbaden: Vieweg.

Staub, B., & Delaloye, R. (2016). Using Near-Surface Ground Temperature Data to Derive Snow Insulation and Melt Indices for Mountain Permafrost Applications. *Permafrost and Periglacial Processes*. doi: 10.1002/ppp.1890

Staub, B., Hasler, A., Noetzli, J., & Delaloye, R. (accepted). Gap filling algorithm for ground surface temperature data. *Permafrost and Periglacial Processes*.

Staub, B., Marmy, A., Hauck, C., Hilbich, C., & Delaloye, R. (2015). Ground temperature variations in a talus slope influenced by permafrost: a comparison of field observations and model simulations. *Geographica Helvetica*, *70*, 45–62. doi: 10.5194/gh-70-45-2015

Trenberth, K. E., Jones, P. D., Ambenje, P., Bojariu, R., Easterling, D., Klein Tank, A., Parker, D., Rahimzadeh, F., Renwick, J. A., Rusticucci, M., Soden, B., & Zhai, P. (2007). Observations: Surface and Atmospheric Climate. In *Climate change 2007: The physical science basis. contribution of working group i to the fourth assessment report of the intergovernmental panel on climate change.* (pp. 235–336). New York: Cambridge University Press.

van den Broeke, M., Reijemer, C., & van de Wal, R. (2004). Surface radiation balance in Antarctica as measured with automatic weather stations. *Journal of Geophysical Research*, *109*, 1–16. doi: 10.1029/2003JD004394

Vonder Mühll, D., Noetzli, J., & Roer, I. (2008). PERMOS – A Comprehensive Monitoring Network of Mountain Permafrost in the Swiss Alps. In *Proceedings of the 9th international conference on permafrost* (pp. 1869–1874). Fairbanks (Alaska). doi: 10.5167/uzh-4288

von Storch, H. (1995). Misuses of Statistical Analysis in Climate. In *Analysis of climate variability: Applications of statistical techniques* (pp. 11–26). Berlin: Springer.

Wilks, D. S. (2006). Empirical distributions and exploratory data analysis. In *Statistical methods in the atmospheric sciences* (2nd ed., p. 627). Amsterdam: Elsevier.

Williams, P. J., & Smith, M. W. (1989). *The Frozen Earth: Fundamentals of Geocryology*. Cambridge: Cambridge University Press.

Wüthrich, C., Scherrer, S. C., Begert, M., Croci-Maspoli, M., Marty, C., Seiz, G., Foppa, N., Konzelmann, T., & Appenzeller, C. (2010). Die langen Schneemessreihen der MeteoSchweiz - Eine basisklimatologische Netzanalyse und Bestimmung besonders wertvoller Stationen mit Messbeginn vor 1961. *Arbeitsberichte der MeteoSchweiz*(233), 33.

Yue, S., & Wang, C. Y. (2002). Applicability of prewhitening to eliminate the influence of serial correlation on the Mann-Kendall test. *Water Resources Research*, *38*(6), 4–1–4–7. doi: 10.1029/2001WR000861

Zenklusen Mutter, E., Blanchet, J., & Phillips, M. (2010). Analysis of ground temperature trends in Alpine permafrost using generalized least squares. *Journal of Geophysical Research*, *115*(4), 1–12. doi: 10.1029/2009JF001648

Zenklusen Mutter, E., & Phillips, M. (2012). Active Layer Characteristics At Ten Borehole Sites In Alpine Permafrost Terrain, Switzerland. *Permafrost and Periglacial Processes*, *23*(2), 138–151. doi: 10.1002/ppp.1738

Zhang, T. (2005). Influence of seasonal snow cover on the ground thermal regime: An overview. *Reviews in Geophysics*, *43*. doi: 10.1029/2004RG000157

Appendix

A Miscellaneous

Table 7.1: Thermal conductivity of different soil constituents (Williams & Smith, 1989).

Soil constituents	Thermal conductivity [W $m^{-1}K^{-1}$]
Quartz	8.80
Clay minerals	2.29
Organic matter	0.25
Water [0°C]	0.56
Ice [0°C]	2.24
Air	0.025

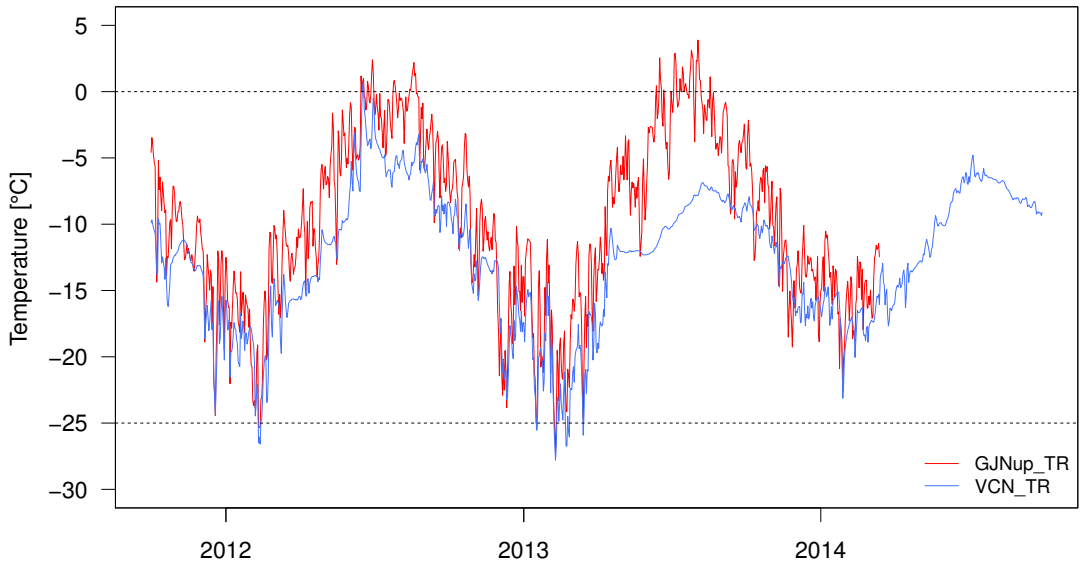

Figure 7.1: Daily GST records from high altitude measurement locations within Alpine terrain. `GJNup_TR` is measured at 4100 m asl. on the Grand Jorasses, `VCN_TR` is measured at 4450 m asl. on the Matterhorn. Data source: ARPA VDA (L'Agenzia Regionale per la Protezione dell' Ambiente della Valle d'Aosta).

B Characteristics of ground surface temperatures

Table 7.2: Meta data of the measurement devices used for the description of GST characteristics.

Name of measurement device	Type of surface material	Slope [°]	Aspect [°]	Elevation [m asl.]	Project
AGE_S001	debris	7.8	127.8	2851.1	PERMOS
AGE_S002	debris	8.3	187.3	2828.1	PERMOS
AGE_S004	debris	8.0	107.1	2842.3	PERMOS
AGE_S005	debris	17.8	276.2	2883.2	PERMOS
AGE_S006	debris	29.1	127.9	2910.0	PERMOS
AGE_S007	coarse blocks	12.1	143.2	2881.2	PERMOS
ATT_S002	soil	33.4	266.9	2712.8	PERMOS
ATT_S003	debris	26.0	269.6	2682.1	PERMOS
ATT_S004	coarse blocks	20.2	273.7	2653.2	PERMOS
ATT_S008	debris	29.4	315.6	2748.8	PERMOS
ATT_S011	debris	32.3	297.7	2712.8	PERMOS
ATT_S013	debris	29.1	269.1	2698.1	PERMOS
ATT_S020	debris	30.6	293.5	2680.4	PERMOS
ATT_S021	coarse blocks	27.4	286.2	2667.0	PERMOS
ATT_S022	coarse blocks	26.4	287.1	2649.9	PERMOS
COR_R002	bedrock	4.4	49.6	2532.6	PERMOS
COR_R003	bedrock	9.1	51.7	2633.1	PERMOS
COR_R005	bedrock	43.9	273.3	2767.5	PERMOS
COR_R006	bedrock	56.5	316.7	3277.0	PERMOS
COR_R007	bedrock	15.4	238.2	3287.9	PERMOS
COR_R008	bedrock	32.4	137.2	3290.1	PERMOS
COR_R009	bedrock	41.9	153.2	2835.0	PERMOS
COR_R010	bedrock	50.2	100.7	2832.2	PERMOS
COR_R011	bedrock	15.2	351.9	2735.8	PERMOS
COR_R012	bedrock	14.6	44.8	2767.3	PERMOS
DRE_S010	coarse blocks	23.8	284.3	1745.1	PERMOS
DRE_S012	coarse blocks	33.4	76.8	1573.5	PERMOS
DRE_S013	coarse blocks	36.6	78.0	1585.9	PERMOS
DRE_S014	coarse blocks	34.8	82.7	1595.0	PERMOS
DRE_S015	coarse blocks	35.6	85.1	1623.5	PERMOS
GFU_S002	coarse blocks	20.3	334.9	2461.7	PERMOS
GFU_S004	coarse blocks	17.1	6.2	2500.4	PERMOS
GFU_S005	coarse blocks	20.3	8.6	2520.8	PERMOS
GFU_S007	coarse blocks	26.5	335.0	2534.9	PERMOS
GFU_S008	coarse blocks	28.3	357.1	2526.1	PERMOS
GFU_S010	debris	27.9	19.5	2479.2	PERMOS
GFU_S011	coarse blocks	27.4	313.0	2486.8	PERMOS

Name of measurement device	Type of surface material	Slope [°]	Aspect [°]	Elevation [m asl.]	Project
GFU_S017	coarse blocks	23.3	27.8	2490.6	PERMOS
GFU_S032	debris	34.2	4.4	2501.4	PERMOS
GFU_S036	coarse blocks	18.9	336.5	2557.7	PERMOS
JFJ_R004	bedrock	38.2	69.7	3730.9	PERMOS
JFJ_R005	bedrock	61.4	356.5	3715.5	PERMOS
LAP_S015	coarse blocks	27.2	6.6	2512.7	PERMOS
LAP_S028	coarse blocks	22.9	12.7	2451.4	PERMOS
LAP_S031	coarse blocks	17.0	47.3	2392.8	PERMOS
LAP_S035	coarse blocks	21.6	21.3	2412.3	PERMOS
LAP_S037	debris	21.4	39.1	2495.0	PERMOS
MIL_S002	coarse blocks	32.7	47.8	2427.8	PERMOS
MIL_S003	coarse blocks	17.4	57.2	2414.9	PERMOS
MIL_S004	coarse blocks	13.1	46.7	2408.4	PERMOS
MIL_S005	coarse blocks	9.5	33.2	2400.6	PERMOS
MIL_S008	coarse blocks	24.0	43.5	2377.3	PERMOS
MIL_S009	coarse blocks	33.4	55.7	2347.3	PERMOS
MIL_S010	coarse blocks	20.5	49.0	2338.8	PERMOS
MIL_S021	soil	27.3	17.4	2366.7	PERMOS
MIL_S024	coarse blocks	21.5	52.7	2441.1	PERMOS
MIL_S031	debris	14.9	357.4	2302.6	PERMOS
MIL_S032	soil	35.9	352.4	2295.9	PERMOS
MIL_S034	coarse blocks	11.6	341.5	2257.7	PERMOS
MIL_S035	coarse blocks	22.5	33.1	2226.9	PERMOS
MIL_S036	soil	28.8	340.1	2306.5	PERMOS
MIL_S041	debris	39.5	46.0	2432.5	PERMOS
MIL_S043	debris	42.5	41.7	2437.9	PERMOS
MIL_S044	debris	33.5	47.3	2428.3	PERMOS
REC_S006	coarse blocks	4.9	353.3	2791.7	PERMOS
REC_S007	coarse blocks	13.5	17.3	2804.5	PERMOS
REC_S008	coarse blocks	20.0	350.4	2817.7	PERMOS
REC_S143	coarse blocks	10.9	252.5	2651.0	PERMOS
RTD_S005	debris	5.1	31.6	2849.5	TEMPS
RTD_S007	coarse blocks	6.3	318.5	2835.3	TEMPS
SCH_R007	bedrock	7.0	74.3	2406.8	PERMOS
SCH_R009	bedrock	32.5	179.0	2677.5	PERMOS
SCH_R011	bedrock	17.8	99.7	2792.5	PERMOS
SCH_S003	debris	37.0	226.3	2939.1	PERMOS
SCH_S017	debris	34.8	22.5	2831.9	PERMOS
YET_S004	coarse blocks	11.4	339.5	2744.4	PERMOS
YET_S014	coarse blocks	20.6	42.5	2715.3	PERMOS
YET_S016	coarse blocks	10.4	54.9	2681.9	PERMOS

C Trend

Table 7.3: Meta data of the measurement devices used for trend analysis.

Name of measurement device	Type of surface material	Slope [°]	Aspect [°]	Elevation [m asl.]	Project
AGE_S001	debris	7.8	127.8	2851.1	PERMOS
AGE_S002	debris	8.3	187.3	2828.1	PERMOS
AGE_S005	debris	17.8	276.2	2883.2	PERMOS
AGE_S006	debris	29.1	127.9	2910.0	PERMOS
AGE_S007	coarse blocks	12.1	143.2	2881.2	PERMOS
GFU_S003	coarse blocks	21.3	347.9	2471.9	PERMOS
GFU_S010	debris	27.9	19.5	2479.2	PERMOS
GFU_S017	coarse blocks	23.3	27.8	2490.6	PERMOS
LAP_S015	coarse blocks	27.2	6.6	2512.7	PERMOS
LAP_S028	coarse blocks	22.9	12.7	2451.4	PERMOS
MIL_S002	coarse blocks	32.7	47.8	2427.8	PERMOS
MIL_S003	coarse blocks	17.4	57.2	2414.9	PERMOS
MIL_S004	coarse blocks	13.1	46.7	2408.4	PERMOS
MIL_S005	coarse blocks	9.5	33.2	2400.6	PERMOS
MIL_S009	coarse blocks	33.4	55.7	2347.3	PERMOS
MIL_S021	soil	27.3	17.4	2366.7	PERMOS
MIL_S024	coarse blocks	21.5	52.7	2441.1	PERMOS
MIL_S032	soil	35.9	352.4	2295.9	PERMOS
MIL_S034	coarse blocks	11.6	341.5	2257.7	PERMOS
MIL_S035	coarse blocks	22.5	33.1	2226.9	PERMOS
MIL_S036	soil	28.8	340.1	2306.5	PERMOS
RTD_S001	debris	43.1	4.2	2497.1	TEMPS
RTD_S002	debris	27.6	342.8	2739.5	TEMPS
RTD_S006	coarse blocks	15.8	263.2	2862.8	TEMPS
RTD_S008	debris	34.0	254.6	2828.8	TEMPS
RTD_S009	coarse blocks	18.0	279.3	2861.6	TEMPS
RTD_S010	debris	14.2	350.7	2956.0	TEMPS
RTD_S011	debris	15.3	285.5	2909.2	TEMPS
RTD_S014	debris	20.2	264.9	2884.1	TEMPS
RTD_S015	coarse blocks	29.9	293.6	2816.1	TEMPS
RTD_S016	debris	26.3	254.1	2810.8	TEMPS
RTD_S017	coarse blocks	29.2	258.2	2815.3	TEMPS
RTD_S018	coarse blocks	17.5	225.6	2853.0	TEMPS
RTD_S019	coarse blocks	10.9	159.1	2872.6	TEMPS
RTD_S020	coarse blocks	35.4	325.8	2859.7	TEMPS
YET_S004	coarse blocks	11.4	339.5	2744.4	PERMOS

Table 7.4: Seasonal trends of GST, Monte Carlo method and AT for GST time series with lengths of 15 years for winter.

Name of logger	P-value of GST trend	Trend of GST [°C]	Number of signif. trends in MCM	μ of MCM trends [°C]	σ of MCM trends [°C]	P-value of AT trend	Trend of AT [°C]
AGE_S001	0.45	0.44	0	0.48	0.1	0.47	-1.2
AGE_S002	0.29	1.19	0	1.22	0.11	0.48	-2.11
AGE_S005	0.59	0.54	0	0.65	0.11	0.47	-0.74
AGE_S006	0.72	-0.25	0	-0.26	0.1	0.47	-0.76
AGE_S007	0.91	0.14	0	0.33	0.11	0.46	-2.01
GFU_S003	0.19	-1.49	0	-1.46	0.1	0.67	-2.55
GFU_S010	0.48	0.65	0	0.73	0.11	0.69	-2.51
GFU_S017	0.72	0.28	0	0.28	0.1	0.67	-1.82
LAP_S015	0.54	0.57	0	0.61	0.1	0.56	-1.56
LAP_S028	0.09	1.75	0	1.72	0.1	0.55	-4.3
MIL_S002	0.47	0.72	0	0.83	0.11	0.53	-0.72
MIL_S003	0.22	1.82	0	1.8	0.1	0.51	-5.82
MIL_S004	0.29	1.39	0	1.46	0.1	0.51	-7.95
MIL_S005	0.39	1.02	0	1.01	0.1	0.52	-5.79
MIL_S009	0.65	-0.55	0	-0.57	0.1	0.54	-6.57
MIL_S021	0.71	0.23	0	0.26	0.1	0.52	-0.49
MIL_S024	0.42	1.18	0	1.18	0.1	0.53	-4.39
MIL_S032	0.72	0.3	0	0.28	0.1	0.51	-0.18
MIL_S034	0.21	1.85	0	1.81	0.11	0.53	-5.24
MIL_S035	0.71	0.47	0	0.45	0.1	0.52	-5.48
MIL_S036	0.93	0.08	0	0.1	0.1	0.54	-0.52
RTD_S001	0.42	-1.61	0	-1.61	0.1	0.49	-7.18
RTD_S002	0.8	0.49	0	0.52	0.1	0.47	-8.14
RTD_S006	0.53	0.74	0	0.76	0.1	0.47	-5.23
RTD_S008	0.68	0.34	0	0.43	0.11	0.47	-0.14
RTD_S009	0.78	0.41	0	0.39	0.1	0.47	-5.45
RTD_S010	0.98	-0.03	0	0.06	0.1	0.46	-2.9
RTD_S011	0.47	-0.92	0	-0.98	0.1	0.47	-6.03
RTD_S014	0.86	0.08	0	0.1	0.11	0.47	-0.2
RTD_S015	0.39	1.46	0	1.51	0.1	0.47	-6.16
RTD_S016	0.6	0.55	0	0.61	0.1	0.47	-1
RTD_S017	0.89	0.15	0	0.16	0.1	0.47	-3.59
RTD_S018	0.26	0.9	0	0.94	0.12	0.47	-0.91
RTD_S019	0.89	0.17	0	0.45	0.12	0.47	-1.51
RTD_S020	0.59	0.85	0	0.83	0.1	0.46	-4.99
YET_S004	0.71	0.48	0	0.67	0.11	0.55	-3

Table 7.5: Seasonal trends of GST, Monte Carlo method and AT for GST time series with lengths of 15 years for spring.

Name of logger	P-value of GST trend	Trend of GST [°C]	Number of signif. trends in MCM	μ of MCM trends [°C]	σ of MCM trends [°C]	P-value of AT trend	Trend of AT [°C]
AGE_S001	0.33	0.38	0	0.42	0.11	0.97	-0.63
AGE_S002	0.26	0.38	0	0.39	0.11	0.96	-0.61
AGE_S005	0.77	0.16	0	0.23	0.11	0.97	-0.62
AGE_S006	0.26	0.31	0	0.3	0.11	0.96	-0.62
AGE_S007	0.69	0.23	0	0.29	0.11	0.97	-1.52
GFU_S003	0.99	-0.01	0	0.01	0.1	0.97	-1.7
GFU_S010	0.57	0.42	0	0.6	0.12	0.99	-2.13
GFU_S017	0.56	0.22	0	0.25	0.11	1	-0.84
LAP_S015	0.72	-0.09	0	-0.08	0.1	0.99	-1.02
LAP_S028	0.11	0.97	0	0.98	0.1	0.97	-2.35
MIL_S002	0.66	0.22	0	0.2	0.1	0.98	-0.39
MIL_S003	0.15	1.01	0	1.02	0.1	0.99	-3.02
MIL_S004	0.1	0.92	438	0.9	0.11	0.99	-2.74
MIL_S005	0.17	0.76	7	0.76	0.1	0.99	-2.87
MIL_S009	0.94	0.07	0	0.08	0.1	0.98	-2.25
MIL_S021	0.99	0	0	0	0.1	0.99	-0.13
MIL_S024	0.31	0.65	0	0.67	0.1	1	-2.32
MIL_S032	0.99	0	0	0	0.1	0.99	-0.1
MIL_S034	0.49	0.29	1	0.28	0.11	1	-1.99
MIL_S035	0.92	-0.09	0	-0.11	0.11	0.98	-2.66
MIL_S036	0.09	-0.74	0	-0.73	0.1	0.97	-0.03
RTD_S001	0.68	-0.28	0	-0.23	0.1	0.99	-2.79
RTD_S002	0.98	-0.01	0	0	0.1	1	-3.79
RTD_S006	0.41	0.52	0	0.48	0.1	0.99	-2.98
RTD_S008	0.68	0.11	0	0.11	0.1	0.99	-0.19
RTD_S009	0.32	0.71	0	0.69	0.1	0.97	-3.52
RTD_S010	1	0	0	-0.03	0.1	0.97	-2.74
RTD_S011	0.45	0.62	0	0.61	0.1	0.97	-3.04
RTD_S014	0.87	0.03	0	0.03	0.1	0.96	-0.05
RTD_S015	0.17	0.68	10	0.67	0.1	1	-2.1
RTD_S016	0.75	0.09	0	0.09	0.1	0.98	-0.24
RTD_S017	0.96	0.02	0	0.01	0.1	0.99	-1.14
RTD_S018	0.2	0.53	0	0.54	0.12	0.95	-0.71
RTD_S019	0.2	1.05	0	1.22	0.13	0.96	-1.08
RTD_S020	0.46	0.76	0	0.71	0.11	0.98	-3.09
YET_S004	0.57	0.48	0	0.53	0.11	0.97	-2.46

Table 7.6: Seasonal trends of GST, Monte Carlo method and AT for GST time series with lengths of 15 years for summer.

Name of logger	P-value of GST trend	Trend of GST [°C]	Number of signif. trends in MCM	μ of MCM trends [°C]	σ of MCM trends [°C]	P-value of AT trend	Trend of AT [°C]
AGE_S001	0.39	-1.08	0	-1.02	0.1	0.7	4.66
AGE_S002	0.7	-0.45	0	-0.37	0.1	0.73	4.67
AGE_S005	0.57	-0.68	0	-0.71	0.1	0.7	3.56
AGE_S006	0.94	-0.07	0	-0.04	0.1	0.73	4.92
AGE_S007	0.88	-0.13	0	-0.13	0.1	0.72	2.36
GFU_S003	0.08	2.36	0	2.33	0.09	0.71	4.48
GFU_S010	0.77	-0.33	0	-0.28	0.1	0.77	5.45
GFU_S017	0.81	-0.26	0	-0.18	0.1	0.72	7.05
LAP_S015	0.71	-0.43	0	-0.38	0.1	0.71	4.78
LAP_S028	0.62	0.55	0	0.63	0.1	0.71	4.86
MIL_S002	0.18	-1.33	0	-1.27	0.1	0.62	8.68
MIL_S003	0.53	-0.63	0	-0.54	0.1	0.62	6.23
MIL_S004	0.65	-0.42	0	-0.31	0.1	0.62	7.49
MIL_S005	0.03	-2.66	432	-2.73	0.12	0.61	8.57
MIL_S009	0.41	-0.68	0	-0.59	0.11	0.63	7.2
MIL_S021	0.2	-1.74	0	-1.63	0.11	0.62	6.44
MIL_S024	0.81	-0.28	0	-0.09	0.1	0.6	6.12
MIL_S032	0.31	-1.05	0	-0.97	0.11	0.63	6.49
MIL_S034	0.11	-1.64	0	-1.66	0.13	0.61	6.57
MIL_S035	0.24	-0.87	0	-0.83	0.11	0.62	6.54
MIL_S036	0.24	-0.79	0	-0.78	0.1	0.61	6.72
RTD_S001	0.27	-0.77	0	-0.7	0.11	0.62	5.22
RTD_S002	0.76	-0.19	0	-0.12	0.11	0.67	3.47
RTD_S006	0.36	0.53	0	0.49	0.09	0.7	1.99
RTD_S008	0.23	-1.33	0	-1.29	0.1	0.71	7.13
RTD_S009	0.17	-0.99	0	-0.98	0.1	0.7	3.69
RTD_S010	0.58	-0.67	0	-0.66	0.1	0.73	3.78
RTD_S011	0.27	-0.68	0	-0.69	0.11	0.7	2.78
RTD_S014	0.81	-0.29	0	-0.25	0.1	0.69	5.24
RTD_S015	0.11	-1.4	0	-1.35	0.11	0.68	4.73
RTD_S016	0.39	-0.94	0	-0.91	0.11	0.7	5.19
RTD_S017	0.67	-0.39	0	-0.24	0.1	0.69	4.57
RTD_S018	0.62	-0.53	0	-0.43	0.11	0.69	3.73
RTD_S019	0.48	-0.75	0	-0.78	0.11	0.72	4.37
RTD_S020	0.66	-0.36	0	-0.24	0.1	0.71	3.42
YET_S004	0.72	-0.4	0	-0.28	0.11	0.72	1.38

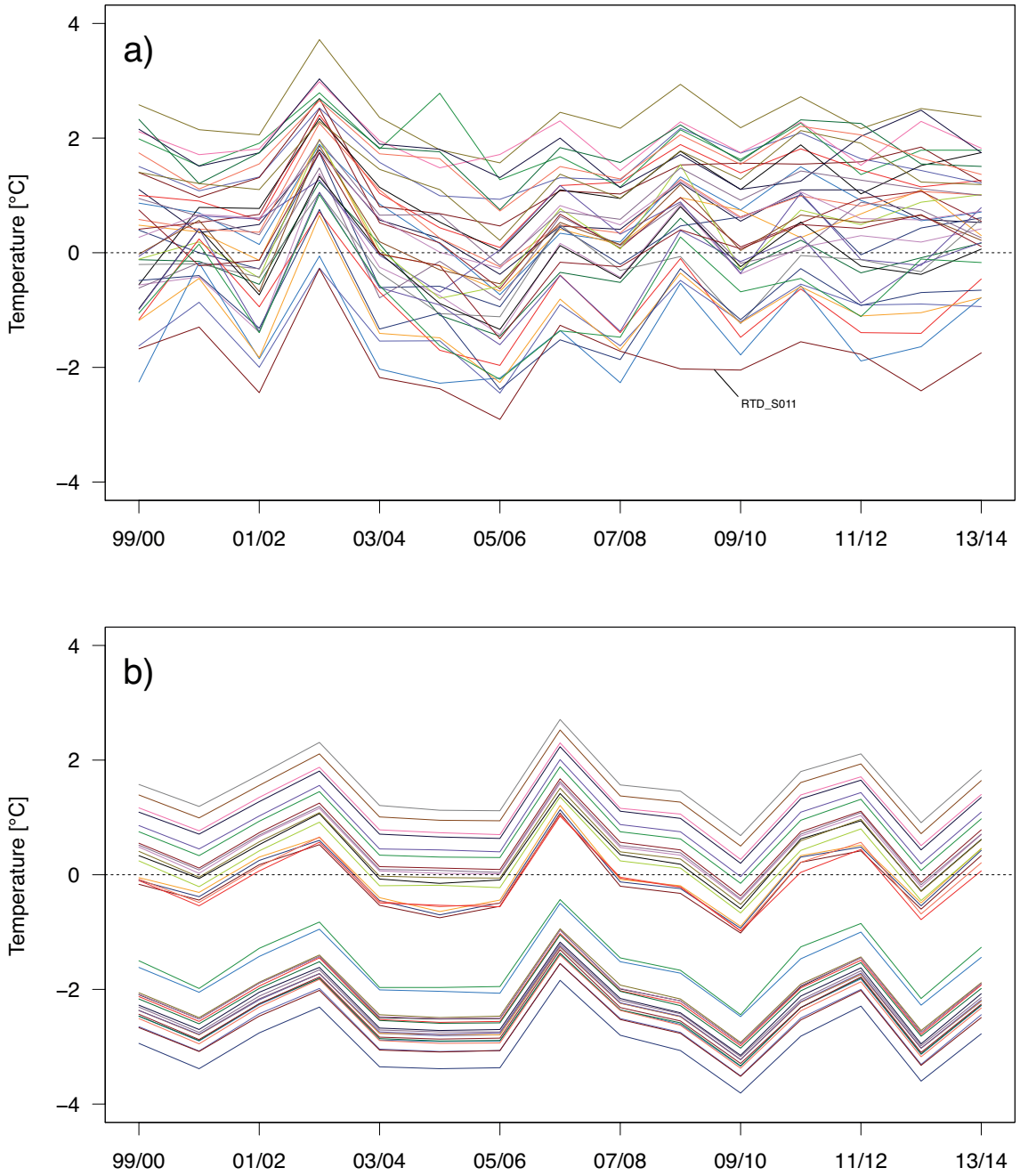

Figure 7.2: Inter annual variability of MAGST (**a)**) and MAAT (**b)**) from time series used in trend analysis for hydrological years 2000 - 2014.

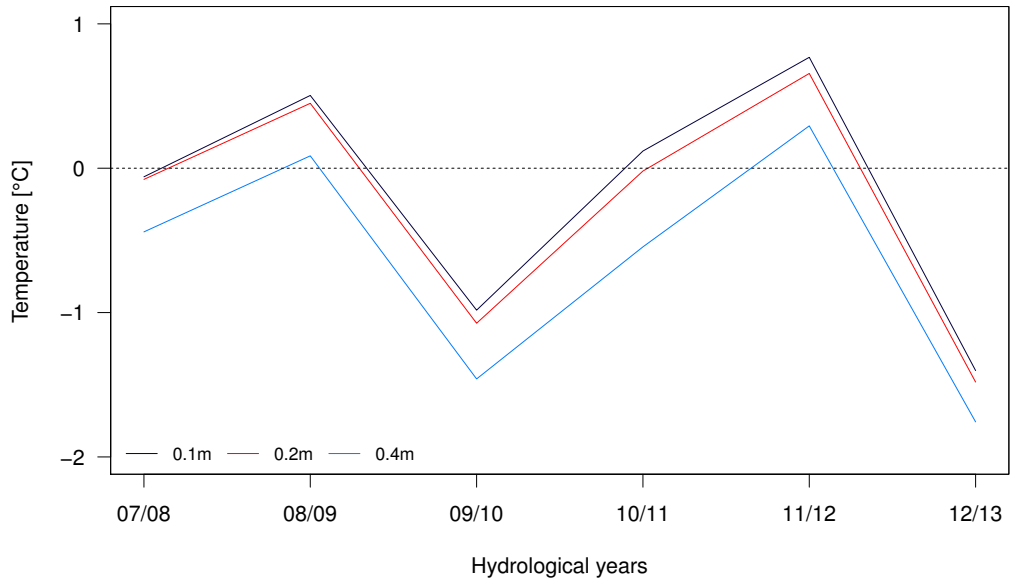

Figure 7.3: MAGT from borehole `Ritigraben 0102` at depths of 0.1, 0.2 and 0.4 m.

Table 7.7: Mean differences of MAGT between depths of 0.1, 0.2 and 0.4 m.

Δ depth	Mean difference [°C]
10cm	0.082
20cm	0.38
30cm	0.462

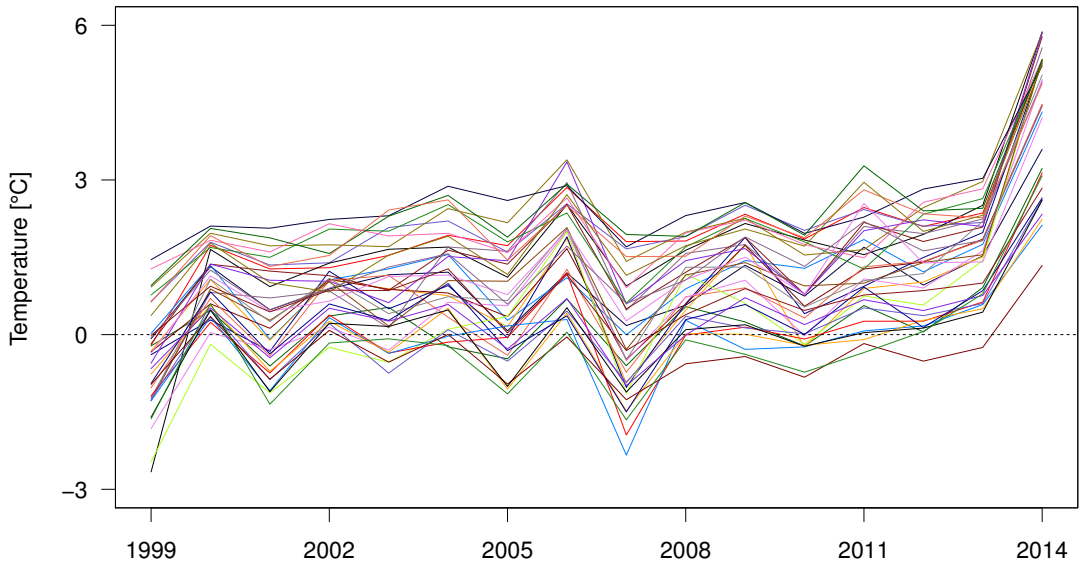

Figure 7.4: Mean GST for autumn (September, October, November) for the years 1999 – 2014.

D Spatial variability

Table 7.8: Meta data of measurement devices used for multiple linear regression model from projects *PERMOS* and *TEMPS*.

Name of measurement device	Type of surface material	Slope [°]	Aspect [°]	Elevation [m asl.]	Project
AGE_S001	debris	7.8	127.8	2851.1	PERMOS
AGE_S002	debris	8.3	187.3	2828.1	PERMOS
AGE_S003	debris	6.3	111.7	2834.6	PERMOS
AGE_S004	debris	8.0	107.1	2842.3	PERMOS
AGE_S005	debris	17.8	276.2	2883.2	PERMOS
AGE_S006	debris	29.1	127.9	2910.0	PERMOS
AGE_S007	coarse blocks	12.1	143.2	2881.2	PERMOS
ATT_S002	soil	33.4	266.9	2712.8	PERMOS
ATT_S003	debris	26.0	269.6	2682.1	PERMOS
ATT_S004	coarse blocks	20.2	273.7	2653.2	PERMOS
ATT_S005	debris	26.2	286.3	2649.8	PERMOS
ATT_S007	debris	31.0	299.3	2722.0	PERMOS
ATT_S008	debris	29.4	315.6	2748.8	PERMOS
ATT_S009	debris	35.5	298.9	2756.3	PERMOS
ATT_S010	debris	32.7	270.5	2767.6	PERMOS
ATT_S011	debris	32.3	297.7	2712.8	PERMOS
ATT_S013	debris	29.1	269.1	2698.1	PERMOS
ATT_S020	debris	30.6	293.5	2680.4	PERMOS
ATT_S021	coarse blocks	27.4	286.2	2667.0	PERMOS
ATT_S022	coarse blocks	26.4	287.1	2649.9	PERMOS
COR_R001	bedrock	11.8	3.3	2625.1	PERMOS
COR_R002	bedrock	4.4	49.6	2532.6	PERMOS
COR_R003	bedrock	9.1	51.7	2633.1	PERMOS
COR_R004	bedrock	4.9	352.5	2665.5	PERMOS
COR_R005	bedrock	43.9	273.3	2767.5	PERMOS
COR_R006	bedrock	56.5	316.7	3277.0	PERMOS
COR_R007	bedrock	15.4	238.2	3287.9	PERMOS
COR_R008	bedrock	32.4	137.2	3290.1	PERMOS
COR_R010	bedrock	50.2	100.7	2832.2	PERMOS
COR_R011	bedrock	15.2	351.9	2735.8	PERMOS
COR_R012	bedrock	14.6	44.8	2767.3	PERMOS
COR_S001	coarse blocks	11.9	288.7	2647.7	PERMOS
COR_S002	coarse blocks	1.5	317.0	2646.8	PERMOS
COR_S003	coarse blocks	7.3	311.1	2650.0	PERMOS
COR_S004	soil	16.8	300.4	2629.0	PERMOS
COR_S005	coarse blocks	24.2	352.6	2629.7	PERMOS
COR_S006	coarse blocks	25.6	324.1	2619.1	PERMOS

Name of measurement device	Type of surface material	Slope [°]	Aspect [°]	Elevation [m asl.]	Project
COR_S008	coarse blocks	20.9	343.5	2569.0	PERMOS
GEN_S002	soil	4.4	205.8	2897.0	PERMOS
GEN_S005	coarse blocks	34.2	246.7	2880.7	PERMOS
GEN_S006	debris	12.1	145.8	2871.4	PERMOS
GEN_S007	debris	21.8	158.5	2883.8	PERMOS
GEN_S009	debris	11.8	108.5	2870.6	PERMOS
GEN_S010	debris	23.1	25.1	2866.0	PERMOS
GEN_S011	debris	23.7	67.1	2881.2	PERMOS
GEN_S012	coarse blocks	34.6	64.9	2876.9	PERMOS
GFU_S001	soil	24.1	345.7	2457.5	PERMOS
GFU_S002	coarse blocks	20.3	334.9	2461.7	PERMOS
GFU_S003	coarse blocks	21.3	347.9	2471.9	PERMOS
GFU_S004	coarse blocks	17.1	6.2	2500.4	PERMOS
GFU_S005	coarse blocks	20.3	8.6	2520.8	PERMOS
GFU_S007	coarse blocks	26.5	335.0	2534.9	PERMOS
GFU_S008	coarse blocks	28.3	357.1	2526.1	PERMOS
GFU_S009	coarse blocks	39.0	10.9	2476.1	PERMOS
GFU_S010	debris	27.9	19.5	2479.2	PERMOS
GFU_S011	coarse blocks	27.4	313.0	2486.8	PERMOS
GFU_S012	debris	30.0	18.5	2534.8	PERMOS
GFU_S014	coarse blocks	18.8	346.3	2536.7	PERMOS
GFU_S015	coarse blocks	15.3	306.2	2512.5	PERMOS
GFU_S016	coarse blocks	21.6	17.6	2496.1	PERMOS
GFU_S017	coarse blocks	23.3	27.8	2490.6	PERMOS
GFU_S027	coarse blocks	30.8	35.6	2464.9	PERMOS
GFU_S031	coarse blocks	25.7	9.0	2508.0	PERMOS
GFU_S032	debris	34.2	4.4	2501.4	PERMOS
GFU_S036	coarse blocks	18.9	336.5	2557.7	PERMOS
GFU_S103	coarse blocks	25.8	313.8	2654.4	PERMOS
GFU_S106	coarse blocks	21.9	339.8	2641.5	PERMOS
GFU_S107	coarse blocks	11.7	308.0	2634.7	PERMOS
GFU_S111	coarse blocks	24.5	301.8	2586.2	PERMOS
GGU_S013	debris	26.7	333.7	2390.8	PERMOS
GGU_S045	debris	28.3	273.2	2458.8	PERMOS
GGU_S073	debris	19.1	1.3	2542.9	PERMOS
HUT_S009	coarse blocks	12.6	335.9	2655.7	TEMPS
HUT_S014	coarse blocks	17.4	316.4	2560.9	TEMPS
HUT_S016	coarse blocks	27.3	330.4	2707.7	TEMPS
HUT_S019	coarse blocks	24.6	343.7	2537.0	TEMPS
HUT_S021	coarse blocks	23.6	325.3	2666.2	TEMPS
HUT_S023	coarse blocks	9.6	321.8	2657.6	TEMPS
HUT_S027	coarse blocks	19.0	331.2	2785.3	TEMPS

Name of measurement device	Type of surface material	Slope [°]	Aspect [°]	Elevation [m asl.]	Project
HUT_S045	coarse blocks	23.1	266.9	2579.7	TEMPS
LAP_R001	bedrock	15.0	310.4	2364.9	PERMOS
LAP_R002	bedrock	43.7	93.6	2719.3	PERMOS
LAP_R003	bedrock	52.6	131.0	2690.5	PERMOS
LAP_R004	bedrock	45.1	240.3	2706.1	PERMOS
LAP_R005	bedrock	14.2	277.9	2801.5	PERMOS
LAP_R006	bedrock	3.7	344.7	2736.7	PERMOS
LAP_S013	coarse blocks	26.2	22.3	2517.4	PERMOS
LAP_S015	coarse blocks	27.2	6.6	2512.7	PERMOS
LAP_S019	debris	28.9	4.5	2512.1	PERMOS
LAP_S023	debris	32.5	8.3	2448.5	PERMOS
LAP_S026	debris	25.4	28.6	2448.4	PERMOS
LAP_S028	coarse blocks	22.9	12.7	2451.4	PERMOS
LAP_S029	coarse blocks	22.7	35.4	2449.2	PERMOS
LAP_S031	coarse blocks	17.0	47.3	2392.8	PERMOS
LAP_S032	coarse blocks	18.6	31.5	2390.8	PERMOS
LAP_S035	coarse blocks	21.6	21.3	2412.3	PERMOS
LAP_S036	coarse blocks	17.4	45.9	2376.1	PERMOS
LAP_S037	debris	21.4	39.1	2495.0	PERMOS
LAP_S038	coarse blocks	21.2	33.1	2480.5	PERMOS
LAP_S040	soil	32.1	24.4	2567.9	PERMOS
LAP_S041	coarse blocks	23.1	21.1	2486.4	PERMOS
LAP_S042	debris	21.6	30.6	2506.3	PERMOS
LAP_S043	coarse blocks	23.3	30.6	2511.1	PERMOS
LAP_S044	debris	23.8	23.9	2524.8	PERMOS
LAP_S045	coarse blocks	26.6	21.2	2550.2	PERMOS
LDV_S007	debris	26.1	306.0	2736.8	TEMPS
LDV_S008	coarse blocks	37.4	311.9	2736.2	TEMPS
LDV_S009	coarse blocks	11.2	305.8	2714.8	TEMPS
LDV_S010	debris	29.2	308.5	2766.3	TEMPS
LDV_S013	debris	36.2	315.8	2806.6	TEMPS
LDV_S014	debris	29.0	316.7	2770.2	TEMPS
LDV_S015	debris	28.4	300.7	2733.7	TEMPS
LDV_S017	debris	36.3	300.1	2784.1	TEMPS
LDV_S019	coarse blocks	23.5	305.6	2727.9	TEMPS
MDO_S001	soil	13.3	187.1	2764.6	TEMPS
MDO_S002	debris	9.2	228.9	2753.8	TEMPS
MDO_S003	debris	13.3	282.6	2761.1	TEMPS
MDO_S004	debris	26.8	286.8	2768.7	TEMPS
MDO_S005	debris	32.0	281.8	2773.9	TEMPS
MDO_S006	debris	32.8	291.3	2788.5	TEMPS
MDO_S010	debris	35.8	291.8	2813.0	TEMPS

Name of measurement device	Type of surface material	Slope [°]	Aspect [°]	Elevation [m asl.]	Project
MDO_S018	debris	40.5	286.7	2826.4	TEMPS
MIL_S001	soil	52.1	32.4	2451.8	PERMOS
MIL_S002	coarse blocks	32.7	47.8	2427.8	PERMOS
MIL_S003	coarse blocks	17.4	57.2	2414.9	PERMOS
MIL_S004	coarse blocks	13.1	46.7	2408.4	PERMOS
MIL_S005	coarse blocks	9.5	33.2	2400.6	PERMOS
MIL_S008	coarse blocks	24.0	43.5	2377.3	PERMOS
MIL_S009	coarse blocks	33.4	55.7	2347.3	PERMOS
MIL_S010	coarse blocks	20.5	49.0	2338.8	PERMOS
MIL_S021	soil	27.3	17.4	2366.7	PERMOS
MIL_S024	coarse blocks	21.5	52.7	2441.1	PERMOS
MIL_S031	debris	14.9	357.4	2302.6	PERMOS
MIL_S032	soil	35.9	352.4	2295.9	PERMOS
MIL_S034	coarse blocks	11.6	341.5	2257.7	PERMOS
MIL_S035	coarse blocks	22.5	33.1	2226.9	PERMOS
MIL_S036	soil	28.8	340.1	2306.5	PERMOS
MIL_S041	debris	39.5	46.0	2432.5	PERMOS
MIL_S043	debris	42.5	41.7	2437.9	PERMOS
MIL_S044	debris	33.5	47.3	2428.3	PERMOS
PMR_S001	debris	34.2	107.4	2604.7	TEMPS
PMR_S002	coarse blocks	24.9	87.7	2621.6	TEMPS
REC_R001	bedrock	51.5	126.0	3129.8	PERMOS
REC_R002	bedrock	52.6	186.5	3135.9	PERMOS
REC_R003	bedrock	34.6	165.8	3134.6	PERMOS
REC_R004	bedrock	30.2	246.3	2605.5	PERMOS
REC_R005	bedrock	20.1	316.0	2611.7	PERMOS
REC_R006	bedrock	9.6	10.4	2615.4	PERMOS
REC_S002	coarse blocks	22.9	301.8	2648.5	PERMOS
REC_S003	coarse blocks	24.1	344.4	2707.5	PERMOS
REC_S004	coarse blocks	13.0	282.1	2801.2	PERMOS
REC_S005	coarse blocks	6.6	52.2	2812.1	PERMOS
REC_S006	coarse blocks	4.9	353.3	2791.7	PERMOS
REC_S007	coarse blocks	13.5	17.3	2804.5	PERMOS
REC_S008	coarse blocks	20.0	350.4	2817.7	PERMOS
REC_S009	coarse blocks	26.6	344.5	2845.7	PERMOS
REC_S011	coarse blocks	21.1	322.9	2661.2	PERMOS
REC_S012	coarse blocks	12.3	336.6	2646.5	PERMOS
REC_S042	coarse blocks	6.6	244.2	2806.6	PERMOS
REC_S043	coarse blocks	14.1	95.6	2804.2	PERMOS
REC_S143	coarse blocks	10.9	252.5	2651.0	PERMOS
RTD_S001	debris	43.1	4.2	2497.1	TEMPS
RTD_S002	debris	27.6	342.8	2739.5	TEMPS

Name of measurement device	Type of surface material	Slope [°]	Aspect [°]	Elevation [m asl.]	Project
RTD_S003	coarse blocks	11.8	203.7	2774.9	TEMPS
RTD_S004	coarse blocks	2.7	286.4	2816.1	TEMPS
RTD_S005	debris	5.1	31.6	2849.5	TEMPS
RTD_S006	coarse blocks	15.8	263.2	2862.8	TEMPS
RTD_S007	coarse blocks	6.3	318.5	2835.3	TEMPS
RTD_S008	debris	34.0	254.6	2828.8	TEMPS
RTD_S009	coarse blocks	18.0	279.3	2861.6	TEMPS
RTD_S010	debris	14.2	350.7	2956.0	TEMPS
RTD_S011	debris	15.3	285.5	2909.2	TEMPS
RTD_S012	debris	17.5	227.8	2888.3	TEMPS
RTD_S013	coarse blocks	9.7	295.0	2888.6	TEMPS
RTD_S014	debris	20.2	264.9	2884.1	TEMPS
RTD_S015	coarse blocks	29.9	293.6	2816.1	TEMPS
RTD_S016	debris	26.3	254.1	2810.8	TEMPS
RTD_S017	coarse blocks	29.2	258.2	2815.3	TEMPS
RTD_S018	coarse blocks	17.5	225.6	2853.0	TEMPS
RTD_S019	coarse blocks	10.9	159.1	2872.6	TEMPS
RTD_S020	coarse blocks	35.4	325.8	2859.7	TEMPS
RTD_S021	coarse blocks	4.6	128.1	2868.7	TEMPS
RTD_S022	coarse blocks	10.7	256.8	2870.9	TEMPS
SBE_S001	coarse blocks	25.1	247.0	2721.8	PERMOS
SBE_S002	coarse blocks	21.0	253.6	2723.5	PERMOS
SBE_S003	coarse blocks	30.4	213.4	2715.9	PERMOS
SBE_S004	coarse blocks	13.6	278.1	2733.7	PERMOS
SBE_S006	coarse blocks	21.2	219.5	2727.8	PERMOS
SBE_S008	coarse blocks	12.2	274.4	2740.5	PERMOS
SBE_S009	coarse blocks	10.6	246.0	2736.3	PERMOS
SCH_R006	bedrock	6.0	102.8	2451.7	PERMOS
SCH_R007	bedrock	7.0	74.3	2406.8	PERMOS
SCH_R008	bedrock	8.6	36.5	2608.8	PERMOS
SCH_R010	bedrock	23.8	147.0	2671.4	PERMOS
SCH_R011	bedrock	17.8	99.7	2792.5	PERMOS
SCH_R012	bedrock	46.8	174.9	2943.9	PERMOS
SCH_S000	debris	9.3	269.0	2957.2	PERMOS
SCH_S001	debris	9.3	269.0	2957.2	PERMOS
SCH_S002	debris	30.6	226.6	2947.7	PERMOS
SCH_S003	debris	37.0	226.3	2939.1	PERMOS
SCH_S004	debris	41.2	229.0	2934.3	PERMOS
SCH_S005	debris	34.6	224.8	2912.7	PERMOS
SCH_S006	debris	38.5	219.2	2865.0	PERMOS
SCH_S007	debris	38.7	24.6	2930.9	PERMOS
SCH_S008	debris	34.0	24.1	2890.8	PERMOS

Name of measurement device	Type of surface material	Slope [°]	Aspect [°]	Elevation [m asl.]	Project
SCH_S009	debris	36.8	22.8	2944.7	PERMOS
SCH_S010	debris	29.0	19.7	2924.2	PERMOS
SCH_S011	debris	24.7	17.5	2911.8	PERMOS
SCH_S012	debris	39.4	23.1	2897.2	PERMOS
SCH_S014	debris	33.6	42.8	2871.6	PERMOS
SCH_S015	debris	33.2	31.9	2854.4	PERMOS
SCH_S016	debris	38.4	25.9	2844.3	PERMOS
SCH_S017	debris	34.8	22.5	2831.9	PERMOS
SCH_S018	debris	22.8	32.8	2807.8	PERMOS
SCH_S019	debris	16.1	68.5	2785.4	PERMOS
SCH_S021	debris	27.5	13.6	2908.8	PERMOS
SCH_S022	debris	17.2	58.6	2796.9	PERMOS
TMI_S017	coarse blocks	22.7	288.9	2601.9	PERMOS
TMI_S019	coarse blocks	16.1	271.1	2548.5	PERMOS
TMI_S020	coarse blocks	24.2	282.9	2498.0	PERMOS
TMI_S021	coarse blocks	20.2	268.8	2542.3	PERMOS
TMI_S022	coarse blocks	23.9	288.2	2567.4	PERMOS
TSA_R001	bedrock	47.6	260.6	3038.2	PERMOS
TSA_R003	bedrock	48.7	255.4	3037.5	PERMOS
TSA_R005	bedrock	22.9	241.1	3071.6	PERMOS
TSA_S002	debris	31.9	217.4	3046.6	PERMOS
TSA_S004	debris	32.8	227.1	3054.8	PERMOS
TSA_S006	debris	31.9	101.1	3064.6	PERMOS
YET_R026	bedrock	56.1	0.8	2827.7	PERMOS
YET_R027	bedrock	39.4	23.8	2813.9	PERMOS
YET_S001	debris	28.2	47.1	2622.5	PERMOS
YET_S002	coarse blocks	20.8	26.0	2658.9	PERMOS
YET_S003	coarse blocks	21.0	5.7	2699.3	PERMOS
YET_S004	coarse blocks	11.4	339.5	2744.4	PERMOS
YET_S010	coarse blocks	20.5	50.7	2595.6	PERMOS
YET_S013	coarse blocks	37.5	40.4	2687.9	PERMOS
YET_S014	coarse blocks	20.6	42.5	2715.3	PERMOS
YET_S015	coarse blocks	22.4	74.8	2763.0	PERMOS
YET_S016	coarse blocks	10.4	54.9	2681.9	PERMOS
YET_S028	debris	30.7	45.7	2646.8	PERMOS

Table 7.9: Meta data of measurement devices used for multiple linear regression model from projects *ARPA VDA* and *PERMASENSE*.

Name of measurement device	Type of surface material	Slope [°]	Aspect [°]	Elevation [m asl.]	Project
ADME_TR	bedrock	60.0	118.0	3823.0	ARPA VDA
ADMN_TR	bedrock	80.0	334.0	3820.0	ARPA VDA
ADMS_TR	bedrock	85.0	160.0	3820.0	ARPA VDA
ADMW_TR	bedrock	85.0	270.0	3825.0	ARPA VDA
CCS_TR	bedrock	90.0	158.0	3820.0	ARPA VDA
CCW_TR	bedrock	85.0	320.0	3815.0	ARPA VDA
CHEM_TR	bedrock	90.0	180.0	3750.0	ARPA VDA
CM_41_BH	debris	0.0	270.0	3100.0	ARPA VDA
CM_7_BH	debris	5.0	270.0	3100.0	ARPA VDA
GJNup_TR	bedrock	75.0	340.0	4100.0	ARPA VDA
GJSR_TR	bedrock	90.0	160.0	4100.0	ARPA VDA
MR_TR	bedrock	90.0	180.0	3180.0	ARPA VDA
ONFR_TR	bedrock	90.0	180.0	2992.0	ARPA VDA
VCN_TR	bedrock	45.0	352.0	4450.0	ARPA VDA
VCS_TR	bedrock	60.0	168.0	4450.0	ARPA VDA
mh01	bedrock	75.0	95.0	3470.0	PERMASENSE
mh02	bedrock	50.0	80.0	3474.0	PERMASENSE
mh03	bedrock	65.0	350.0	3456.0	PERMASENSE
mh06	bedrock	60.0	90.0	3476.0	PERMASENSE
mh09	bedrock	70.0	80.0	3534.0	PERMASENSE
mh10	bedrock	90.0	140.0	3438.0	PERMASENSE
mh11	bedrock	70.0	340.0	3456.0	PERMASENSE

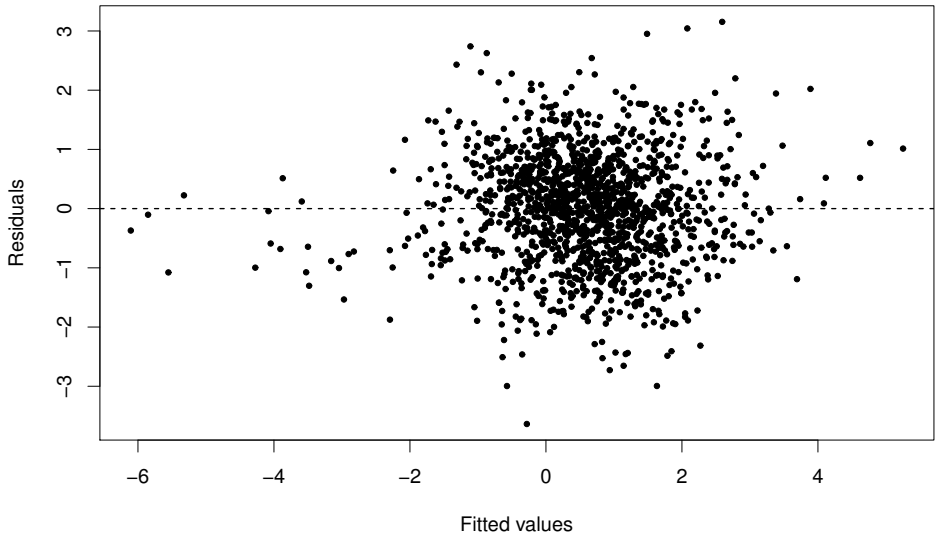

Figure 7.5: Tukey-Anscombe plot of the multiple linear regression model. If the residuals are independent, no pattern is visible in the scatter plot.

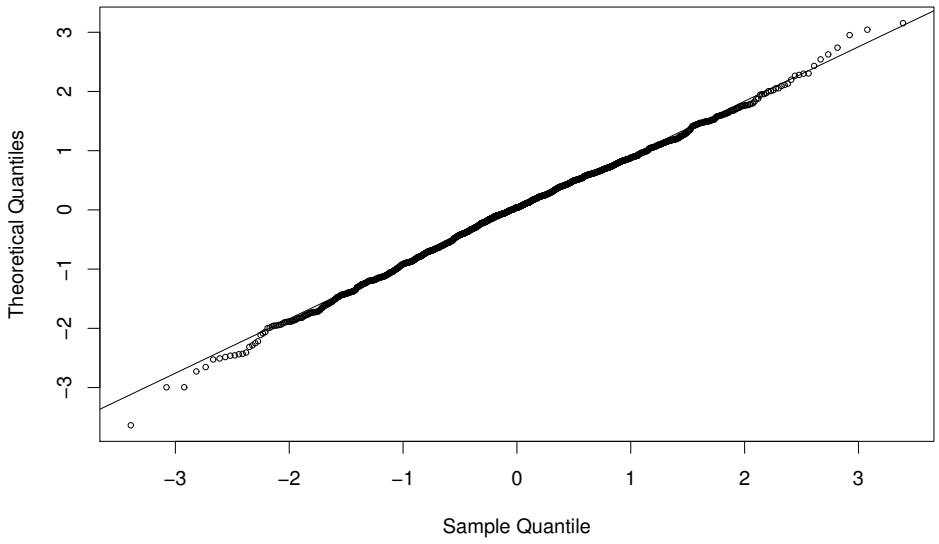

Figure 7.6: Q-Q plot of the multiple linear regression model. If the residuals come from a normal distribution, the data points are located on a straight line.

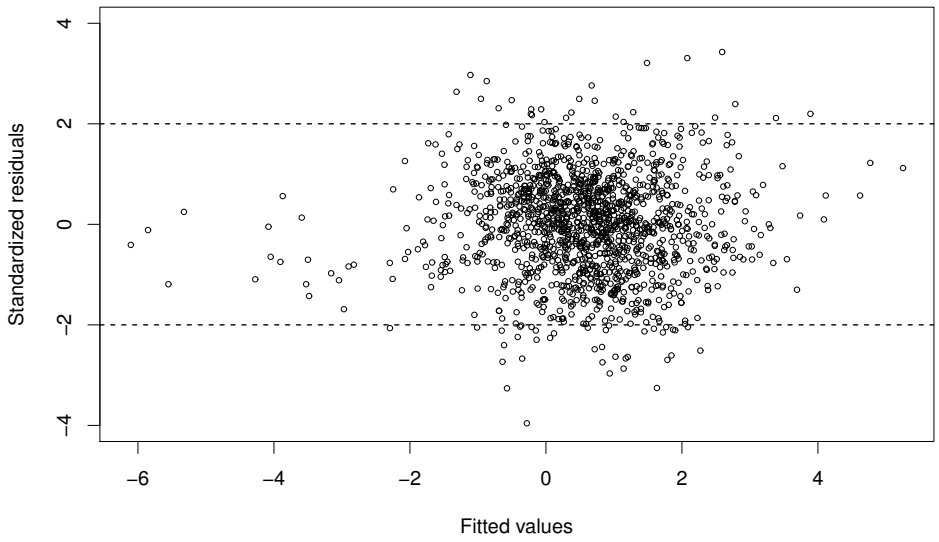

Figure 7.7: Homogeneity of variance of the multiple linear regression model. Given homogeneity of variance, no increasing or decreasing pattern is present.

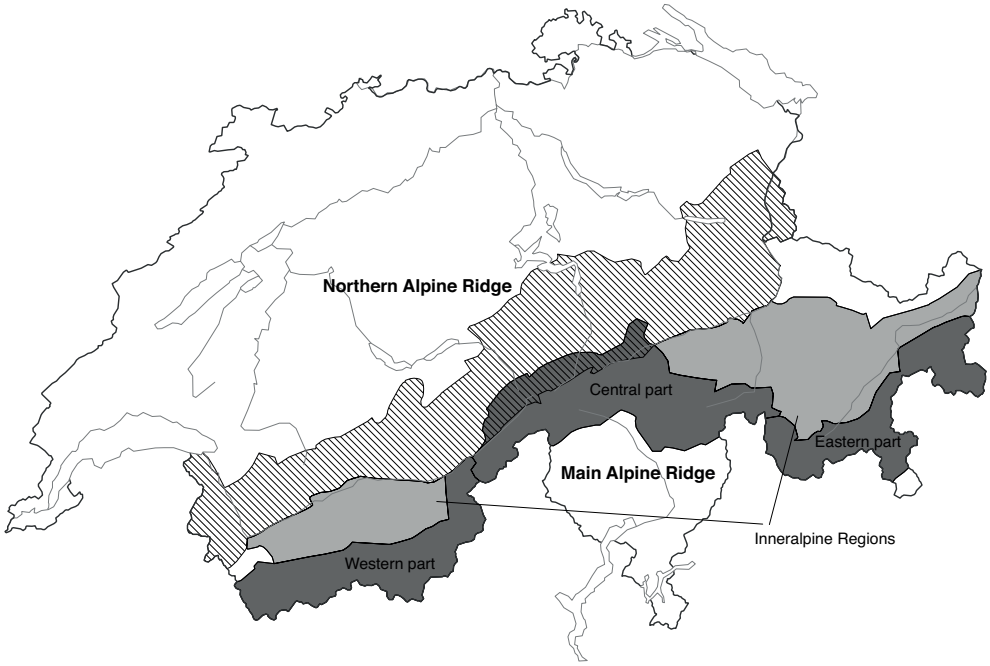

Figure 7.8: Main and Northern Alpine Ridge with inneralpine regions. Source: Main Alpine Ridge © SLF.

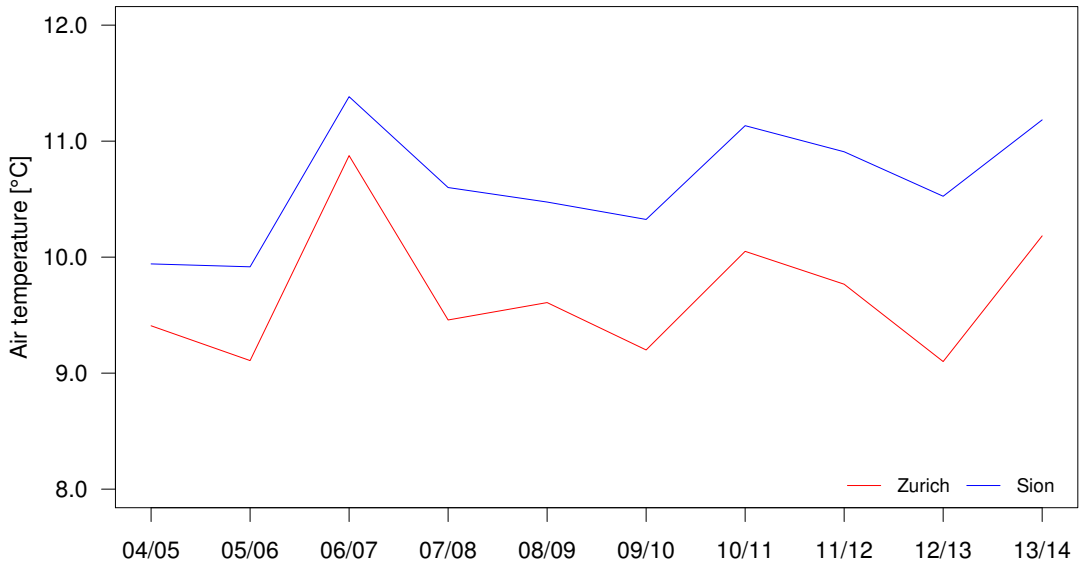

Figure 7.9: Air temperature from Zurich and Sion for hydrological years 2005 – 2014. Data is based on long-time homogeneous series of monthly temperature averages, measured at the corresponding stations of the Swiss national basic climatological network (Swiss NBCN). Data source: MeteoSwiss.

E Temporal variability

E.1 Ground surface temperatures

Table 7.10: Meta data of GST measurement devices used for correlation analysis.

Name of measurement device	Type of surface material	Slope [°]	Aspect [°]	Elevation [m asl.]	Project
AGE_S001	debris	7.8	127.8	2851.1	PERMOS
AGE_S002	debris	8.3	187.3	2828.1	PERMOS
AGE_S005	debris	17.8	276.2	2883.2	PERMOS
AGE_S006	debris	29.1	127.9	2910.0	PERMOS
AGE_S007	coarse blocks	12.1	143.2	2881.2	PERMOS
ATT_S002	soil	33.4	266.9	2712.8	PERMOS
ATT_S003	debris	26.0	269.6	2682.1	PERMOS
ATT_S004	coarse blocks	20.2	273.7	2653.2	PERMOS
ATT_S005	debris	26.2	286.3	2649.8	PERMOS
ATT_S013	debris	29.1	269.1	2698.1	PERMOS
ATT_S021	coarse blocks	27.4	286.2	2667.0	PERMOS
ATT_S022	coarse blocks	26.4	287.1	2649.9	PERMOS
COR_R002	bedrock	4.4	49.6	2532.6	PERMOS
COR_R005	bedrock	43.9	273.3	2767.5	PERMOS
COR_R006	bedrock	56.5	316.7	3277.0	PERMOS
COR_R007	bedrock	15.4	238.2	3287.9	PERMOS
COR_R008	bedrock	32.4	137.2	3290.1	PERMOS
COR_R009	bedrock	41.9	153.2	2835.0	PERMOS
COR_R010	bedrock	50.2	100.7	2832.2	PERMOS
COR_R011	bedrock	15.2	351.9	2735.8	PERMOS
COR_R012	bedrock	14.6	44.8	2767.3	PERMOS
DRE_S013	coarse blocks	36.6	78.0	1585.9	PERMOS
DRE_S014	coarse blocks	34.8	82.7	1595.0	PERMOS
DRE_S015	coarse blocks	35.6	85.1	1623.5	PERMOS
GFU_S002	coarse blocks	20.3	334.9	2461.7	PERMOS
GFU_S003	coarse blocks	21.3	347.9	2471.9	PERMOS
GFU_S004	coarse blocks	17.1	6.2	2500.4	PERMOS
GFU_S005	coarse blocks	20.3	8.6	2520.8	PERMOS
GFU_S007	coarse blocks	26.5	335.0	2534.9	PERMOS
GFU_S008	coarse blocks	28.3	357.1	2526.1	PERMOS
GFU_S011	coarse blocks	27.4	313.0	2486.8	PERMOS
GFU_S017	coarse blocks	23.3	27.8	2490.6	PERMOS
GFU_S031	coarse blocks	25.7	9.0	2508.0	PERMOS
GFU_S032	debris	34.2	4.4	2501.4	PERMOS
GFU_S036	coarse blocks	18.9	336.5	2557.7	PERMOS
JFJ_R005	bedrock	61.4	356.5	3715.5	PERMOS

Name of measurement device	Type of surface material	Slope [°]	Aspect [°]	Elevation [m asl.]	Project
LAP_S013	coarse blocks	26.2	22.3	2517.4	PERMOS
LAP_S015	coarse blocks	27.2	6.6	2512.7	PERMOS
LAP_S028	coarse blocks	22.9	12.7	2451.4	PERMOS
LAP_S031	coarse blocks	17.0	47.3	2392.8	PERMOS
LAP_S035	coarse blocks	21.6	21.3	2412.3	PERMOS
LAP_S037	debris	21.4	39.1	2495.0	PERMOS
LAP_S042	debris	21.6	30.6	2506.3	PERMOS
LAP_S043	coarse blocks	23.3	30.6	2511.1	PERMOS
MIL_S002	coarse blocks	32.7	47.8	2427.8	PERMOS
MIL_S003	coarse blocks	17.4	57.2	2414.9	PERMOS
MIL_S004	coarse blocks	13.1	46.7	2408.4	PERMOS
MIL_S005	coarse blocks	9.5	33.2	2400.6	PERMOS
MIL_S008	coarse blocks	24.0	43.5	2377.3	PERMOS
MIL_S009	coarse blocks	33.4	55.7	2347.3	PERMOS
MIL_S010	coarse blocks	20.5	49.0	2338.8	PERMOS
MIL_S021	soil	27.3	17.4	2366.7	PERMOS
MIL_S024	coarse blocks	21.5	52.7	2441.1	PERMOS
MIL_S031	debris	14.9	357.4	2302.6	PERMOS
MIL_S032	soil	35.9	352.4	2295.9	PERMOS
MIL_S034	coarse blocks	11.6	341.5	2257.7	PERMOS
MIL_S035	coarse blocks	22.5	33.1	2226.9	PERMOS
MIL_S036	soil	28.8	340.1	2306.5	PERMOS
MIL_S041	debris	39.5	46.0	2432.5	PERMOS
MIL_S043	debris	42.5	41.7	2437.9	PERMOS
MIL_S044	debris	33.5	47.3	2428.3	PERMOS
MPR_S008	coarse blocks	18.0	325.9	2533.4	PERMOS
MPR_S021	coarse blocks	15.0	20.9	2480.7	PERMOS
REC_S002	coarse blocks	22.9	301.8	2648.5	PERMOS
REC_S003	coarse blocks	24.1	344.4	2707.5	PERMOS
REC_S004	coarse blocks	13.0	282.1	2801.2	PERMOS
REC_S006	coarse blocks	4.9	353.3	2791.7	PERMOS
REC_S007	coarse blocks	13.5	17.3	2804.5	PERMOS
REC_S008	coarse blocks	20.0	350.4	2817.7	PERMOS
REC_S011	coarse blocks	21.1	322.9	2661.2	PERMOS
REC_S012	coarse blocks	12.3	336.6	2646.5	PERMOS
REC_S042	coarse blocks	6.6	244.2	2806.6	PERMOS
REC_S043	coarse blocks	14.1	95.6	2804.2	PERMOS
REC_S143	coarse blocks	10.9	252.5	2651.0	PERMOS
SCH_R007	bedrock	7.0	74.3	2406.8	PERMOS
SCH_R009	bedrock	32.5	179.0	2677.5	PERMOS
SCH_R010	bedrock	23.8	147.0	2671.4	PERMOS
SCH_R011	bedrock	17.8	99.7	2792.5	PERMOS

Name of measurement device	Type of surface material	Slope [°]	Aspect [°]	Elevation [m asl.]	Project
YET_S004	coarse blocks	11.4	339.5	2744.4	PERMOS
YET_S014	coarse blocks	20.6	42.5	2715.3	PERMOS
YET_S016	coarse blocks	10.4	54.9	2681.9	PERMOS

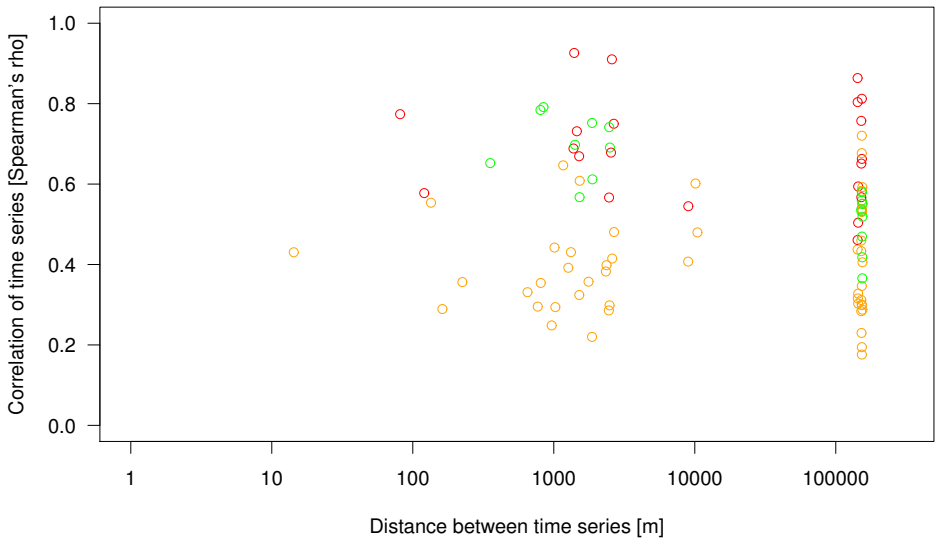

Figure 7.10: Correlation of distance and Spearman's rank correlation coefficient between all possible pairs of GST time series with bedrock as type of surface material. The colors of the circles refer to the combination of the types of surface material within each pair: red = steep bedrock / steep bedrock, green = flat bedrock / flat bedrock, orange = steep bedrock / flat bedrock. *Flat bedrock* is defined as bedrock with a slope $< 30°$, whereas *steep bedrock* is defined as bedrock with a slope $\geq 30°$.

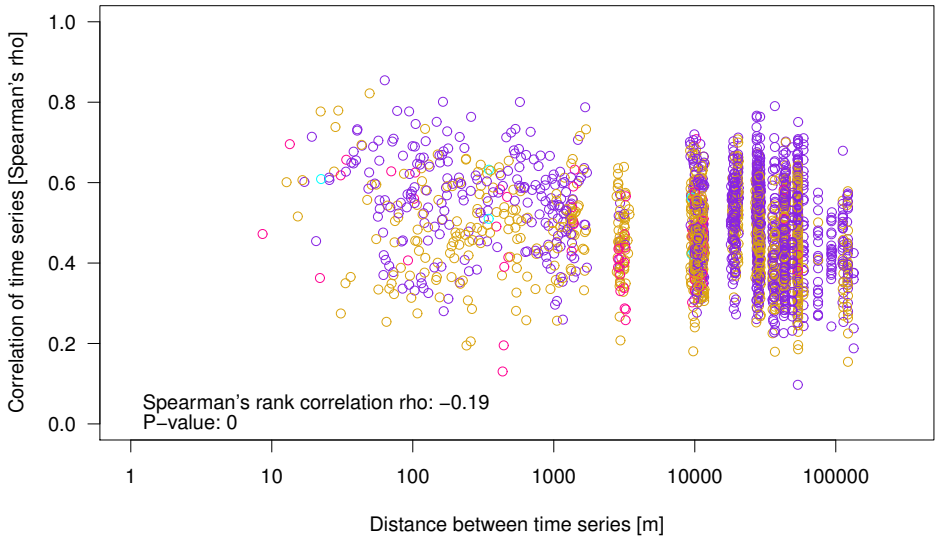

Figure 7.11: Correlation of distance and Spearman's rank correlation coefficient between all possible pairs of GST time series with soil, debris and coarse blocks as types of surface material. The colors of the circles refer to the combination of the types of surface material within each pair: violet = coarse blocks / coarse blocks, pink = debris / debris, cyan = soil / soil, gold = coarse blocks / debris, coarse blocks / soil, soil / debris.

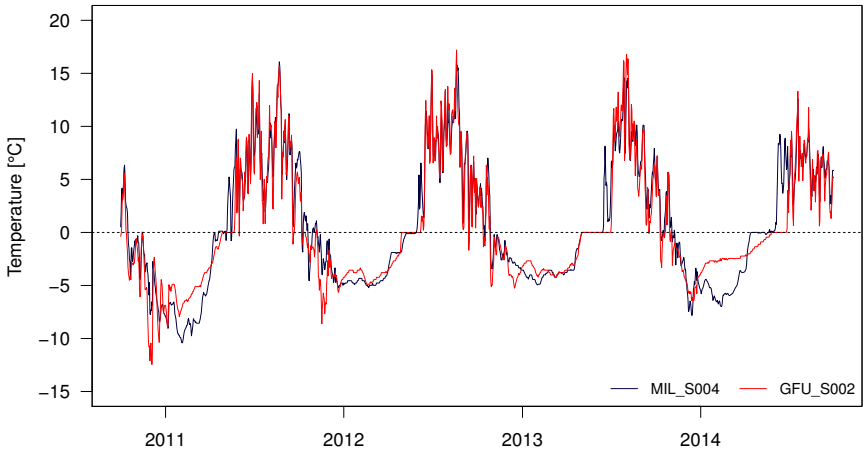

Figure 7.12: GST time series with a correlation coefficient of 0.751, located 54 km apart.

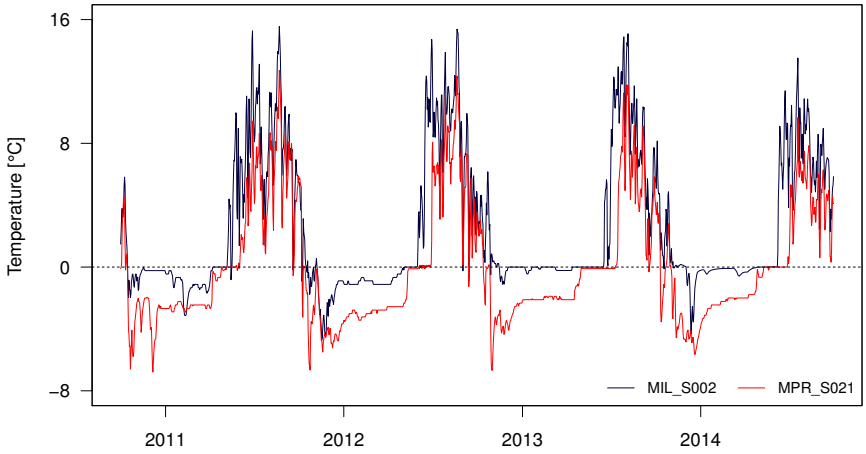

Figure 7.13: GST time series with a correlation coefficient of 0.539, located 120 km apart.

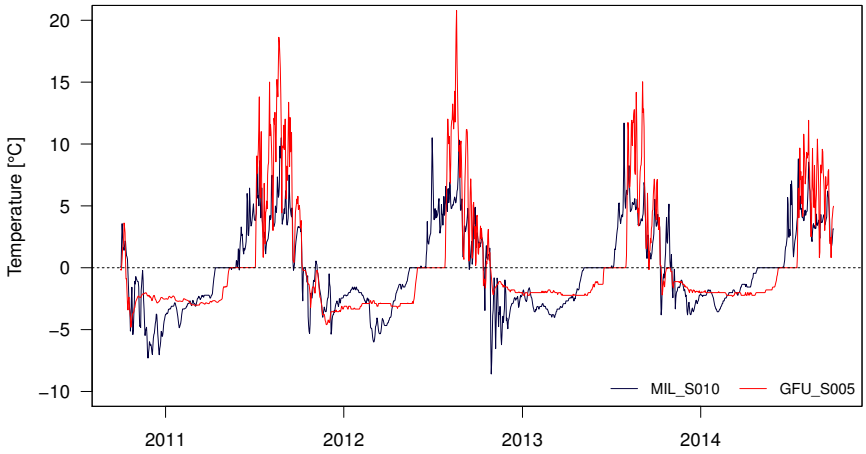

Figure 7.14: GST time series with a correlation coefficient of 0.097, located 54 km apart.

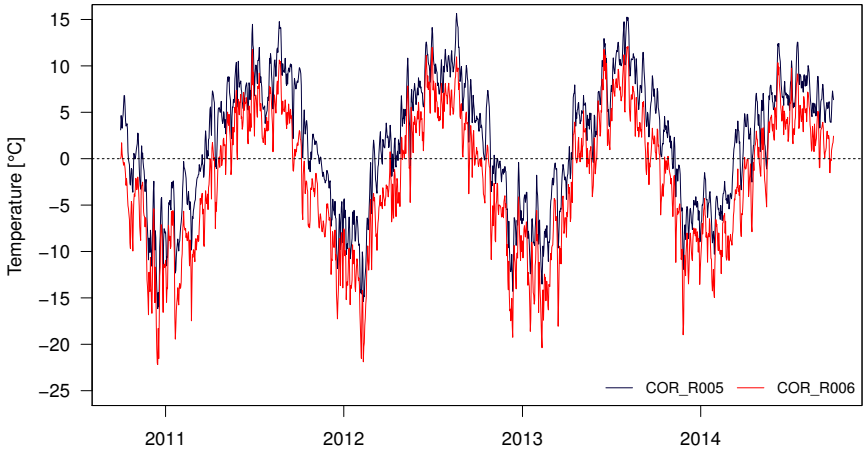

Figure 7.15: GST time series with correlation coefficient of 0.926 and steep bedrock as type of surface material. The measurement devices are located 1400 m apart.

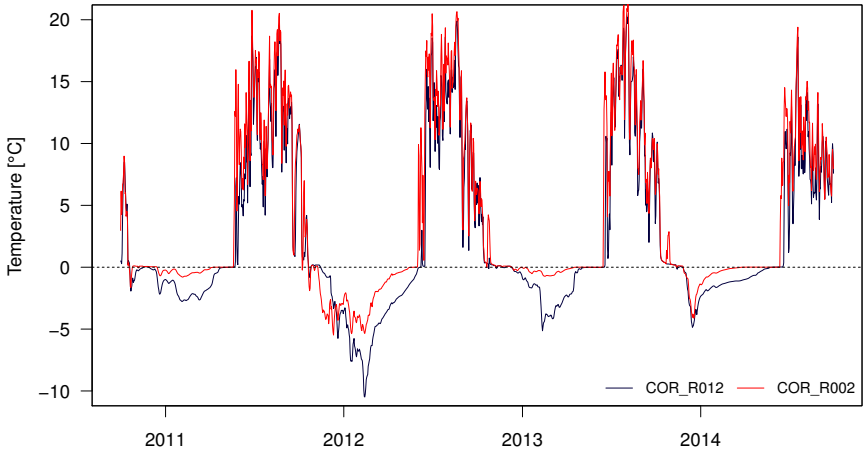

Figure 7.16: GST time series with correlation coefficient of 0.791 and flat bedrock as type of surface material. The measurement devices are located 845 m apart.

Table 7.11: Correlation coefficients, distance and mean difference of MAGST between GST time series for hydrological years 2011 – 2014.

Measurement devices	Type of surface material	Distance [km]	Correlation coefficient	Mean difference of MAGST [°C]
COR_R005/COR_R006	bedrock	1.4	0.926	4.179
MIL_S004/GFU_S002	coarse blocks	54	0.751	0.169
MIL_S010/GFU_S005	coarse blocks	54	0.097	0.372

Table 7.12: 20 most distant GST time series of surface type coarse blocks with correlation coefficients > 0.5 and corresponding meta data.

Correlation coefficient	GST device[1]	GST device[2]	Distance [m]	SurfType[1]	SurfType[2]	Slope[1] [°]	Slope[2] [°]	Aspect[1] [°]	Aspect[2] [°]
0.539	MIL_S002	MPR_S021	122099.8	coarse blocks	coarse blocks	32.7	15.0	47.8	20.9
0.573	MIL_S003	MPR_S021	122080.6	coarse blocks	coarse blocks	17.4	15.0	57.2	20.9
0.535	MIL_S024	MPR_S008	122026.0	coarse blocks	coarse blocks	21.5	18.0	52.7	325.9
0.569	MIL_S005	MPR_S021	122020.8	coarse blocks	coarse blocks	9.5	15.0	33.2	20.9
0.554	MIL_S034	MPR_S021	121663.2	coarse blocks	coarse blocks	11.6	15.0	341.5	20.9
0.567	AGE_S007	MPR_S021	120517.0	coarse blocks	coarse blocks	12.1	15.0	143.2	20.9
0.502	AGE_S007	MPR_S008	120437.9	coarse blocks	coarse blocks	12.1	18.0	143.2	325.9
0.534	MPR_S021	YET_S004	112400.6	coarse blocks	coarse blocks	15.0	11.4	20.9	339.5
0.512	MPR_S008	YET_S004	112328.1	coarse blocks	coarse blocks	18.0	11.4	325.9	339.5
0.518	MPR_S021	YET_S014	112315.0	coarse blocks	coarse blocks	15.0	20.6	20.9	42.5
0.679	MPR_S021	YET_S016	112280.0	coarse blocks	coarse blocks	15.0	10.4	20.9	54.9
0.503	LAP_S013	MPR_S021	112045.7	coarse blocks	coarse blocks	26.2	15.0	22.3	20.9
0.514	LAP_S015	MPR_S021	111975.3	coarse blocks	coarse blocks	27.2	15.0	6.6	20.9
0.547	LAP_S035	MPR_S021	111659.9	coarse blocks	coarse blocks	21.6	15.0	21.3	20.9
0.526	MPR_S021	REC_S007	93755.9	coarse blocks	coarse blocks	15.0	13.5	20.9	17.3
0.513	MPR_S021	REC_S012	93168.8	coarse blocks	coarse blocks	15.0	12.3	20.9	336.6
0.504	MPR_S021	REC_S143	93132.9	coarse blocks	coarse blocks	15.0	10.9	20.9	252.5
0.507	MPR_S008	REC_S003	92887.8	coarse blocks	coarse blocks	18.0	24.1	325.9	344.4
0.558	GFU_S003	MPR_S021	74899.9	coarse blocks	coarse blocks	21.3	15.0	347.9	20.9
0.531	GFU_S007	MPR_S008	74837.6	coarse blocks	coarse blocks	26.5	18.0	335.0	325.9

E.2 Ground temperatures

Table 7.13: Meta data of GT measurement devices studied in correlation analysis.

Name of measurement device	Type of surface material	Slope [°]	Aspect [°]	Elevation [m asl.]	Project	Depth of measure-ment device [m]
DRE_0104	coarse blocks	30	90	1580	PERMOS	1.2
LAP_1208	coarse blocks	25	45	2535	PERMOS	1.0
LAP_0198	coarse blocks	25	45	2500	PERMOS	0.7
LAP_1108	coarse blocks	25	45	2500	PERMOS	0.7
COR_0287	coarse blocks	10	315	2670.2	PERMOS	0.55
ATT_0108	debris	25	270	2661	PERMOS	0.5
ATT_0208	coarse blocks	30	270	2689	PERMOS	0.5
GEN_0102	debris	20	90	2888	PERMOS	0.5
SCH_5000	debris	30	45	2910	PERMOS	0.8
SCH_5200	debris	30	45	2910	PERMOS	0.6
SCH_5198	debris	30	45	2910	PERMOS	0.8
MBP_0296	debris	38	315	2942	PERMOS	0.5
SBE_0190	coarse blocks	0	NA	2754.2	PERMOS	0.5
SBE_0290	coarse blocks	0	NA	2732	PERMOS	1.2
MUR_0499	coarse blocks	15	225	2549.2	PERMOS	0.79
MUR_0299	coarse blocks	15	315	2538.5	PERMOS	0.52
MUR_0199	coarse blocks	15	315	2536.1	PERMOS	0.9
COR_0200	coarse blocks	10	315	2672.3	PERMOS	0.5

Table 7.14: Lags with maximum cross-correlation coefficients of GST time series and corresponding BH time series at certain depths.

Depth	Cross-correlation coefficient	Lag [day]
0.5m	0.54	0.00
0.7m	0.53	0.00
1.0m	0.40	1.00
1.2m	0.53	1.00

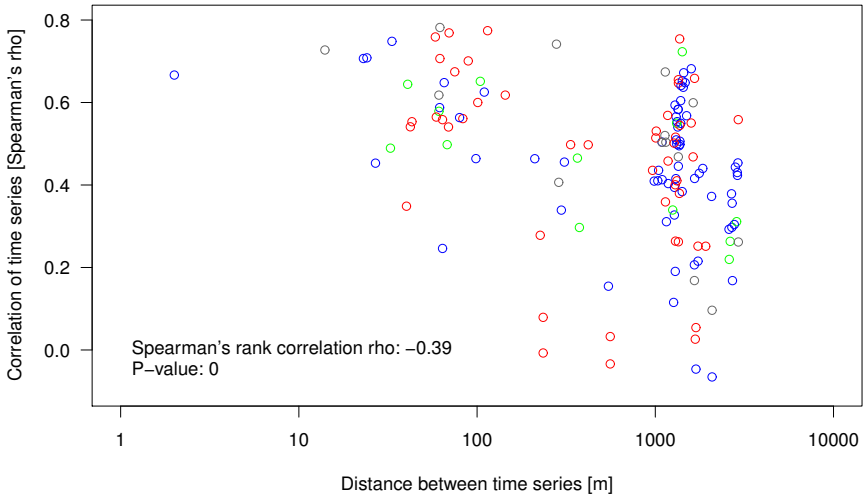

Figure 7.17: Correlation of distance and Spearman's rank correlation coefficient between GT and GST time series with distances between pairs of less than 5 km. The colors of the circles refer to the combination of the types of surface material within each pair. The first type of surface material refers to the GT time series, the second one to the GST time series: red = debris or coarse blocks for both time series, gray = debris or coarse blocks / steep bedrock, green = debris or coarse blocks / flat bedrock, blue = debris or coarse blocks / soil or debris or coarse blocks.

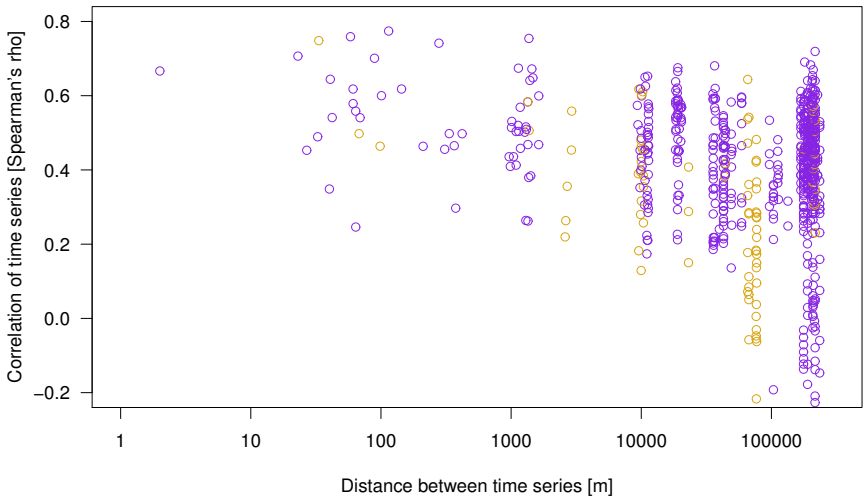

Figure 7.18: Correlation of distance and Spearman's rank correlation coefficient between GT and GST time series with debris and coarse blocks as type of surface material. The colors of the circles refer to the combination of the types of surface material within each pair: violet = coarse blocks / coarse blocks, gold = debris / debris.

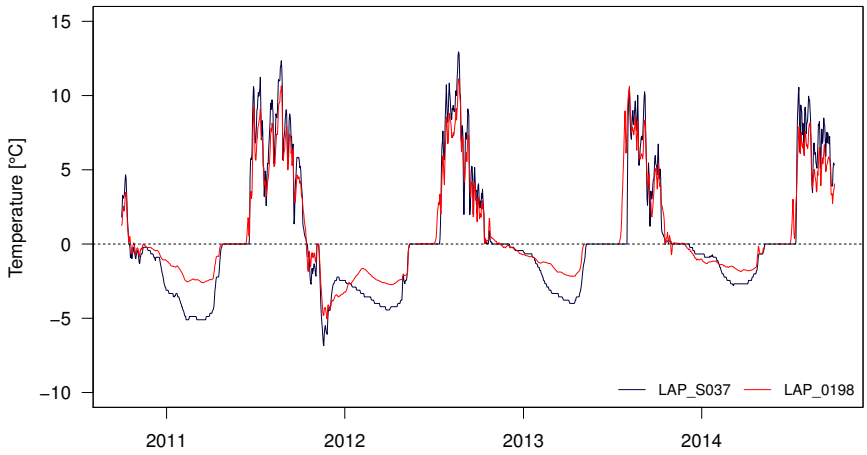

Figure 7.19: GT (red) and GST (blue) time series with coarse blocks and debris as type of surface material and a correlation coefficient of 0.782. GT measurement device has a slope of 25° and aspect of 45°, GST logger has a slope of 21.4° and a aspect of 39.1°. The measurement devices are located 60 m apart.

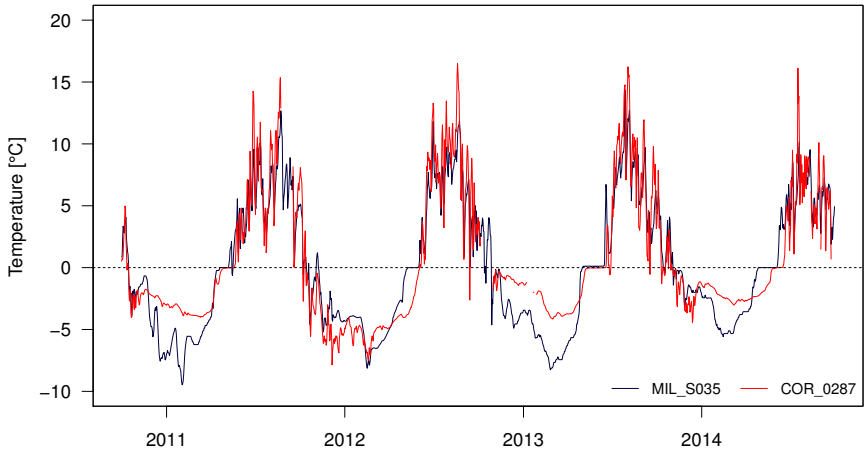

Figure 7.20: GT (red) and GST (blue) time series with coarse blocks as type of surface material for both time series and a correlation coefficient of 0.654. GT measurement device has a slope of 10° and aspect of 315°, GST logger has a slope of 22.5° and a aspect of 33.1°. The measurement devices are located 206 km apart.

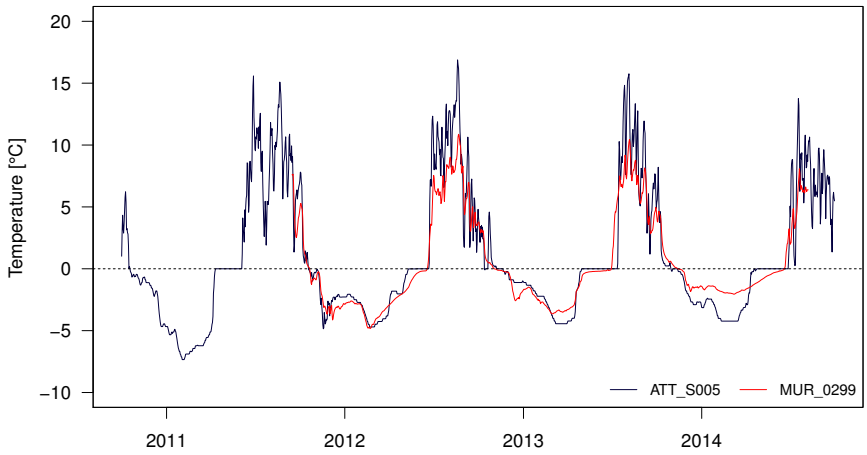

Figure 7.21: GT (red) and GST (blue) time series with coarse blocks and debris as type of surface material and a correlation coefficient of 0.684. GT measurement device has a slope of 15° and aspect of 315°, GST logger has a slope of 26.2° and a aspect of 286.3°. The measurement devices are located 209 km apart.

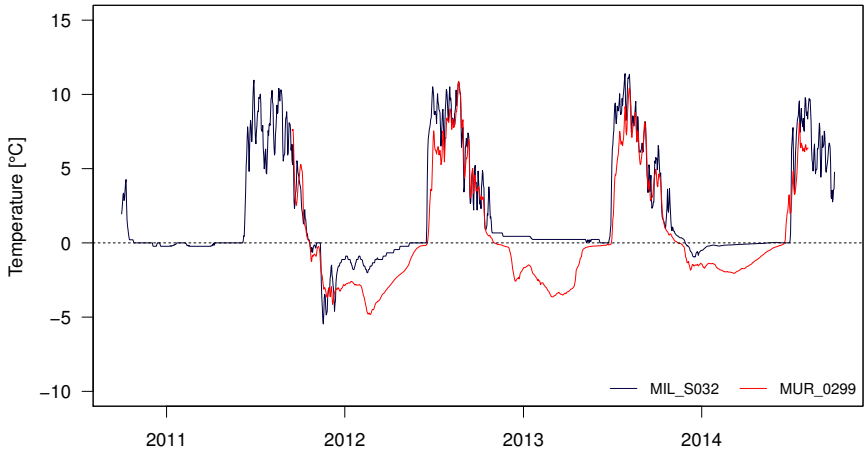

Figure 7.22: GT (red) and GST (blue) time series with coarse blocks and soil as type of surface material and a correlation coefficient of 0.622. GT measurement device has a slope of 15° and aspect of 315°, GST logger has a slope of 35.9° and a aspect of 352.4°. The measurement devices are located 216 km apart.

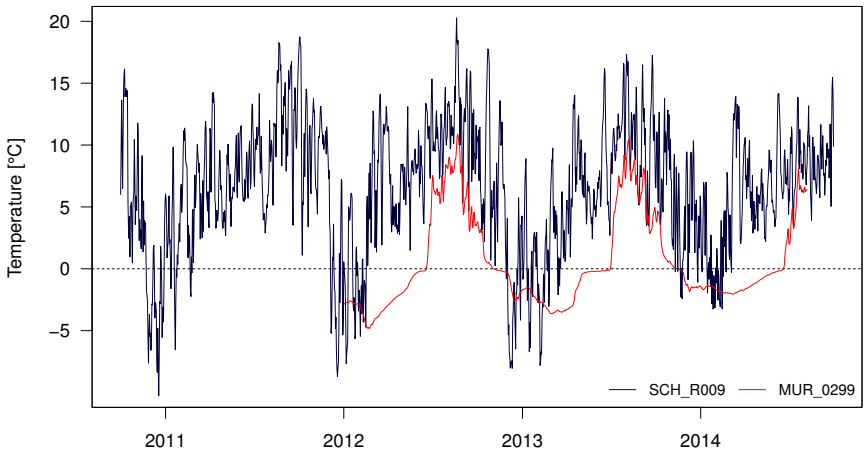

Figure 7.23: GT (red) and GST (blue) time series with coarse blocks and steep bedrock as type of surface material and a correlation coefficient of -0.006. GT measurement device has a slope of 15° and aspect of 315°, GST logger has a slope of 32.5° and a aspect of 179°. The measurement devices are located 159 km apart.

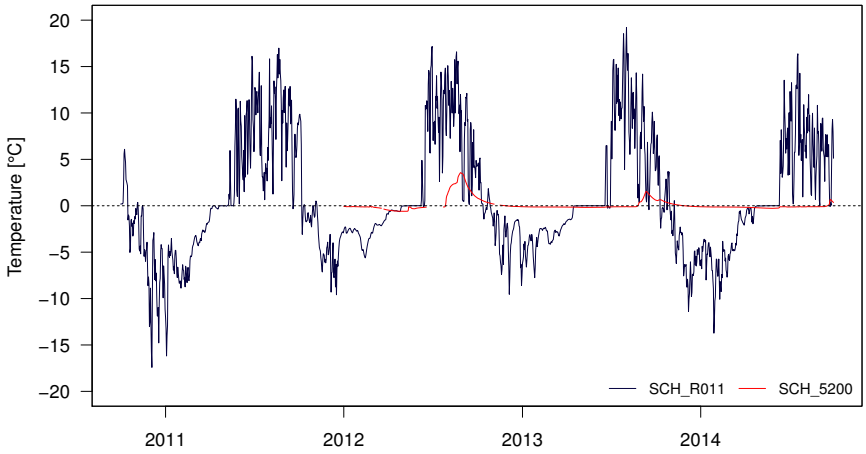

Figure 7.24: GT (red) and GST (blue) time series with debris flat bedrock as type of surface material and a correlation coefficient of -0.007. GT measurement device has a slope of 30° and aspect of 45°, GST logger has a slope of 17.8° and a aspect of 99.7°. The measurement devices are located 235 m apart.

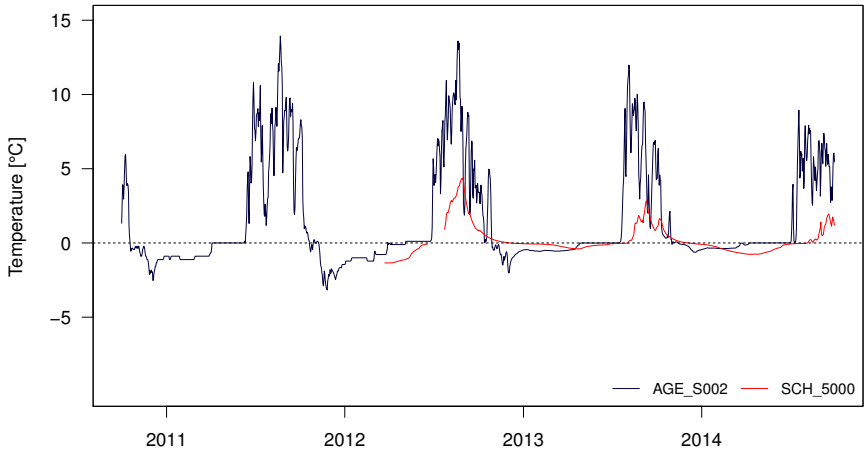

Figure 7.25: GT (red) and GST (blue) time series with debris as type of surface material for both time series and a correlation coefficient of 0.005. GT measurement device has a slope of 30° and aspect of 45°, GST logger has a slope of 8.3° and a aspect of 187.3°. The measurement devices are located 76 km apart.

Acknowledgments

At first I would like to thank Jeannette Nötzli, Stefanie Gubler and Benno Staub for their excellent supervision, valuable comments, enormous cooperativeness and great patience in answering my many questions throughout my Master's thesis. Furthermore, I would like to thank the organizations PermaSense and ARPA VDA for the generous supply of their valuable ground surface temperature data as well as MeteoSwiss for providing air temperature data. I would also like to thank the following people who supported me in writing this thesis: Ross Purves for answering my questions regarding geostatistics; Francesco Isotti, MeteoSwiss, who computed air temperature data for all of the ground surface temperature measurement locations; Samuel Weber, PermaSense, for technical support in data handling; Michael Fehlmann for his great patience in answering my many questions regarding the software R; and Miriam Müller for correcting the English text. Last but not least I would like to thank my family and Julia for the enormous support during the last nine months.

Personal declaration

I hereby declare that the submitted thesis is the result of my own, independent work. All external sources are explicitly acknowledged in the thesis.

Date: _____ Signature: _____